UNIVERSITY OF CALIFORNIA, SAN DIEGO

Seafloor geodetic measurements and modeling of Nazca - South America plate convergence

A dissertation submitted in partial satisfaction of the
requirements for the degree Doctor of Philosophy
in
Earth Sciences

by

Katie L. Gagnon

Committee in charge:

C. David Chadwell, Chair
Kevin Brown
John Hildebrand
Tara Hutchinson
Peter Lonsdale

2007

The dissertation of Katie L. Gagnon is approved, and it is acceptable in quality and form for publication on microfilm:

_____

_____

_____

_____

_____

Chair

University of California, San Diego

2007

To Those Who Have Come Before me.

TABLE OF CONTENTS

LIST OF SYMBOLS

A	Matrix of partial derivatives
α	Seismic coupling coefficient
α	Angle
β	Angle
C	Constraints
C_{STP}	Sound speed
$\mathbf{CD}_{t_1}$	Vector from new to temporary transponder
c	Critical value
c	Matrix of constraint equations
D_{acu}	Acoustic distance
$D_{opt-dcr}$	Optical distance to the transducer
$D_{opt-rng}$	Optical distance to the ring
D_{rng}	Distance
$\mathbf{DE}_{t_1}$	Vector from new to replacement transponder
$d.f.$	Degrees of freedom
dt	Time
E^T	Matrix to form null space of A
η_x	Seafloor survey package X-plane tilt
η_y	Seafloor survey package Y-plane tilt
ϵ	Angle
ϵ	Youngs modulus
FL	Camera focal length
$f(x)$	Model parameters
G	Constraints
G	Rotation matrix
G_{enu}	Rotation matrix from east, north, up
G_{VeVn}	Rotation matrix for velocity vectors

G_{VpVp}	Rotation matrix for trench parallel, perpendicular
γ	Angle
H	Height above mean sea level
$H_{dcr-pxl}$	Pixel count of transponder transducer
$H_{dcr-rng}$	Height of transducer
h	Height above ellipsoid
k	Stiffness
L	
λ	Longitude
μ_{dcr}	Camera pitch to PXP transducer
μ	Coefficient of friction
N	Orthometric height
N_{pxp}	Number of array transponders
ν_i	
∇_i	Marginally detectable blunder
∇x_i	Coordinate shift
ν	Poissons ratio
O	Matrix of observation equations
ω	Angle
P	Pressure
$\mathbf{P}$	Plate motion
p_i	Weight of i^{th} residual
$(\phi, \lambda, H)_A$	Latitude, longitude, height transponder A
ϕ_{circle}	Diameter of circle drive
ψ	Angle
$Q_{\Delta x}$	Cofactor matrix
q_i	Cofactor matrix
r_i	Redundancy number
ρ_{xy}	Correlation coefficient between x, y

ρ_{xz}	Correlation coefficient between x, z
ρ_{yz}	Correlation coefficient between y, z
S	Salinity
ss	Sound speed
Σ_c	Covariance matrix of the constraints
Σ_{enuo}	Uncertainty in east, north, up, epoch 0
Σ_{enui}	Uncertainty in east, north, up, epoch, i
$\Sigma_{e,n}$	East, north uncertainty
$\Sigma_{r,\theta}$	Uncertainty in radial direction
Σ_{VeVn}	Uncertainty in east and north velocity
Σ^*_{VeVn}	Uncertainty in east, north velocity, corrected for motion of S. America
σ^2_{VeVn}	Covariance in east and north velocity
Σ_{Vsa}	Uncertainty in velocity of South America
Σ_x	Covariance matrix of the adjusted parameters
Σ_{xyzo}	Uncertainty in x, y, z,epoch 0
Σ_{xyzi}	Uncertainty in x, y, z, epoch i
σ_{DE}	Uncertainty
σ_e	Uncertainty in east direction
σ_{en}	Uncertainty in east, north direction
σ_{GPS}	GPS positional uncertainty
σ_n	Uncertainty in north direction
σ_P	Uncertainty of plate motion
σ_x	Uncertainty in x direction
σ_y	Uncertainty in y direction
σ_z	Uncertainty in z direction
$\hat{\sigma}_{vi}$	
$\hat{\sigma}^2_0$	A priori variance of unit weight
T	Temperature
tt	Acoustic travel time

τ_i	Pope's Studentized residual
θ	Angle
θ	Latitude
θ	Angle
$u_{\alpha,\beta}$	Critical number
v_c	Residuals of the constraints
v_o	Residuals of the observations
$\hat{x}$	New estimate of unknown paramters
x_o	Initial estimate of unknowns
Δx	Corrections to unknowns
W_{rng}	Width of transponder frame ring
$W_{rng-pxl}$	Pixel count of transponder ring
Z_{off}	Height offset
Z_{ssp}	Seafloor survey package depth
Z_{pxp}^{acu}	Transponder depth from acoustic measurement
$Z_{pxp}^{opt-dcr}$	Transponder depth from optical transducer measurement
$Z_{pxp}^{opt-rng}$	Transponder depth from optical ring measurement
z_{pd}	Seafloor survey package height from transducer to pressure gauge
z_{dc}	Seafloor survey package height from transducer to camera

LIST OF FIGURES

LIST OF TABLES

ACKNOWLEDGMENTS

Several individuals supported the completion of this work. More importantly, several individuals created the foundation for this work, without which I never could have contributed to the growth of this important field. I would like to thank my advisor, Dave Chadwell, for his infinite patience and support both at-sea and on land. I have learned a great deal from him and the experiences we have shared together. I also acknowledge the late Fred Spiess for his significant contributions to this field. Dr. Spiess and Dr. Chadwell convinced me to maintain high expectations for the sciences, even when the funding, the data collection and processing and the technique itself pose daunting hurdles.

Each of my committee members have provided guidance and support whenever needed and I could not have asked for anything more. I also thank the members of the Marine Physical Lab Deeptow group: Richard Zimmerman, Dennis Rimington, Dave Price and Mariah Lovejoy. My time at sea and in the lab would not have been as productive or enjoyable without their dedication and high spirits.

The MPL administrative staff and SIO graduate office, particularly Beve Kennedy and Dawn Huffman, have truly helped guide me through the graduate school process. The always welcoming captain and crew of the Scripps' ships have also been a major contributor to this work and to my positive experiences at sea.

I also thank others who have passed through the seafloor geodesy doors, including Katie Phillips, Neil Kussat and Aaron Sweeney. In the unique order of events, in which I entered and left this field last, each has played the role of a collaborator, lab mate, ship mate, advisor and even wise, older sibling.

Finally, I would like to acknowledge the people and environment surrounding Scripps Institution of Oceanography. It is a Mecca of outstanding research, colorful sunsets and friendly, happy faces.

VITA

2001	B.S., Civil and Environmental Engineering, Worcester Polytechnic Institute
2001–2002	Research Assistant Scripps Institution of Oceanography, University of California, San Diego
2007	Ph.D., Earth Sciences Scripps Institution of Oceanography, University of California, San Diego.

PUBLICATIONS

K. Gagnon and C. D. Chadwell 2007: Relocating a seafloor transponder - Sustaining the GPS-Acoustic technique. *Earth, Planets, Space*, **59**, 327–336.

K. Gagnon and C. D. Chadwell, and F. Spiess, 2005: Evolving method to measure seafloor plate tectonic motions. *Sea Technology*, **46**, 49–52.

K. Gagnon and C. D. Chadwell, and E. Norabuena, 2005: Measuring the onset of locking in the Peru-Chile trench with GPS and Acoustic Measurements. *Nature*, **434**, 205–208.

PRESENTATIONS

K. Gagnon and C. D. Chadwell, 2006: Geologic interpretation of shallow coupling at the Peru-Chile trench, *Subduction Zone Dynamics*, Montpellier, France.

K. Gagnon and C. D. Chadwell, 2006: Seafloor Geodetic measurements over the Nazca-South America thrust fault: results and implications, *European Geophysical Union General Assembly*, Vienna, Austria.

K. Gagnon and C. D. Chadwell, and E. Norabuena, 2005: Seafloor Geodetic Measurements Reveal Locking within 5 km of the Peru-Chile Trench at 12°S, *American Geophysical Union General Assembly*, San Francisco, CA, USA.

K. Gagnon and C. D. Chadwell, and E. Norabuena, 2004: Seafloor Geodetic Measurements of Nazca-South America Plate Stick-Slip Behavior, *American Geophysical Union Joint Assembly*, Montreal, Canada.

ABSTRACT OF THE DISSERTATION

Seafloor geodetic measurements and modeling of Nazca - South America plate convergence

by

Katie L. Gagnon
Doctor of Philosophy in Earth Sciences
University of California, San Diego, 2007
Professor C. David Chadwell, Chair

Campaign geodetic observations demonstrate shallow, interplate coupling along the thrust fault between the converging oceanic Nazca and continental South American plates. Delimiting the width of the seismogenic zone contributes to our understanding of the seismic and tsunamigenic nature of convergent plate boundaries. Here we locate the updip limit of the seismogenic zone using a combination of the Global Positioning System (GPS) and acoustic travel time measurements. Two seafloor transponder arrays were positioned in 2001 and 2003, providing plate motion vectors 20 and 50 km landward of the Peru-Chile trench axis at 12°S. Over 100 hours of GPS, acoustic and sound speed profiling data were gathered at each array, in each epoch, providing an estimate of plate motion with an uncertainty on the order of millimeters. I describe each component of the GPS-acoustic technique (GPSA), including static and kinematic GPS, GPS antenna-hydrophone baseline surveys, acoustic travel time measurements, sound speed profiling and moving surveys to determine a priori transponder position. Comparing these geodetic measurements with three dimensional kinematic models reveals coupling at less than 2 km depth. Seismic records, thermal models, and topographic analyses suggest that GPSA array displacements represent shallow, elastic strain accumulation.

Transponder relocation, another key component of this technique, consists of surveying a replacement transponder in the event that a transponder be-

comes inactive. I discuss the methodology and results of a transponder relocation, which contributed ±19 mm uncertainty to the final array vector. Optimal survey network geometry for a transponder relocation was determined in a simulation of the least-squares adjustment. Future relocations could decrease the contribution to array uncertainty to ±10 mm with improved survey geometry. Finally, complimentary investigations such as long-baseline kinematic GPS, transponder depth measurements and near-bottom acoustic surveys are included as necessary asides for the development seafloor geodetic observations.

I

Introduction

Interplate earthquakes occur along the seismogenic zone (SZ), where two converging plates are coupled along a convergent boundary. The SZ is initiated at the updip limit, undergoing a transition from stable to unstable, or aseismic to seismic sliding. It ends at the downdip limit with a transition back to stable sliding. This region has been traditionally studied by locating seismic rupture areas, with heat flow measurements and thermal modeling and with geodetic, seismic refraction and reflection, bathymetry and gravity observations.

The work presented here contributes plate velocity measurements at 20 and 50 km landward of the Peru-Chile trench axis. To help interpret the observations, I review our knowledge of the width of the seismogenic zone. Second, I present mechanical constraints on the seismic cycle. Finally, geophysical observations at the Peruvian margin are presented, which constrain the kinematic model parameters of the subduction zone at 12°S and provide background for the geologic interpretation of results (Chapter III).

I.1 Width of the seismogenic zone

The downdip limit has been investigated using the extent of coseismic faulting and interseismic geodetic data. Tichelaar and Ruff (1993) mapped the

inversion of teleseismic P-waveforms for earthquakes at circum-Pacific subduction zones with magnitudes larger than 6. Comparing coseismic rupture extent with inversions of tsunami data and geodetic models, they estimated the downdip limit at 40±5 km depth or 52-55 km in a few cases of complex faulting. Using coseismic rupture width, Pardo et al. (2002) found the downdip limit occurred at 60 km depth in central Chile.

The downdip limit has also been investigated with land-based geodetic observations, such as repeated survey lines, long-term tide gauge data, repeated precision gravity surveys and continuous GPS velocities. Norabuena et al. (1998) and Leffler et al. (1997) fit coastal GPS station velocities in Peru with a kinematic model locking the thrust fault from the trench axis to 50 km depth. Dragert and Hyndman (1995) monitored complex interseismic deformation patterns at the Cascadia subduction zone using an automated GPS tracking network and Tabei et al. (1996) measured uniform strain accumulation in SW Japan, indicating strong interplate coupling at the Nankai subduction zone. GPS measurements of coseismic displacement have also been used to monitor the extent of interplate coupling, such at the 1995 M8.0 event on the Northern Middle America Trench in Mexico. Tide gauge data and an 11-station regional GPS network showed widespread coastal subsidence, explained by anomalously shallow faulting, <15 km depth (Melbourne et al., 1997; Hutton et al., 2001).

Observations of the updip transition are complicated by low magnitude, shallow seismicity, which is not revealed in megathrust events. Ocean bottom seismometers (OBS) have been used to study shallow seismicity though they must observe the entire seismic cycle, often several decades, in order to determine the updip transition. Newman et al. (2002) used OBS's to locate 650 earthquakes over the period of 1 year off Nicoya peninsula, Costa Rica and predicted the updip limit to range from 10 to 20 km depth. Direct GPS measurements of plate motion above the updip portion of the thrust fault are hindered by the fast attenuation of electromagnetic waves in water. I present a combination of GPS and acous-

tic observations at the Peruvian margin which are modeled to show initiation of coupling at <2 km depth (Gagnon et al., 2005).

Forearc structure has also been used as an indicator of unstable portions of the fault. Byrne et al. (1988) argued that the morphological outer-arc high indicates the beginning of the strong, crustal backstop (Figure I.1). The backstop marks the lower limit of unconsolidated sediments of the accretionary prism and the beginning of unstable sliding. Wells et al. (2003) compared forearc structure to areas of high coseismic slip for 29 Circum-Pacific megathrust earthquakes. Subsidence of the forearc basin may occur by basal erosion, which they test for a possible link to seismogenesis. On average, they found that 71% of the seismic moment and 79% of the asperities (areas of highest slip) occurred beneath the gravity low of the deep-sea terrace and its basins. The correlation may be due to geologic features such as strong crust in the upper plate or subducted seamounts or sediment (Wells et al., 2003). Similarly (Song and Simons, 2003) correlated negative, trench-parallel gravity anomalies (TPGA) with regions where great earthquakes occur and positive anomalies with aseismic regions.

Thermal models at several subduction zones show that the depth of the updip transition coincides with the ∼100° isotherm and the downdip transition with the 350-450° isotherms (Figure I.2 and Figure I.1) (Ponko and Peacock, 1995; Hyndman et al., 1995; Hyndman and Wang, 1995; Oleskevich et al., 1999; Currie et al., 2002). Thermal model parameters include conductive and radiogenic heat flow, frictional heating, hydrothermal cooling, oceanic plate age, convergence rate, sediment thickness, dip angle and thermal properties of the overlying material. At 350°C, crustal rocks begin stable sliding and between 325-350°C, quartzofeldspathic rocks undergo a critical transition (Tse and Rice, 1986; Tichelaar and Ruff, 1993; Moore and Saffer, 2001). Above 450°, there is a change from brittle to ductile behavior. In between the two temperature limits is a region of conditional stability (Scholz, 2003). In some subduction zones, the 350-450°C isotherms are deeper that the maximum depth of recorded earthquakes. Dehydration reactions

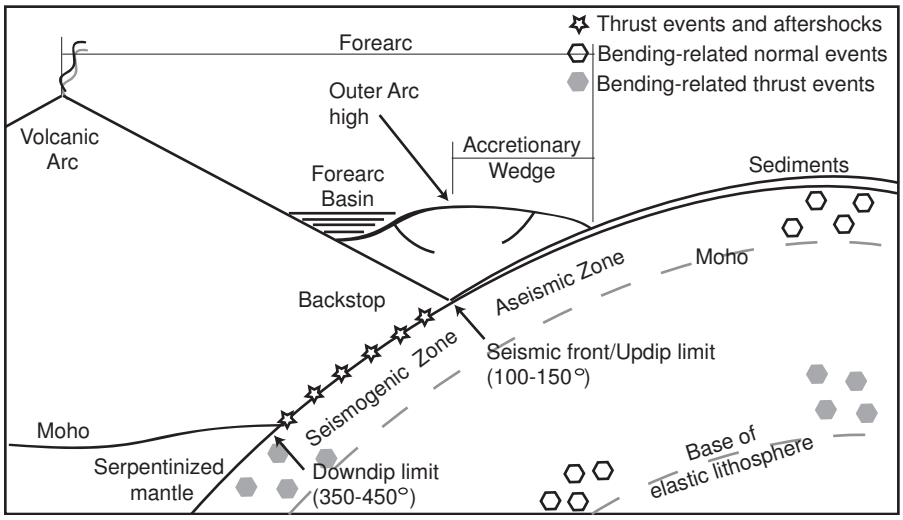

Figure I.1: Cross section of a subduction zone, adapted from (Byrne et al., 1988; Oleskevich et al., 1999). The updip limit, or seismic front, occurs beneath the outer-arc high of the crustal backstop. Thrust events and aftershocks are shown along the seismogenic zone and bending related earthquakes are shown in the downgoing plate. Approximate thermal limits for the updip and downdip transition are shown. The downdip limit may also coincide with the intersection of the thrust fault and the continental mantle.

at the intersection of the thrust fault and the continental forearc mantle corner (Moho) are thought to control the downdip limit, between 35-50 km depth (Ruff and Tichelaar, 1996; Oleskevich et al., 1999). Dehydration of the subducting slab introduces hydrous minerals to the forearc mantle such as talc and brucite, causing serpentinization of the forearc mantle. The forearc mantle may also form a permeability barrier (Hyndman et al., 1997; Peacock and Wang, 1999; Moore et al., 1997). The depths and distances from the trench axis to the 100°C, 350°C and 450°C isotherms and the Moho are shown in Table I.1. Shallow limits, such as in Mexcio, typically indicate a young, warm subducting oceanic crust.

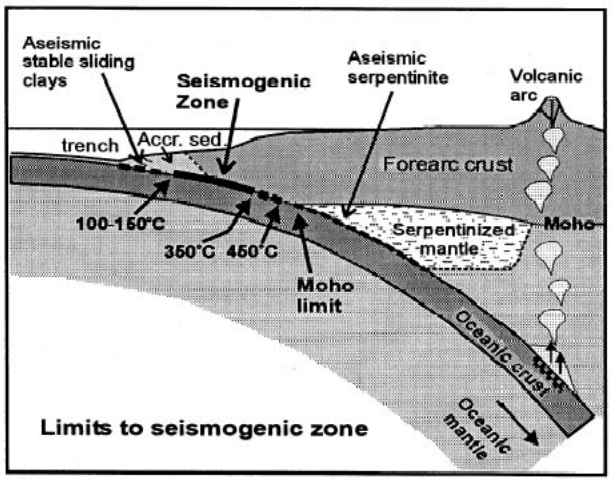

Figure I.2: The seismogenic zone is shown as a bold line on the thrust fault, from (Oleskevich et al., 1999). Dashed bold line shows the transition to the updip limit of the seismogenic zone, between 100-150°C, and the downdip limit, 350-450°C. Moho limit is shown at the intersection of the thrust fault and the serpentinized mantle.

The updip aseismic region reflects mostly unconsolidated sediments, particularly saturated clays, along the thrust fault that lack the strength to support a stress, (Marone and Scholz, 1988; Wang, 1980; Moore and Saffer, 2001). The transition from stable to unstable sliding is likely caused by a combination of diagenetic, metamorphic and fluid pressure related processes. The dehydration of stable sliding clays between 100-150°C causes cementation and consolidation and

Table I.1: Depth (km) and distance (km) to updip and downdip isotherms coinciding with SZ limits from thermal models

Region	100°C		350°C		450°C		Moho	
	Depth	Dist.	Depth	Dist.	Depth	Dist.	Depth	Dist.
Vancouver	5	5	12	55	21	100	35-40	150
Olympic Pen.	4	5	14	95	27	175	35-40	260
Columbia R.	5	5	14	70	29	130	35-40	160
MidOregon	5	5	14	65	27	115	35-40	145
Nankaido	12	30	20	140	32	185	33-35	220
Tonankai	14	30	23	120	38	155	33-35	165
S. Alaska	12	80	80	380	>100	>400	40-50	360
N. Chile	10-15	75	12	300	>100	>300	40-45	140
Taltal	10-15	70	12	240	80	>260	40-45	140
Coquimbo	10-15	>100	12	300	>100	>320	40-45	120
Valparaiso	10-15	>100	12	300	>100	>320	40-45	140
S. Chile	10-15	40	12	150	50	210	40-45	200
Jalisco	∼5	15-20	∼25	92	40	120	40	120
Oaxaca	∼5	15-20	∼30	110	40	160	40	160

creates velocity-weakening, or seismic, conditions. Figure I.3 shows porosity, fluid pressure and various mineral transitions as a function of depth. The dehydration of stable sliding clays, particularly smectite to illite, releases large amounts of water. The transition of smectite to illite clay (second column) was previously thought to increase strength and (Vrolijk, 1990) suggested that the transition coincided with the updip limit. Smectite is a hydrated phyllosilicate mineral, which is structurally weak and highly porous (Vrolijk, 1990). Saffer and Marone (2003) provided laboratory evidence for the velocity-stregthening (aseismic) behavior of both clays, suggesting that illite is stronger than smectite but not strong enough to initiate unstable sliding. Other diagenetic and metamorphic reactions include opal (siliceous radiolarian and diatom fossils) alteration to quartz at temperatures less than 100°C (Moore and Vrolijk, 1992) and low-grade metamorphism of unconsolidated sediments and cementation by zeolite, calcite and carbonate between 75-175°C (Ernst, 1990). Also, diffusive mass-transfer in siliciclasitc rocks, including pressure solution and precipitation followed by quart cementation, homogenizes

the rock fabric above 150°C (Byrne et al., 1988). Solid organic matter is transformed to fluid between 100-150°C, generating hydrocarbon which can be observed migrating out of surface seeps (Oleskevich et al., 1999; Moore and Saffer, 2001).

Porosity collapse during consolidation, metamorphic dehydration reactions and hydrocarbon generation releases fluids into the accretionary complex and underthrust sediment as well as the overriding crust and mantle from the trench axis to over 200 km depth (Peacock and Wang, 1999). At the updip portion of the thrust, high fluid pressures may contribute to stable sliding (Brown et al., 2001, 2003; Moore and Saffer, 2001). The updip transition from stable to stick-slip behavior may be related to a declining fluid pressure (P) ratio,

$$\lambda^* = \frac{P_{fluid} - P_{hydrostatic}}{P_{lithostatic} - P_{hydrostatic}}, \tag{I.1}$$

decreasing fluid production potential and increasing mechanical strength. Stable sliding may be fueled by the addition of fluid from several sources. The majority of porosity losses, or sediment consolidation, occurs within 5 km of the sediment-water interface and releases the largest amounts of water (Moore and Vrolijk, 1992). Mineral dehydration, particularly during the dissolution of smectite and opal-A to opal-CT to quartz, also releases water into the system. For example, 35% of the original volume of smectite and 23% opal is released as water (Moore and Vrolijk, 1992). Some water may also be release from hydrous, zeolite-greenschist facies minerals in the oceanic crust created by hydrothermal alteration or from water trapped in pores and fractures (Kastner et al., 1991; Moore and Vrolijk, 1992). The generation of methane at depth can cause increased fluid pressure as it moves upward in a low-permeability fabric. Fluid pressure is also increased by the exsolution of methane from upward migrating, supersaturated water, volume expansion and carbon dioxide generation from organic matter. Carbon dioxide can also be generated from underthrust limestone, though little evidence has been found to show that it is a significant contributor of fluid to the accretionary complex (Moore and Vrolijk, 1992).

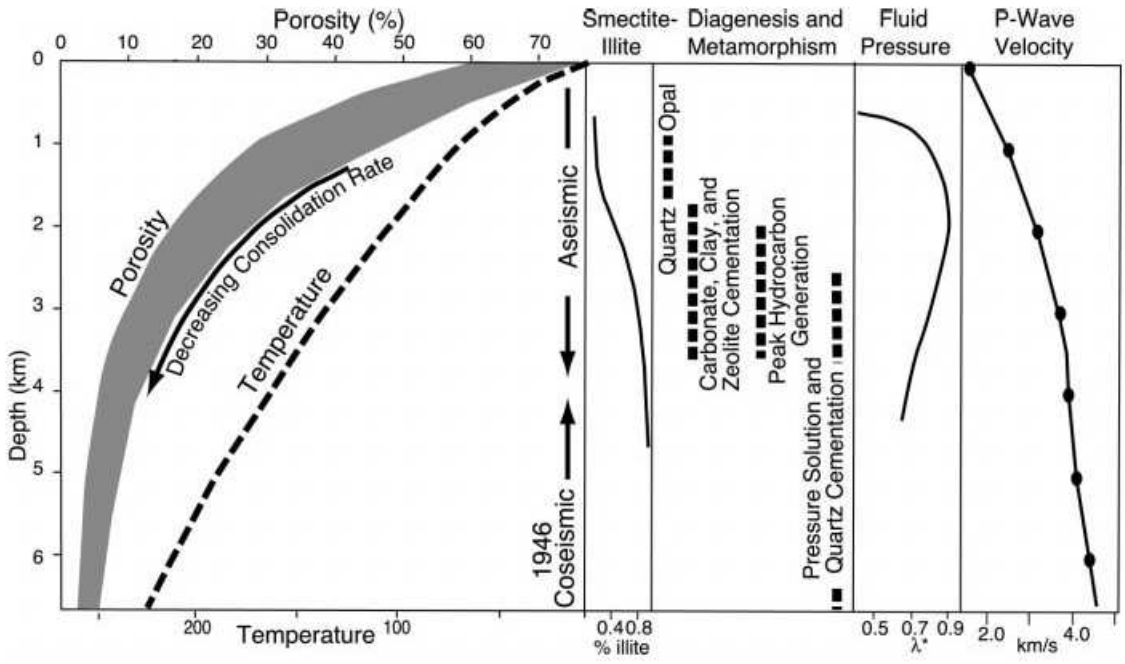

Figure I.3: Depth dependent properties affecting the updip limit of the seismogenic zone including porosity and temperature, smectite-illite transition, diagenetic/metamorphic/structural transitions of several minerals, fluid pressure (see Equation I.1) and increasing P-wave velocity. Temperature, porosity, and seismic wave velocity represent the hanging wall above the thrust fault in the central Nankai subduction zone (Moore and Saffer, 2001).

I.2 Modeling subduction

Thrust faults can be modeled with a dislocation model using convergence rate and direction. Savage (1983) presented a model for strain accumulation and release by superimposing steady state subduction and repeated slip events in an elastic half space (Figure I.4). This type of model requires information on the width of the seismogenic zone, or the updip and downdip boundaries of seismic slip.

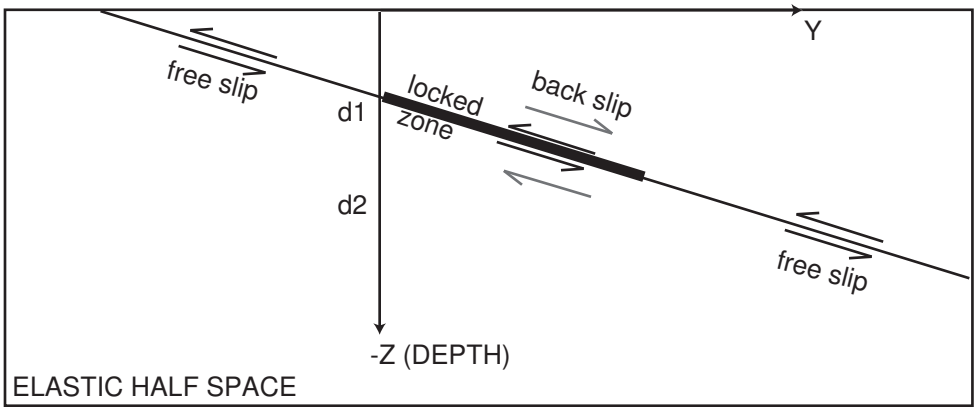

Figure I.4: Kinematic, elastic half space model of a thrust fault. Back slip along the locked zone (bold) is superimposed on steady state free slip to show strain accumulation (Savage, 1983). The locked zone is delimited by updip limit depth, $d1$, and downdip limit depth, $d2$.

Mechanical models investigate thrust fault dynamics in terms of frictional slip stability. Several studies at subduction zones show complex along and across strike variations in slip, or friction on the thrust fault (Lay and Kanamori, 1981; Byrne et al., 1988; Pacheco et al., 1993; Wells et al., 2003; Song and Simons, 2003). Scholz (2003) defined a stability parameter, $\xi = (a-b)\sigma_n'$, where $(a-b)$ is the velocity dependence of sliding friction and σ_n' is the effective normal stress. Velocity strengthening materials, positive $(a-b)$, exhibit an increase in frictional resistance with sliding velocity, creating aseismic or stable sliding conditions (Saffer and Marone, 2003; Scholz, 1998). Velocity weakening materials, negative $(a-b)$,

have a decrease in frictional resistance with increasing velocities, creating unstable slip or seismogenic behavior. Scholz argues that earthquakes can only nucleate in the unstable condition and can extend into areas that are conditionally stable. Earthquakes that propagate into the stable region will have a negative stress drop, which will stop propagation. A model for stability at crustal faults and subduction zones versus depth is plotted in Figure I.5, where k represents stiffness. The stability parameter transitions from positive to negative at the updip limit. Earthquake distribution at crustal faults is shown to the right. Pacheco et al. (1993) defined the seismic coupling coefficient, α=seismic slip/total slip, for 19 subduction zones. Low values of α represent stable slip along the thrust fault with little seismic activity, including the Marianas arc and Java. High values of α represent unstable surrounded by conditionally stable regions, including portions of the Central and South America, Tonga, Vanuatu and Japan trenches.

The Coulomb wedge theory describes the thrust fault under constant shear stress as a wedge in critical state, allowing an exact stress solution (Davis et al., 1983; Dahlen, 1990). Wang and Hu (2006) modeled a dynamic Coulomb wedge to include both interseismic locking and coseismic slip. The wedge material is elastic-perfectly Coulomb plastic, meaning stress increases linearly with strain until the yield envelope. Further deformation is plastic, with constant stress and increasing strain. Figure I.6a and b show a profile of the subduction zone while I.6c shows the time-varying stable-unstable updip transition beneath the accretionary prism. They suggest that the topography of the outer wedge is controlled by the strength of the velocity-strengthening material on the updip portion of the thrust fault. The updip limit of the seismogenic zone is the transition from outer (seaward) to the inner (landward) wedge. The solution depends on slope angle, α, basal dip, β, and the fluid pressure ratio, λ. Figure I.7a, b, and c show the stress cycle for the Nankai accretionary prism in coseismic, postseismic, and interseismic conditions, respectively. In the coseismic period, basal friction peaks beneath the outer wedge and reaches a minimum beneath the inner wedge. After the coseismic

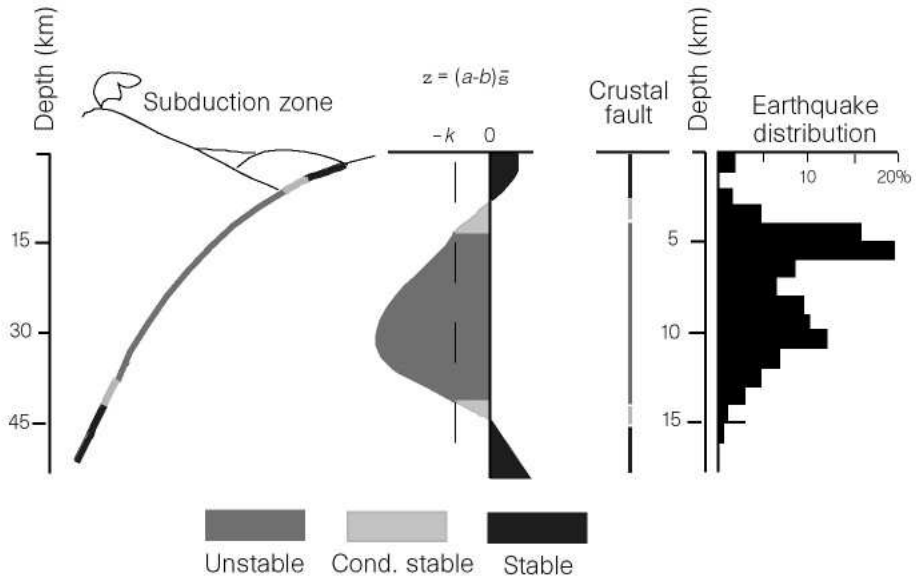

Figure I.5: Depth versus stability parameter $(a - b)$ at a subduction zone (first column) and crustal fault (third column) (Scholz, 1998). Histogram of earthquake distribution with depth (on the right) is for a crustal fault. Beneath the forearc basin the fault is stable, or $(a - b)$ is positive (dark gray). In the seismogenic zone the fault is unstable, or $(a - b)$ is negative (medium gray). In conditionally stable regions, $(a - b)$ is between 0 and $-k$ (light gray).

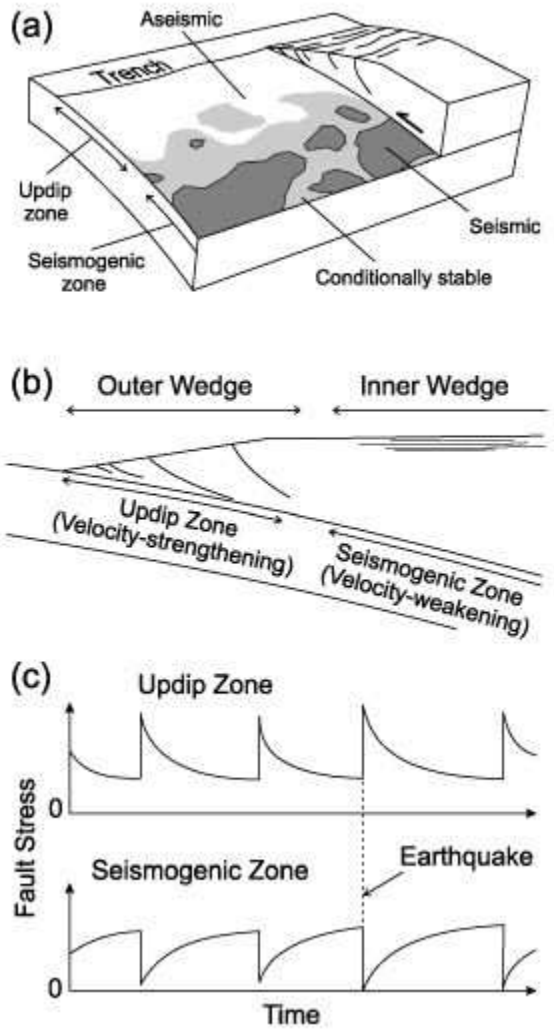

Figure I.6: a) Thrust fault highlighting regions that are stable (white), conditionally stable (light gray) and unstable (gray) (Wang and Hu, 2006). Patches of unstable regions extend towards the trench axis and are known as asperities. b) Cross section of the thrust fault showing velocity-strengthening (increasing friction with increasing slip) outer wedge and velocity-weakening (decreasing friction with increasing slip) inner wedge. c) Stress on the fault versus time. The updip zone experiences a peak in stress during coseismic events and relaxes during the interseismic period. The seismogenic zone experiences increasing stress during interseismic periods with a stress drop during coseismic events.

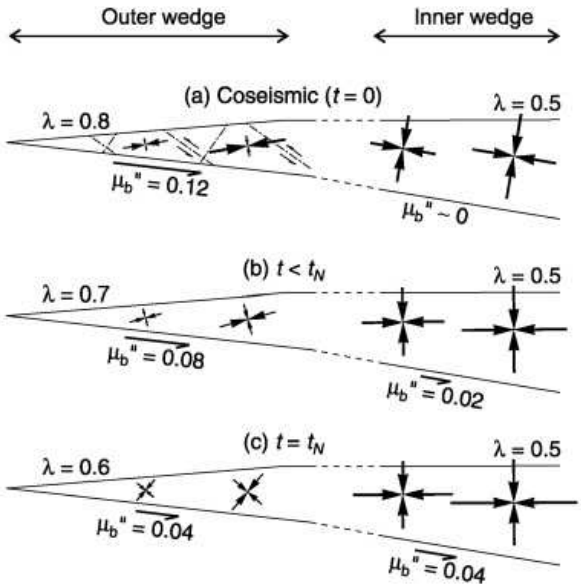

Figure I.7: Principal stresses during the seismic cycle with respect to the outer and inner wedge, based on (Wang and Hu, 2006). Time t_N represents the relaxation time of the outer wedge. Fault geometry is from the Nankai trench. (a) Coseismic event, $t = 0$. Outer wedge is in a critical state with maximum basal friction, $\mu_b^{"}$ and elevated pore fluid stress, λ. Inner wedge experiences a minimum basal friction during slip. b) Postseismic stage. Outer wedge is relaxed and inner wedge compressed. c) Interseismic stage at $t = t_N$. Outer wedge is neutral and inner wedge experiencing increasing shear stress, τ_n.

event, the outer wedge relaxes and the inner wedge begins to accumulate elastic strain. During the interseismic period, shear stress on the locked zone approaches fault strength. The outer wedge has a minimal basal friction and pore fluid pressure (Wang and Hu, 2006). They note that the topographic signature of the updip limit is abrupt for certain thrust faults. The distinctness may represent the width of the transition zone from the aseismic to seismic portion of the thrust fault, where the geometry of the accretionary wedge is a function of the peak strength of the outer wedge. Similar conclusions on the correlation between topography and the updip limit were presented by Byrne et al. (1988). This model also suggests that the updip limit is transitional over many seismic cycles.

Davis et al. (2006) created a model of relaxation and contraction in the accretionary prism based on obsevations from terrestrial borehole accelerometers and velocity seismometers. They observed a swarm of low-frequency earthquakes concurrent with relaxation of the incoming plate and contraction of the outer prism. Figure I.8 shows a stress cycle that could explain the observations. The interseismic period (A) is dominated by contraction outside of the locked zone and relaxation in the accretionary wedge. Coseismic slip (B) then propagates updip and reverses the process, loading the accretionary prism in contraction. Both Wang and Hu (2006) and Davis et al. (2006) treat the accretionary wedge as a material that can store elastic energy. This will be an important feature of the geologic interpretation of GPSA results in Chapter III.

I.3 Nazca-South America plate convergence

The Peru-Chile trench axis, roughly 150 km offshore and 6-7 km below sea level, marks the interface of the Nazca and South America plates, Figure I.9. Significant shortening of the west coast of South America has produced the Andean chain, 7000 km along strike, with the widest series of mountain ranges at the Arica Bend, $\sim$17°S. The Andean chain in the Cenozoic experienced quiescent

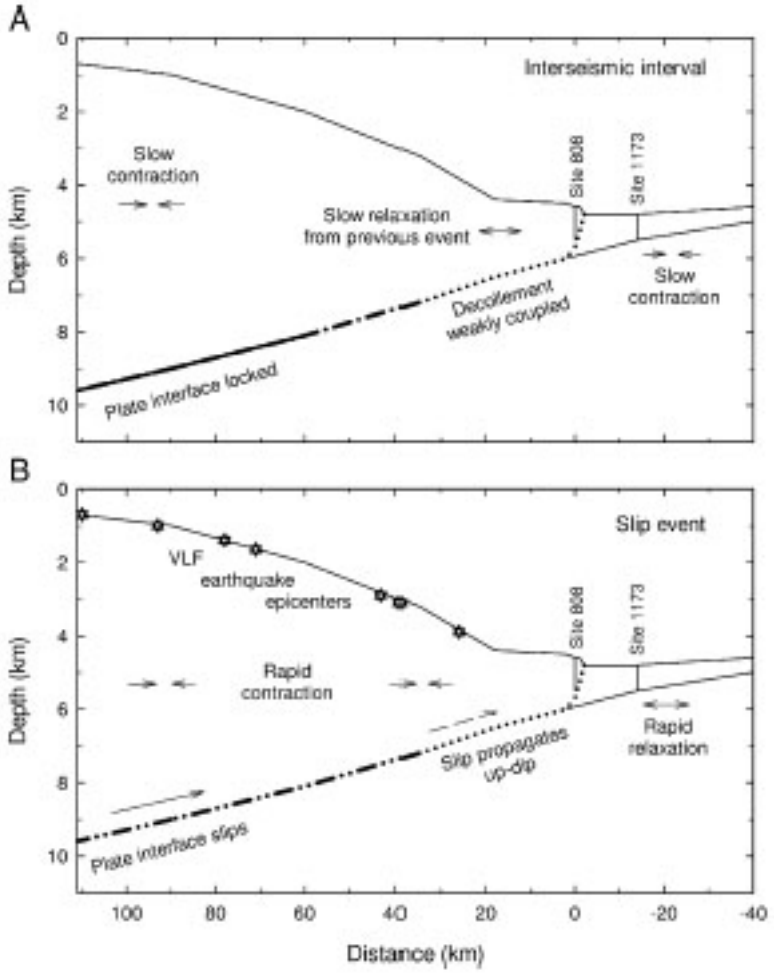

Figure I.8: Interpretation of borehole accelerometer and velocity seismometer observations between the Eurasian and Phillippine Sea plates (Davis et al., 2006). A) Interseismic interval includes contraction above the locked interface and relaxation, or dilation, above the weakly coupled, shallow portion of the thrust fault, concurrent with Wang and Hu (2006) model, at Site 808. B) Aseismic slip on the thrust, which induced a swarm of very-low-frequency (VLF) earthquakes (< M4) in the overlying material, produced contraction above the decollement and some dilation in the incoming plate.

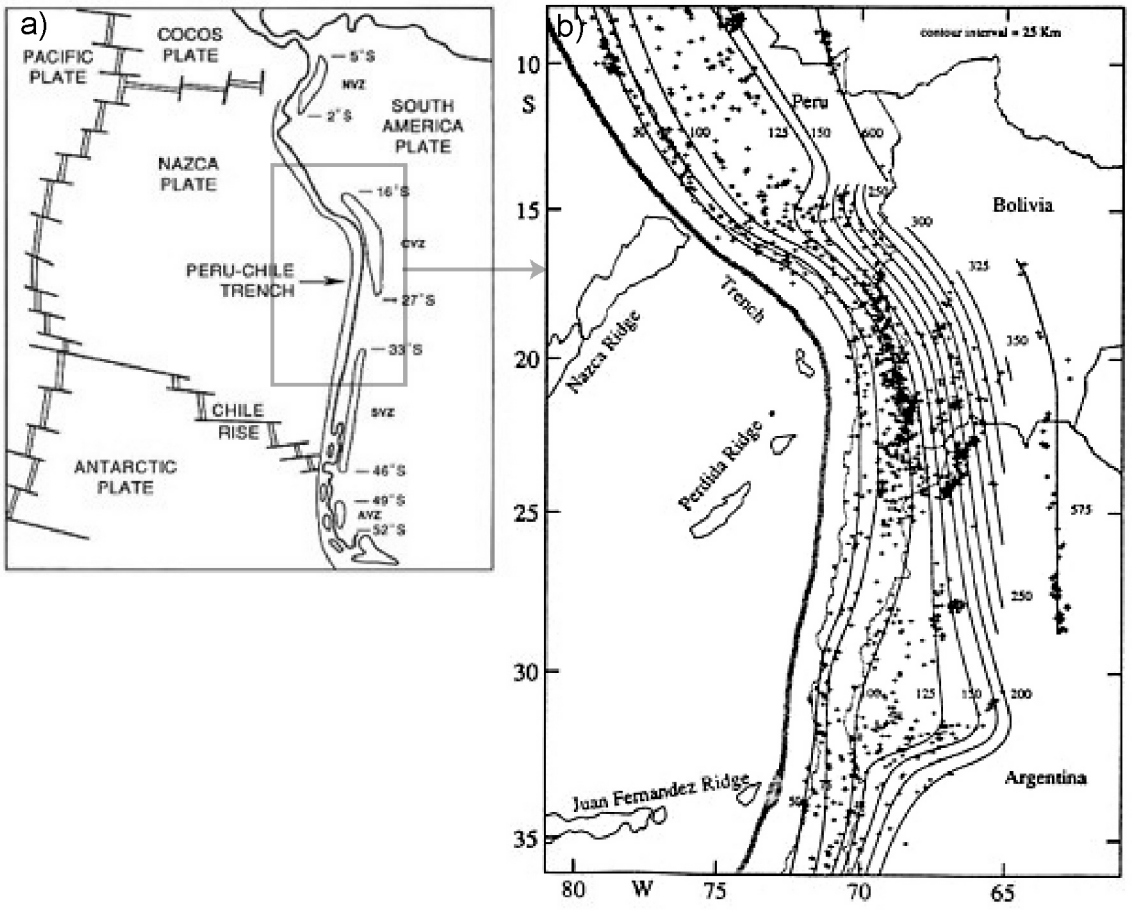

Figure I.9: a) Map of tectonic plates. Convergence between the Nazca and South America plates is marked by the Peru-Chile trench. Volcanism along the convergent margin is grouped into the Northern, Central and Southern Volcanic Zones (NVZ, CVZ and SVZ, respectively). b) Contours of the subducted plate show a decrease in dip, or flat slab subduction, in southern Peru (10°) and northern Chile (30°S) at roughly 100 km depth (Cahill and Isacks, 1992). Earthquake epicenters, used to determine depth contours, are shown as black crosses.

periods of weak deformation (Oligocene, ∼30 Ma), high convergence rates and large volume magmatism (Miocene, ∼23 Ma), and uplift and crustal shortening due to convergence and the westward drift of the South American plate (Sebrier and Soler, 1991). Currently, uplift of the Eastern Cordillera and Subandean zone by underthrusting of the Brazilian Shield is dynamically supported by shortening, with highly debated rates of shortening estimated between 2 and 15 mm/yr (Wdowinski and Bock, 1994; Leffler et al., 1997; Norabuena et al., 1999). Figure I.9 also shows a cross section from the trench axis to the cratonic interior across the Central Volcanic Zone (CVZ), ∼ 20°S. Geologically, the cross-section includes suspect terrains near the coast, volcanics in the Western Cordillera, volcanoclasitc and lithoclastic fill in the 4 km-wide Antiplano-Puna plateau, metamorphic fold and thrust belts in the Eastern Cordillera and Subandean zone, and the low lying Brazilian shield about 200 m above sea level. The converging oceanic Nazca and continental South America plates are part of the Circum-Pacific Ring of Fire, responsible for 76% of the annual, global seismic energy release (Bolt, 1993). The Peru-Chile thrust fault is one of the most active faults in the world, with an M 8.0 recurrence interval of 10 years (Bevis and Martel, 2001).

The Peru-Chile margin can be broken into five segments based on dip of the downgoing plate, seismic and volcanic activity, tectonic erosion/accretion and seafloor structure. Barazangi and Isacks (1976) first observed along-strike variations in dip by locating the Benioff zone. The subducting lithosphere undergoes two unique changes at 10°S and 30°S, revealed by the depth of earthquake hypocenters (Figure I.9). Flat slab subduction is characterized by a broad zone of seismicity and the absence of volcanic activity in the Holocene. The dip maintains 10°-15° from the trench axis to 100 km depth before flattening out for several hundred kilometers and finally descending into the mantle. Three regions of steep subduction are located at the northern, central and southern volcanic zones where the plate dips at 30°. Gutscher (2002) showed that seismic energy is roughly 5-10 times greater over flat slab segments, with greater interplate coupling possibly

caused by a colder forearc.

The Nazca Ridge intersects the trench axis at 15°S. Due to oblique convergence, it has migrated south at roughly 75 km/myr. The onset of ridge subduction occurred at 9°S, ∼11 Ma (Hampel, 2002). During ridge subduction the margin experienced forearc uplift and extensive tectonic erosion followed by subsequent growth of an accretionary prism (Hampel et al., 2004; Clift et al., 2003; von Huene et al., 1996; Kukowski et al., 1994). Over the last 11 Ma, the prism between 9-12°S has grown to 10-15 km wide (von Huene and Lallemand, 1990; von Huene et al., 1996). Several studies argue that erosion has been the dominant regime at this margin, as evidenced by large margin taper and a small frontal prism (Kukowski et al., 2001; Clift et al., 2003; Hampel et al., 2004).

The relationship between tectonic erosion and stick-slip behavior has been investigated at several sites along the Peru-Chile margin (Schweller et al., 1981; Warsi et al., 1983; Wortel and Cloetingh, 1985; von Huene and Lallemand, 1990; von Huene et al., 1996; von Huene and Ranero, 2003; Sallares and Ranero, 2005). Seismic refraction and reflection, side scan sonar and ODP/DSDP cores show evidence of subsidence and extensive frontal erosion along the portions of the Peruvian margin. Frontal and basal erosion of the overriding plate contributes fluid and debris to the thrust fault and can deepen the updip limit by increasing pore fluid pressure (von Huene and Lallemand, 1990; Sallares and Ranero, 2005).

Extensional forearc basins along the continental shelf are feature of the convergent margin. Ponded sediments, several km thick, have accumulated in the Trujillo and Yaquina basins at 9°S, the Salaverry and Lima basins between 10-12°S and the West Pisco basin at 14°S. Data from ODP leg 112 and mutichannel seismic reflection profiles suggest the basins were formed as a result of tectonic erosion and subsidence, which accelerated with the passing of the aseismic Nazca Ridge (Clift et al., 2003).

GPS station velocities have been used to construct kinematic models of interseismic deformation along the Peruvian margin. Figure I.10 shows campaign

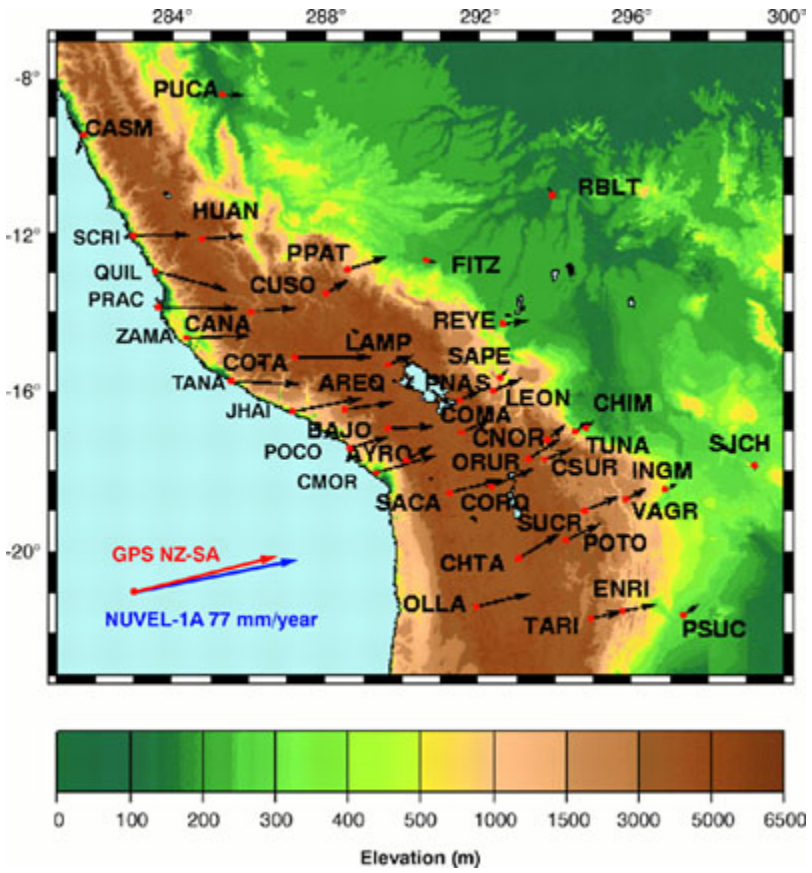

Figure I.10: Campaign GPS station velocities in Peru. Stations operated by Instituto Geofisico del Peru. Space geodetic data, including GPS, SLR and DORIS, provide an estimate of Nazca-South America plate convergence (red) at 75±5 mm/yr, comparable to NUVEL-1A (blue). All rates are relative to stable South America (Norabuena et al., 1999). Converge

GPS station velocities relative to stable South America (Norabuena et al., 1999). Figure I.11 shows elastic half space models with various locking scenarios. Norabuena et al. (1999) fit GPS velocities with a model representing 30 mm/yr of partial locking (part of the 75 mm/yr convergence is accommodated by stable sliding) from the trench axis to 50 km depth and 15 mm/yr shortening in the Sub-Andean fold and thrust belt (FTB). Leffler et al. (1997) fit GPS station velocities with a model of full locking from the trench axis to 20 km depth and little to no shortening (0-3 mm/yr). The results in the following chapters will further

help differentiate between kinematic models by providing plate velocities at 20 and 50 km from the trench axis and using updated absolute rotation poles and fault geometry.

The seismically active region between 10-14°S has produced several tsunamis. The southern coast of Peru has a high tsunami risk as Lima is closer to a major convergent plate boundary than any other city of comparable size in the Americas (Degg and Chester, 2005). On February 21, 1996, a tsunami occurred at 9.59°S, 79.59°W at 10 km depth, roughly 200 km north of the GPS-acoustic site. Figure I.12 shows several types of subduction-related earthquakes in the oceanic and continental plates. (Kanamori, 1972) defined tsunami earthquakes as having concentrated slip near the trench axis. The resulting tsunamis are consistently larger than expected for the magnitude of seismic waves. Several theories exist for how they are generated: a long and slow rupture (Kanamori, 1972), slip in the accretionary wedge (Fukao, 1979) or by a decrease in rigidity along the upper portions of the thrust fault (Bilek and Lay, 1999). Complex frictional properties of some clays and/or patches of anomalous pore fluid pressure are thought to occasionally allow slip updip of the seismogenic zone (Seno, 2002; Bilek and Lay, 1999).

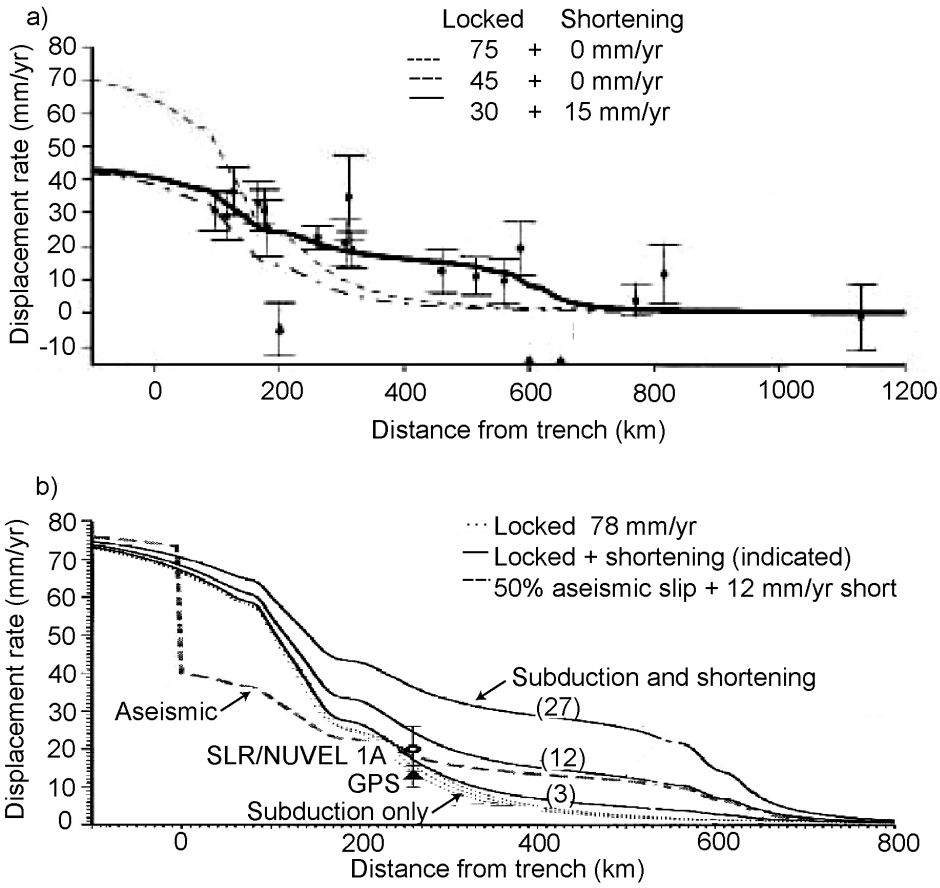

Figure I.11: a) Norabuena et al. (1999) kinematic, elastic half space models for convergence rate 75 mm/yr at 80°. Data points show GPS station velocities and 1-σ uncertainties from Figure I.10. The best fit model includes partial locking on the thrust fault (30 mm/yr) and shortening across the margin (15 mm/yr). b) Leffler et al. (1997) kinematic, elastic half space models for convergence rate 78 mm/yr at 80° compared to Arequipa GPS and satellite laser ranging (SLR) data relative to stable South America. Best fit model shows full locking from the trench axis to 20 km depth and little to no shortening (0-3 mm/yr). Solid line includes surface horizontal displacement from strain accumulation and shortening, number in parenthesis describes rate of shortening. Dashed line shows stable sliding, or aseismic conditions on the thrust fault. Surface displacement without shortening is shown as thin, dashed lines.

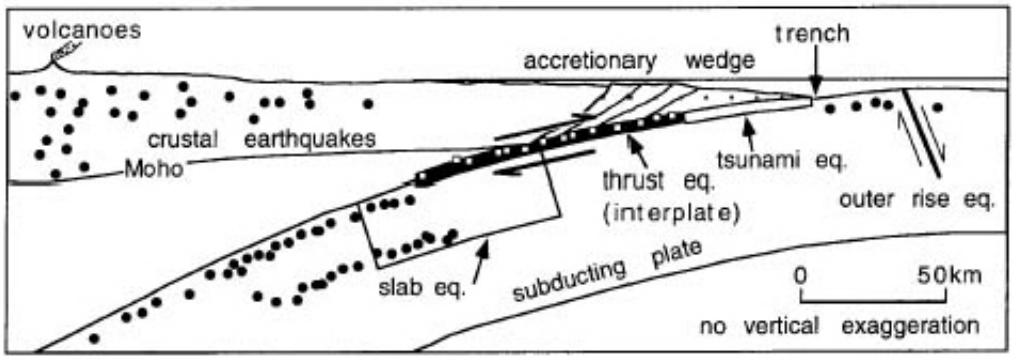

Figure I.12: Profile of a subduction zone showing the location of tsunami earthquakes on the shallow, updip portion of the thrust fault. Other types of earthquakes associated with this region are thrust and interplate earthquakes between 10 and 40 km depth, outer rise earthquakes in the downgoing plate and crustal earthquakes in the backarc (Satake and Tanioka, 1999). Locked zone is shown in bold.

II

GPS-acoustic technique

The GPS-acoustic (GPSA) technique employs kinematic GPS (Global Positioning System) on a ship and acoustic signals from a ship to an array of precision acoustic transponders on the seafloor (Figure II.1) to estimate horizontal seafloor plate motion. Scripps Institution of Oceanography (SIO) began GPS-acoustic campaigns to measure the motion of a rigid transponder array at the North Cascadia subduction zone in 1991 (Spiess et al., 1998). This provided a measurement of the Juan de Fuca - North America plate convergence between 1994 and 1996 with a repeatability of $\pm$39 mm east and $\pm$8 mm north after roughly 30 hours of data collection in each epoch. Four additional sites were created to investigate various forms of crustal deformation as well as further develop the technique. One array was created on the South Cleft segment of the Juan de Fuca ridge to investigate plate motion 25 km east of the spreading ridge (Spiess et al., 2000). Another, 150 km west of Newport, Oregon, on the subducting Juan de Fuca plate, was employed to study convergence over the South Cascadia subduction zone. Seven transponders were deployed on the slope of the Hilina fault system of Kilauea volcano to study aseismic submarine slumping (Hildebrand et al., 2000; Phillips and Chadwell, 2005). Finally, the subject of this dissertation, two transponder arrays were installed 20 and 50 km landward of the Peru-Chile trench axis to determine the magnitude of horizontal deformation above the subduction zone. After roughly 100

hours of data collection at each array the repeatability was ±5 - 7 mm (Gagnon et al., 2005).

The GPSA technique involves three or four precision acoustic transponders, arranged in a triangle or square, inscribed on a circle with radius equal to the nominal water depth (Spiess et al., 1998). The transponder spacing is a tradeoff between shorter baselines allowing ray paths through similar sound speed profiles at the surface and longer baselines increasing geometric strength (Spiess et al., 1998). The precision acoustic transponders (PXPs) are typically allowed to freefall from the ship or, in steep or rough terrain, placed with a tethered control vehicle operated remotely from the ship. The sound speed profile is assumed to be horizontally stratified and is repeatedly measured during GPSA data collection by casting a CTD package (conductivity-temperature-depth). The transponder arrays are typically 2 to 4 km deep, allowing roughly 2 CTD casts per hour. The ship is held near (∼10 m) the acoustic center, where the acoustic launch angle is the same from the ship to each transponder. This helps negate unmodelled changes in the sound speed by ensuring that the ray paths are uniformly spaced at the surface, where the majority of variability occurs. As a result, sound speed variability in the upper water column will appear to shift the array's position vertically but not horizontally. In addition, holding station for several days helps average out any of the affects from sloping isopycnals due to internal waves. The data sets required to obtain the final PXP positions are outlined in Table II.1. Three GPS antennas are mounted on a ship and collect data at 1 Hz (Section II.1). The GPS antenna positions are transferred to a well-mounted hydrophone at each acoustic transmit and receive via a daily shipboard survey (Section II.2). The range of the acoustic signal from the hydrophone to each transponder is determined by performing a ray trace with the travel time and an average sound speed profile. An initial moving GPSA survey provides the a priori horizontal position of each transponder with an uncertainty of ±200 mm and the vertical position with a repeatability of 1 meter (Section II.4.A). The depth is also independently measured with an acous-

tic/optical seafloor survey instrument with an uncertainty of ±30 mm (Section V.2). The absolute position of the array is determined by holding the baselines of each transponder pair fixed, treating the array as a rigid plate, and minimizing the acoustic range residuals in a least-squares adjustment (Section II.4.B). The average positional difference of the transponders between epochs represents horizontal plate motion with an uncertainty on the order of mm in the International Terrestrial Reference Frame (ITRF). Figure IIB shows the displacement of the array from epoch t_0 to t_1 expressed in latitude (ϕ), longitude (λ) and height (H). The plate motion vector will then be,

$$\mathbf{P} = \frac{\mathbf{A} + \mathbf{B} + \mathbf{C}}{3}, \tag{II.1}$$

where

$$\mathbf{A} = (\phi, \lambda, H)_{At_1} - (\phi, \lambda, H)_{At_0}, \tag{II.2}$$

$$\mathbf{B} = (\phi, \lambda, H)_{Bt_1} - (\phi, \lambda, H)_{Bt_0}, \tag{II.3}$$

$$\mathbf{C} = (\phi, \lambda, H)_{Ct_1} - (\phi, \lambda, H)_{Ct_0}, \tag{II.4}$$

such that **A**, **B** and **C** are vectors for the displacement of transponders A, B and C, respectively.

Table II.1: Data types, frequency of collection and uncertainty, $^{+}$(Watts, 2000)

Data type	Period	Uncertainty
Kinematic GPS	1 sec	±20-30 mm
Acoustic signal	40 sec	±5 μs
Sound speed	1 sec	±0.6 m/s
Tidal height	20 sec	±0.2 ppm
Barometric pressure	1 sec	±0.05 mbar
Transponder depth	1 year	±30 mm
Ship survey baselines	1 day	±2-3 mm
Conductivity (CTD)	1 sec	±0.005^{+}
Temperature (CTD)	1 sec	±.005K^{+}
depth (CTD)	1 sec	±.15 % full depth^{+}

Several organizations in Japan have used a combination of GPS and

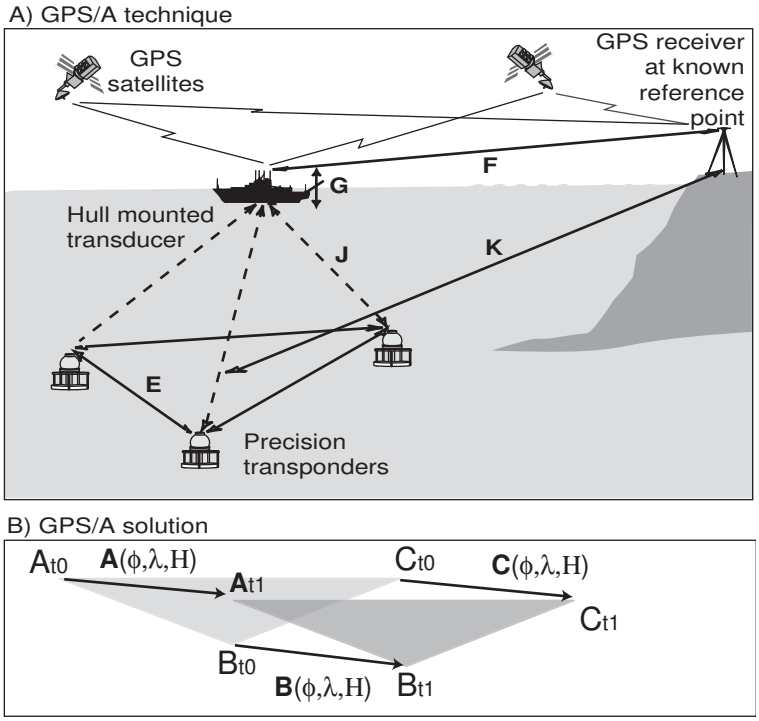

Figure II.1: A) The GPS-acoustic approach to measure seafloor motion. Three precision transponders are deployed around the circumference of a circle with a radius equal to the nominal water depth. The transponders are spaced several kilometers apart and the relative positions **E** are measured by performing a moving GPSA survey (circle drive). Dual-frequency GPS carrier phase data sampled at 1 Hz at the ship and onshore provide the connection to sub-aerial reference stations **F**. An optical survey connects shipboard GPS antenna phase centers to the acoustic hydrophone phase center **G**. Two-way travel times of acoustic signals are collected between the ship and the transponder array **J**. Vectors **E**, **F**, **G** and **J** combine to determine the horizontal components of **K**. Maintaining the ship near the array center assures that acoustic velocity variations are primarily a function of depth and do not bias the horizontal components of **A**. Survey times range from 80 to 120 hours in order to achieve centimeter-level positioning. B) Displacement of a rigid array of transponders a, b and c from time t_0 to t_1. The position of each transponder is made up of the absolute latitude, ϕ, longitude, λ and height, H.

acoustic measurements to study crustal deformation. Tohoku University used the GPSA approach from a towed buoy to measure an array with ±50 mm of seafloor deformation after 48 hours at Kumano-nada in the Nankai trough (Kido et al., 2006). Jointly, the Univ. Tokyo, Tohoku University and SIO demonstrated array positioning of ±30 mm east and ±31 mm north after roughly 18 hours of GPSA data on the slope of the Hilina fault system in Kilauea (Osada et al., 2003).

The Hydrographic and Oceanographic Department of Japan (JHOD) and the Institute of Industrial Science, Univ. Tokyo (IIS) have installed over 15 seafloor reference points. At the Japan trench off the Miyagi Prefecture, seven GPSA campaigns were performed to individually position an array of four transponders from 2002 to 2005. The resulting RMS variability for one day solutions, averaging the four transponder positions, ranged from ±37 - 117 mm east and ±48 - 114 mm north with 48 - 192 hours of data (Fujita et al., 2006; Funakoshi et al., 2005). Yamada et al. (2002) performed an error evaluation for single transponder positioning with uncertainties on the order of 180 mm using numerical simulations. Obana et al. (2000) has also used kinematic GPS and acoustic ranging to individually locate two transponders off the coast of Shirahama, southwest Japan and in Sagami Bay, central Japan. They estimated the positions of the individual seafloor transponders with 5 hours of data collection at each site. The standard error was estimated as ±220 mm east and ±150 mm north at the shallow site and ±170 mm east and ±120 mm north at the deep site.

This work focuses on two transponder arrays, installed at 12°S, offshore Lima, Peru in 2001 and resurveyed in 2003. They are 20 and 50 km east of the Peru-Chile trench axis as shown in Figure II.2. These distances were chosen based on a kinematic model of land geodesy data, which showed the updip limit of locking on the thrust fault within 50 km of the trench axis. This section includes a description of GPS, sound speed and acoustic data collection techniques and the analysis used to determine plate motion at the two arrays.

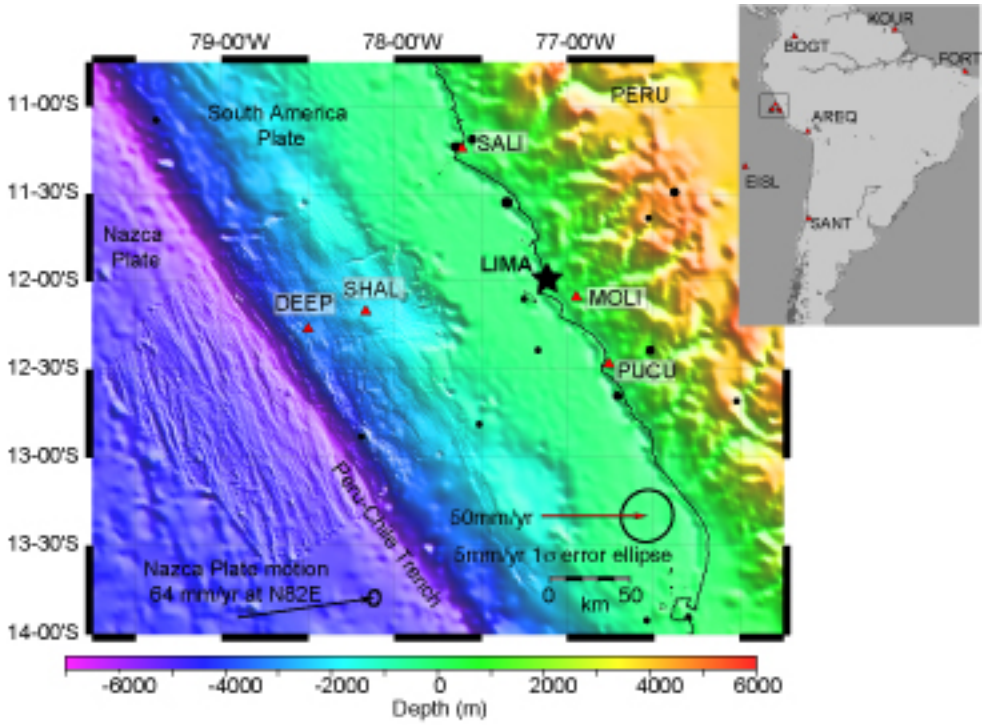

Figure II.2: Topographic map of Peruvian margin. Yellow triangles show campaign, land GPS stations at Pucusana (PUCU) and Salinas (SALI). Red triangles represent deep and shallow transponder arrays 20 and 50 km from the Peru-Chile trench axis. Bathymetric data was collected in 2001 and 2003 from R/V Roger Revelle using SIMRAD EM 120. Land topography shown from E4 TOPO (Smith and Sandwell, 1997). Black circles represent earthquakes from the USGS/NEIC PDE solutions between data collection periods. The REVEL plate convergence vector (64 mm/yr at N82E) is shown relative to stable South America (Sella et al., 2002). Inset shows distant low-rate GPS stations (red triangles) Arequipa (AREQ), Bogota (BOGT), Galapagos (GALA), Kourou (KOUR), Fortaleza (FORT) and Santiago (SANT).

II.1 GPS component

Kinematic GPS was used to position the seafloor transponder arrays with respect to campaign, coastal GPS stations, roughly 150 km east. The coastal stations were, in turn, positioned relative to continuous, distant ($\gg$100 km) stations on the stable South America craton. GPS data were processed with NASA's Jet Propulsion Lab GIPSY/OASIS II software with modeling approaches developed at Scripps Institution of Oceanography (Webb and Zumberge, 1997; Chadwell et al., 2002; Spiess et al., 1998). All GPS receivers recorded L1 and L2 pseduorange and P1 and P2 carrier phase data. The dual frequencies allowed for the elimination of ionospheric affects. Together, the stations formed a double-differenced phase observable, such that the satellite/receiver clock errors and satellite/receiver hardware delays were cancelled over short baselines, allowing for the solution of fixed integer ambiguity. When combined with the daily ship surveys of antenna-hydrophone baselines, these data provide the position of the ships hydrophone referenced to the land-based GPS network at each second. Below is a discussion of the static and kinematic processing techniques and methods for canceling the effects of GPS phase wrap.

II.1.A Static GPS

Static, terrestrial GPS observations have become a key component of crustal deformation studies over the last decade. Several of the processing techniques outlined here have been used in a variety of studies (Feigl et al., 1993). Distant, low-rate (30 sec.) GPS stations were used to determine the daily position of coastal stations in ITRF00 during GPSA operations offshore. Distant stations at Arequipa (AREQ), Bogota (BOGT), Galapagos (GALA), Kourou (KOUR), Fortaleza (FORT) and Santiago (SANT), coastal stations at Molina (MOLI), Salinas (SALI) and Pucusana (PUCU) and GPSA deep (DEEP) and shallow (SHAL) seafloor arrays are shown in Figure II.2. Figure II.3 shows the east, north and up

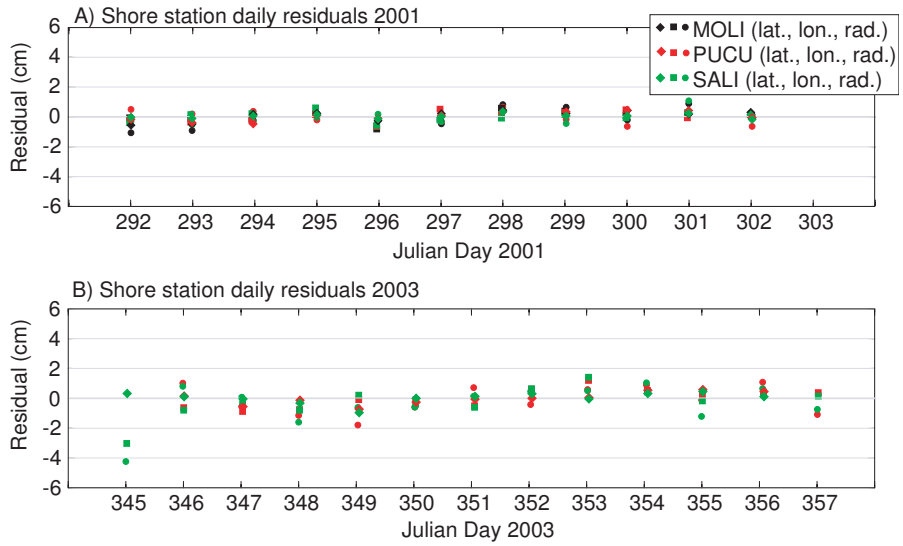

Figure II.3: Daily east, north and up residuals for coastal GPS stations MOLI, PUCU and SALI in 2001 (A) and PUCU and SALI in 2003 (B) using fixed distant stations on stable South America.

Table II.2: GPS station vectors (mm/yr) 2001 to 2003 in trench perpendicular and parallel components.

Station	Lat. (°S)	Lon. (°W)	V_{dip}	V_{str}	Vector	Az
PUCU	12-27.96	76-45.54	26±6	26±4	37	105
SALI	11-14.28	77-36.72	31±6	19±4	37	92

daily residuals for SALI, PUCU and MOLI in 2001 and SALI and PUCU in 2003. The residuals vary less than ±10 mm. Station rates relative to stable interior of South America are shown in Table II.2 and were within millimeters of the ITRF00 solution. These rates show large relative displacement of the west coast of South America as a result of the convergent boundary. The positions of the coastal stations were averaged over the time span of GPSA operations and held fixed in the kinematic solution for shipboard GPS antennas.

II.1.B Kinematic GPS

Three GPS antennas were mounted on 12.2 meter towers on the R/V Roger Revelle and wired to TurboRogue receivers. A rigid foundation is required for each GPS antenna and the hydrophone such that the antenna-hydrophone baselines do not change during several days of data collection at sea. The height and spacing of the antennas expose a tradeoff between multipath and rigidity of the antenna supports. The towers were designed to provide roll and pitch stability to 2-3 mm (Chadwell, 2003).

The GPS carrier wave is right hand circularly polarized (RHCP) such that rotating a GPS antenna will include a bias due to phase wrapping. Antenna rotation causes the same bias as GPS receiver clock offset and is therefore indistinguishable from a clock error since it is common to all phase measurements. The effect is also cumulative in that rotating past 360° continues to increase the phase error. One revolution causes an offset in the L1 and L2 frequencies of 19 and 24.5 cm, respectively (Leick, 2004). Phase wrap in the kinematic GPS solution was accounted for by tracking the absolute position of the three shipboard antennas. In these surveys, ship heading was controlled by dynamic positioning though sea conditions sometimes necessitated a heading change. None of the solutions included a full revolution of the GPS antennas and therefore no correction was required. All kinematic GPS analysis, including positional uncertainty and ship heading, will be presented in Section II.4.B.

II.2 GPS antenna-hydrophone baseline

Daily total station surveys provided the baseline between GPS antennas and well-mounted hydrophone. Daily surveys average fluctuations in height of the well-mounted hydrophone or antenna position. The surveys were performed with a standard surveyors instrument mounted on the deck directly above the 1-m diameter access well, housing the hydrophone, and in view of each antenna (Figure

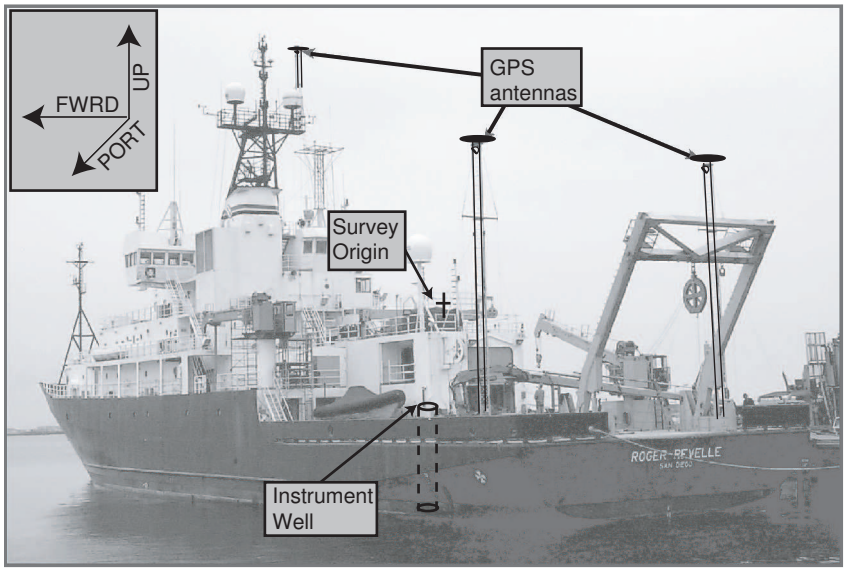

Figure II.4: Shipboard total station survey on R/V Roger Revelle. Three GPS antennas and the well mounted hydrophone were surveyed daily from the survey origin.

II.4). Three surveyors take ranges with an electromagnetic distance measurement (EDM) and angle measurements in two orthogonal planes to optical corner cube reflectors backed on the hydrophone and mounted below each antenna. The average baseline plus the offset between the antenna phase center and the reflector is used to transfer the GPS positions to the hydrophone, where they are averaged.

A histogram of RMS residuals for the survey measurement of each antenna and the hydrophone is shown in Figure II.5 for each array in 2001 and 2003. The vector residuals were smallest ($\sim$1.75 mm) for the hydrophone measurement due to a short baseline ($\sim$13 m) from the survey origin. The average residuals for the remaining baselines measurements averaged 4.7$\pm$2.3 mm.

II.3 Acoustic component

Two-way acoustic travel times are measured between the ship and each transponder. Travel times are incorporated into the GPSA least squares adjust-

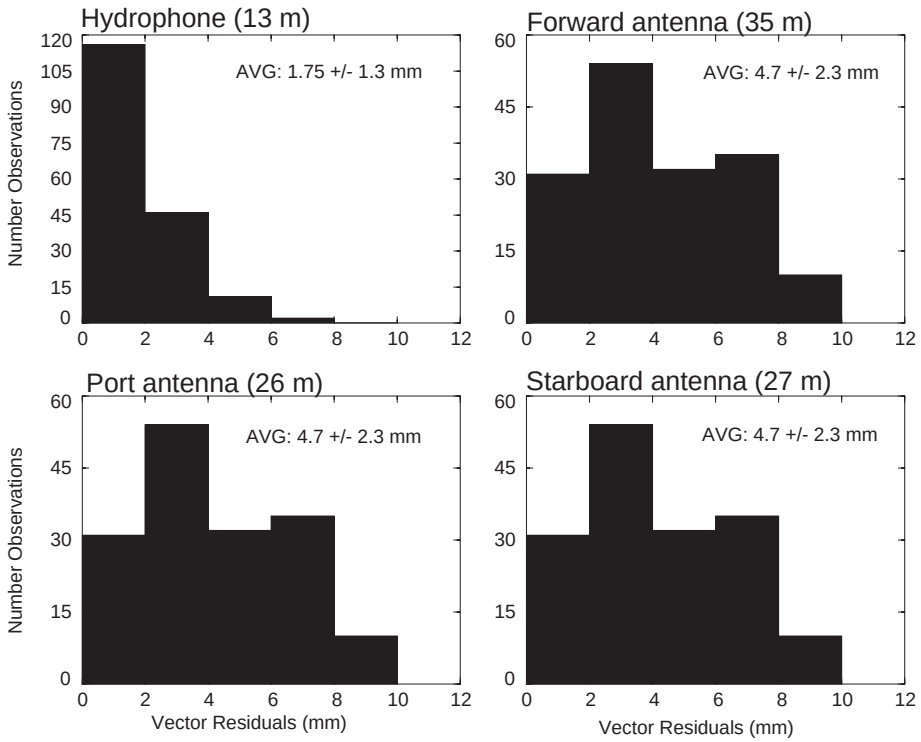

Figure II.5: Histogram of RMS residuals for total station survey measurements of each antenna and the hydrophone. Baseline length from survey origin is shown in parentheses.

ment with knowledge of the sound speed profile and sea surface height. Acoustic interrogation includes transmitting a sweep-code signal from the ship, where a stored replica is time-stamped. The transponder receives the signal and emits a delayed reply with a preprogrammed tag frequency clipped to the end. The total delay combines a set delay line and the residual delay, caused by the passive band pass filter, the power amplifier transformer and the hydrophone. The residual delay is measured before the transponder is deployed. The surface acoustic unit identifies each PXP by it's unique tag frequency. A match filtering process is used to step back the reply to the point of highest correlation with the original copy. The location of the correlogram peak can be determined within ± 5 μs, about 4 mm in range. A quality value equal to the amplitude of the correlogram, shows how well the signal was correlated. A low quality can represent a high uncertainty or

interference by noise and/or multipath. The transponders at the Peruvian margin operated at carrier frequencies between 13.5 and 17.5 kHz and the signal pulse length was 8 ms.

Sound speed changes as a function of density, which in the ocean is a function of pressure, temperature and salinity. Higher temperatures in the upper 500 meters and increasing pressures above 1500 meters create above average sound speeds. The upper layers have the largest sound speed gradient, up to 0.3 m/s/m, compared with depths over 2000 m, which have a gradient of less than 0.02 m/s/m. The variability near the surface can be caused by isopycnal tilt due to internal waves, surface waves, air entrainment and/or lateral variations in density, temperature and salinity depending on ocean currents.

The sound speed was calculated by an inversion of pressure, temperature and salinity measurements using formulas by Chen and Millero (Chen and Millero, 1977), Del Grosso (Grosso, 1974) and Wilson (Wilson, 1960). Del Grosso's inversion for sound speed was favored and is represented by,

$$C_{STP} = C_{000} + \triangle C_T + \triangle C_S + \triangle C_P + \triangle C_{STP}, \tag{II.5}$$

where, $C_{000} = 1402.392$,
$\triangle C_T = 5.011 \times T - 5.509 \times 10^{-2} T^2 + 2.21 \times 10^{-4} T^3$,
$\triangle C_S = 1.329 \times S + 1.289 \times 10^{-4} S^2$,
$\triangle C_P = 1.560 \times 10^{-1} P + 2.449 \times 10^{-5} P^2 - 8.834 \times 10^{-9} P^3$,
$\triangle C_{STP} = -1.276 \times 10^{-2} TS + 6.352 \times 10^{-3} TP + 2.655 \times 10^{-8} T^2 P^2 - 1.593 \times 10^{-6} TP^2 + 5.221 \times 10^{-10} TP^3 - 4.380 \times 10^{-7} T^3 P - 1.617 \times 10^{-9} S^2 P^2 + 9.684 \times 10^{-5} T^2 S + 4.856 \times 10^{-6} TS^2 P - 3.406 \times 10^{-4} TSP$,
and T is the temperature in degrees Celsius, S is the salinity in parts per thousand and P is the pressure in kilograms per square centimeter (Grosso, 1974). The sound speed parameters were measured by casting a conductivity-temperature-depth (CTD) sensor from the sea surface to within 10 meters of the seafloor throughout GPSA operations. The number of casts, depth coverage and duration of CTD measurements for each realization are shown in Table II.3. Roughly

30 water samples were also taken at varying depths in order to compare the measured salinity against the conductivity conversion. The CTD sensors operated at 1 Hz with a 1-σ uncertainty of ± 0.0001°C, ± 0.0001S/m and ± 1dbar, respectively (Watts, 2000). Processing the raw data with Sea-Bird, filtering out erroneous salinity and temperature readings produced two sound speed profiles roughly each hour, or 2 measurements at any one depth per hour. Higher frequency variations in the sound speed were not measured with the CTD though they can be observed in the acoustic range residuals. In addition, un-modeled sound speed variations do not significantly affect the estimate of transponder location after several days of GPSA data collection, see Section II.4.B.

The average sound speed, temperature and salinity profiles were computed for each epoch as well as one all-epoch average. Figure II.3, column 1, shows the all-epoch average sound speed (black, bold line) compared to the individual epoch (2001 and 2003) averages. Seasonal changes in water masses affect the slope of each profile near the surface though the sound speed gradient is consistently the largest in the top 200 meters. The second column in Figure II.3 shows the average sound speed RMS values. Sound speed in the upper water column varies up to ± 1 m/s. The residuals converge for each array to roughly ± 0.1 m/s at depths greater than 2 km, verifying the stability of the deep ocean at these arrays. The variability of the all-epoch average is similar to that of each individual epoch, which demonstrates both the capability and limitations of this frequency of measurement. The deep ocean sound speed can be accurately mapped with few profiles in this region. Sound speed variability can also be investigated by calculating the harmonic mean. Figure II.30 shows the harmonic mean sound speed for increasing water column depths as a function of time with roughly 2 casts per hour. In the top 10 m, the harmonic mean sound speed can change by 10 m/s on the order of an hour. At depths greater than 100 m, the harmonic mean changes less than ± 1 m/s by pressure changes at the surface. At this time, maintaining the ship at the acoustic center on the order of 4-5 days is necessary in order to cancel these higher

frequency variations and maintain a positional uncertainty on the order of mm.

The sound speed is highly dependent on temperature. The all-epoch and individual epoch average temperatures are shown in the third column of Figure II.3. The surface temperature is representative of seasonal changes in water masses. Approaching the summer months in Peru, December to March, the thermocline strengthens with the southward extension of warm surface waters. The RMS values show $\pm 0.1^{\circ}$ C at the surface and $\pm 0.01^{\circ}$ C beyond 1000 m depth. Salinity, shown in the fourth column, also affects the sound speed, though to a lesser degree than temperature. The variability averaged $\pm$ 0.1 psu at the surface and ± 0.01 psu at depth.

Sea surface height is needed to shift the ray path to the height of the geoid in the acoustic ray trace calculation. A record of sea surface height was created with both tide gauges and tide models to cover the time span of GPS-acoustic operations. The geoidal undulation, from the University NAVSTAR Consortium (UNAVCO), as well as the solid earth tide were also included in the correction.

The tide gauge is a Paroscientific Digiquartz pressure gauge housed in a metal casing, attached to weights and allowed to free-fall from the ship. Four tide models were also calculated and could be used when pressure gauge data were not available. The tide model is also used to subtract the mean depth from the tide gauge record and isolate the tidal variation at the surface. The tide models include fes952 (Provost et al., 1994), csr3tr (Eanes and Bettadpur, 1995), schw (Schwiderski, 1980) and tpxo2 or TOPEX/Poseidon satellite radar altimetry (Egbert et al., 1994).

Converting pressure to depth in the ocean requires additional measurements of compressibility as well as the effect of the local gravity field. Atmospheric pressure was measured every 30 seconds from the ship and subtracted from the pressure record to account for the inverse barometer effect. The geopotential anomaly was estimated based on latitude and combined with the pressure

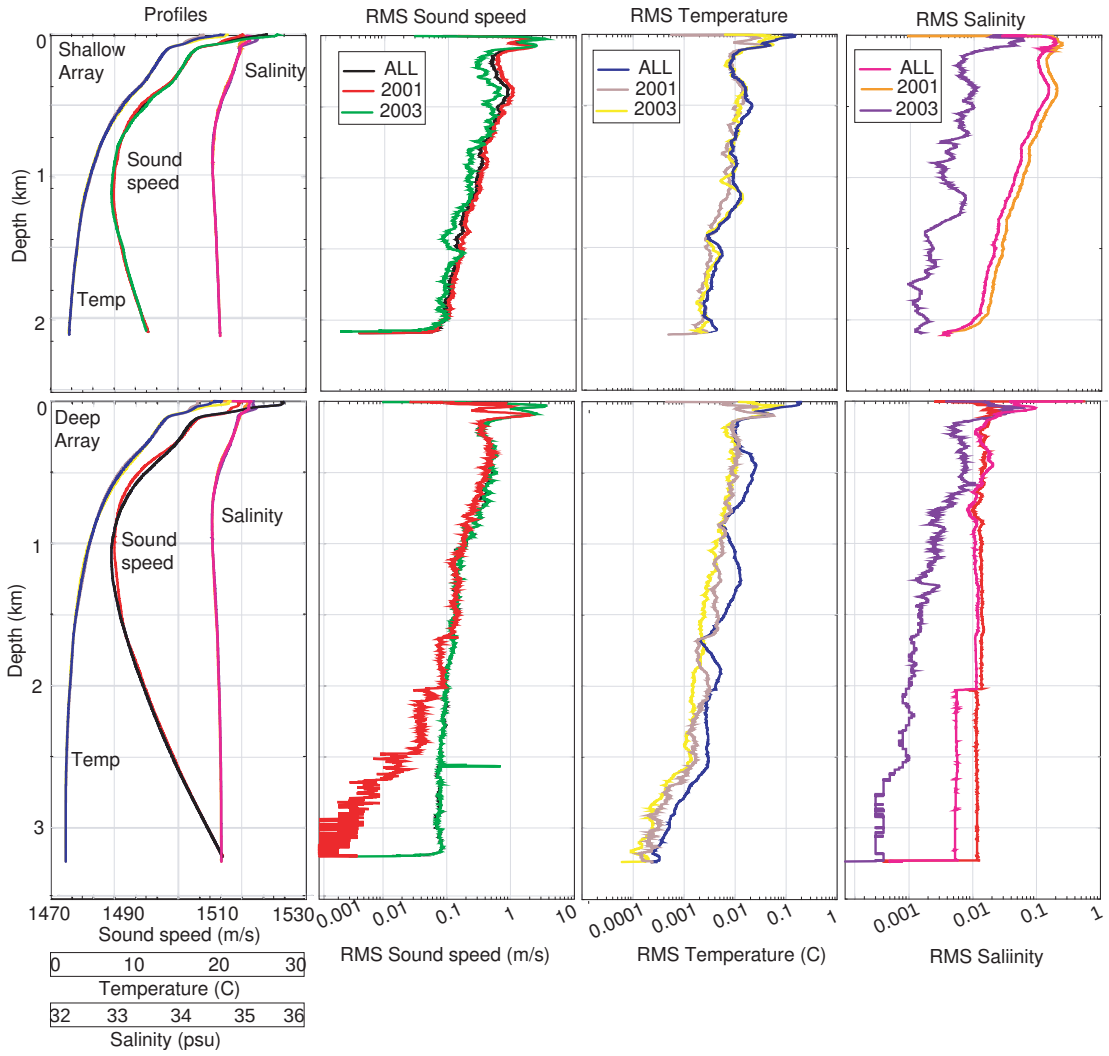

Figure II.6: a) Sound speed, temperature and salinity profiles at shallow (top row) and deep (bottom row) arrays in 2001 and 2003 using CTD measurements and Del Grosso calculation. See Table II.3 for the number of CTD casts per site per year. b) Average sound speed RMS at each array. Bold, black line represents the average profile using data from all epochs. c) Average temperature RMS at each array. Bold, blue line represents the average profile using data from all epochs. d) Average salinity RMS at each array. Bold, magenta line represents the average profile using data from all epochs.

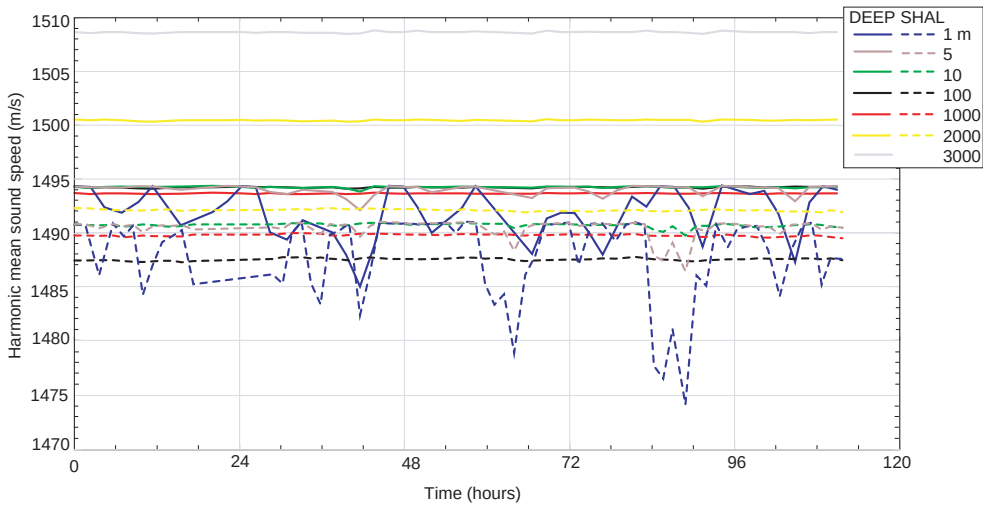

Figure II.7: a) Harmonic mean sound speed from the surface to increasing depths (1-3000 m) for deep and shallow arrays in 2003. Each point represents a CTD cast.

Table II.3: CTD casts at each array and epoch

Array	Epoch	Casts	Depth(m)	Month	Time (hrs)
Deep	2001	82	4 - 3200	OCT	120
Deep	2003	52	4 - 3200	DEC	91
Shallow	2001	80	4 - 2200	OCT	114
Shallow	2003	76	4 - 2200	DEC	113

record as well as a saltwater correction (Saunders and Fofonoff, 1976).

GPS data collection also provided an ellipsoid-based height measurement of the ship at 1 Hz. The amplitude of the tide can be isolated by subtracting the orthometric height, N, or the average difference between the tide model and ship's GPS observed height above the ellipsoid, $N = h - H$, where h is the height above the ellipsoid and H is the tidal height, or the height above mean sea level, approximated by the geoid, Figure II.8. The amplitude and period of the tidal record and GPS ellipsoid height record can be compared, though the magnitudes differ by up to 30 m, since the ellipsoid-coordinate system, used as a geodetic horizontal and vertical datum, only approximates and is often different from the mean sea level.

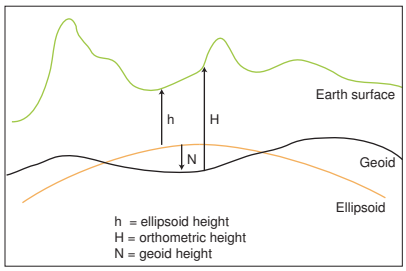

Figure II.8: Relationship between height of the geoid, ellipsoid and earth surface. GPS height is referenced to the ellipsoid.

II.4 GPS-acoustic surveys

GPS and acoustic data are combined in a least-squares solution and reiterated until the acoustic range residuals are below a threshold. First, the GPSA moving survey, or 1-nm radius circle drive, is used to determine the baselines between each transponder pair. Next, the GPSA array center survey provides several days of stationary GPS and acoustic data at the equal angle point. This section includes the results of both surveys at the GPSA arrays in 2001 and 2003.

II.4.A Moving survey

Moving GPSA surveys, or circle drives, are used to estimate the initial absolute position of each transponder. One nautical mile radius circles were driven around each transponder in each epoch, interrogating every 20 seconds. This provides a horizontal position of the transponder with a repeatability of ±200 mm. The depth of the transponder is poorly constrained by this method due to variable sound speeds in the upper water column and poor observation geometry. The relative transponder positions determined from the moving survey are held fixed in the GPSA center solution for all subsequent epochs. The array forms a polygon whose baselines are assumed to be rigid. A change in array geometry will appear to be a change in the horizontal position of the array. To ensure fixed internal array geometry, moving surveys and acoustic/optical surveys (Section V.2)

are performed after each GPSA survey.

Figures II.9 - II.19 show GPS and acoustic information from each moving survey as a function of time. The first plot (a) shows the GPS east, north and up uncertainty for one representative shipboard antenna (Port). The northward component has the largest uncertainty due to the geometry of the reference stations. The second plot (b) shows GPS-determined antenna baselines compared to the daily shipboard survey. The moving survey around transponder D13 in 2001 (Figure II.12) showed a large antenna baseline difference for the first 20 minutes, possibly due to the low number of satellites. The average antenna baseline difference is consistently negative during each circle drive, showing a systematic bias in the antenna baselines of 0.01 m. This bias will be discussed further in the following section. The third plot (c) shows the satellite observations for each antenna. A minimum of 4 satellites are needed to calculate position. High GPS positional uncertainty is often associated with too few satellite observations, as shown for the first half of the moving survey around PXP D20 in 2003 (Figure II.18). The fourth plot (d) shows sea surface height from the tide model and GPS. A constant is subtracted to compare the GPS height, referenced to the ellipsoid, to the geoid as discussed in Section II.3. Plot (e) shows distance from the ship to the transponder. The ship should maintain a constant distance from the transponder though variations occurred due to sea conditions. The ship is typically held within $\pm$100 m of the survey circle though at at transponder E11 in 2003 (Figure II.19) the ray path changed by 800 m. Finally, the bottom plot (f) shows the acoustic range residuals from the GPSA least-squares solution. There is no significant difference between the fixed or freed GPS solutions.

FIGURES II.9 - II.19

GPS and acoustic diagnostics for GPS-acoustic moving surveys, or circle drives, around individual transponders. a) GPS 1-σ east, north and up uncertainty for port antenna. b) GPS antenna baseline length comparison between GPS derived antenna baselines and daily total station antenna surveys. Port-starboard antenna baseline is ∼13.2m, (black), forward-port, ∼38 m, (red) and forward-starboard antenna baseline, ∼39m, (green). c) Number of GPS satellite observations versus time at each receiver. d) Sea surface height record from shipboard GPS, normalized to mean sea level (black) and fes95.2 tide model (red). e) Ship position referenced to the transponder. f) Acoustic range residuals from GPSA least-squares solution using fixed (black) and freed (red) GPS data. Fixed solution represents a fixed integer of signal wavelength ambiguities and is used in the final solution.

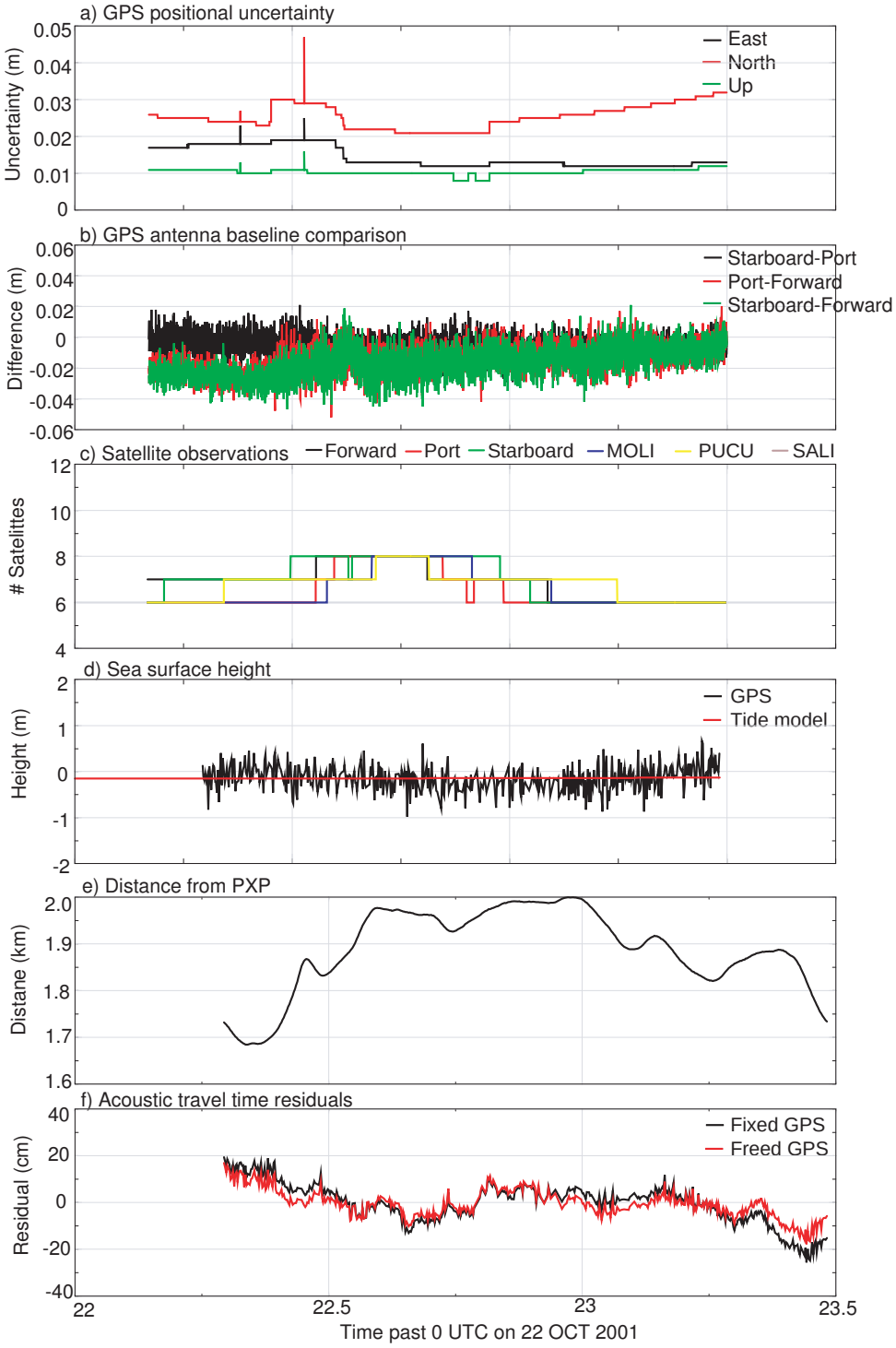

Figure II.9: Moving survey around transponder D14, 2001.

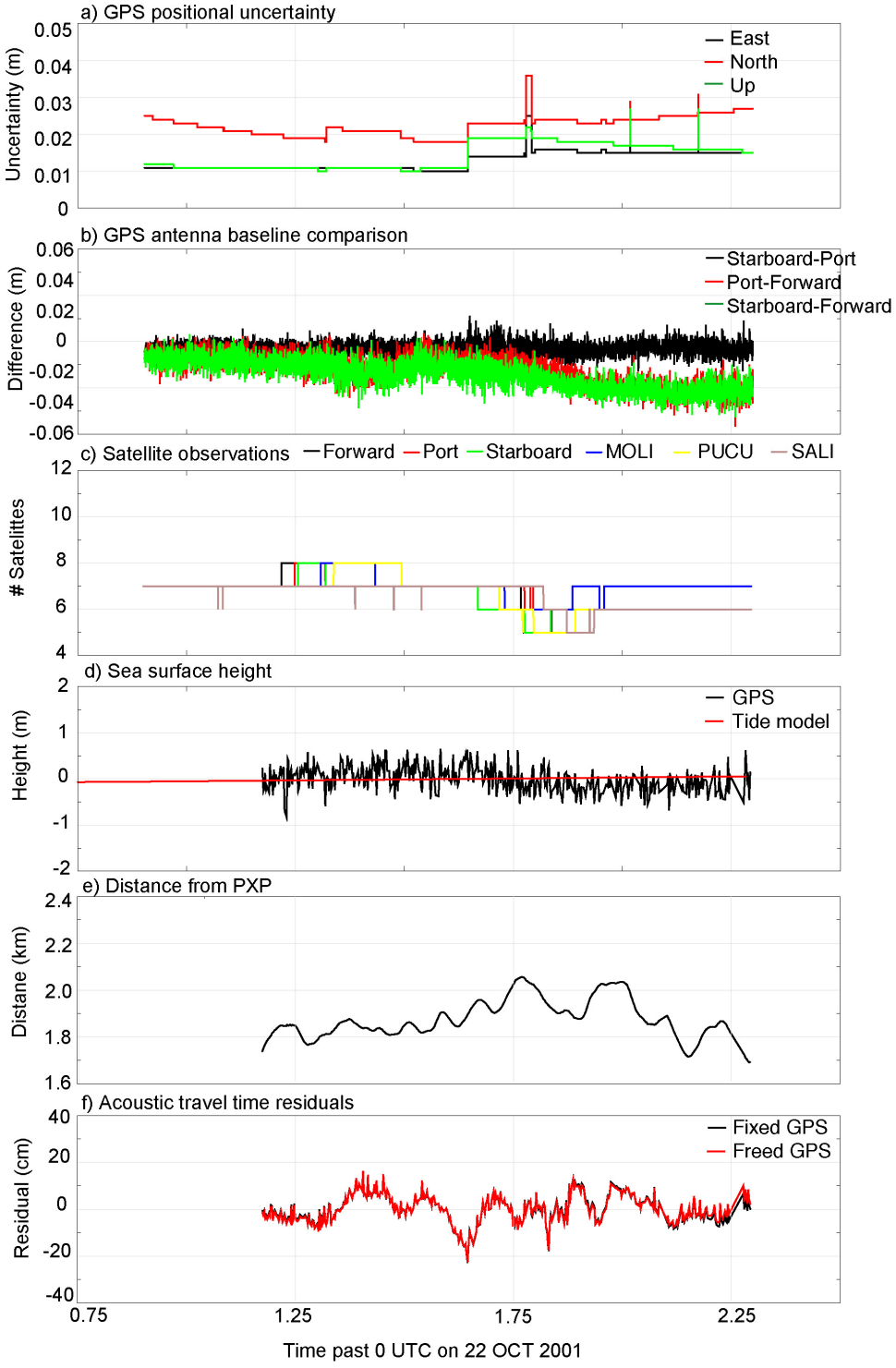

Figure II.10: Moving survey around transponder D16, 2001.

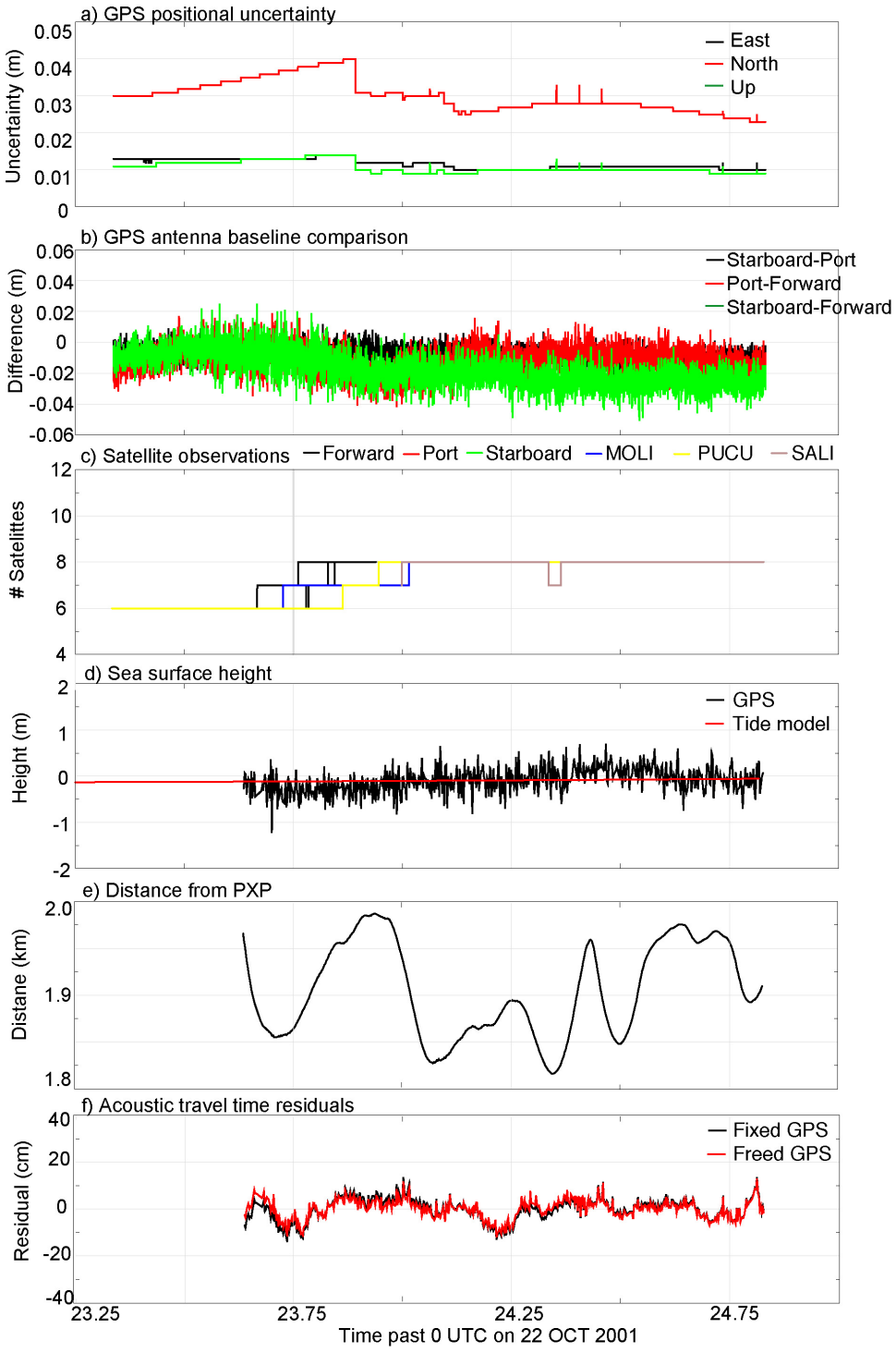

Figure II.11: Moving survey around transponder D18, 2001.

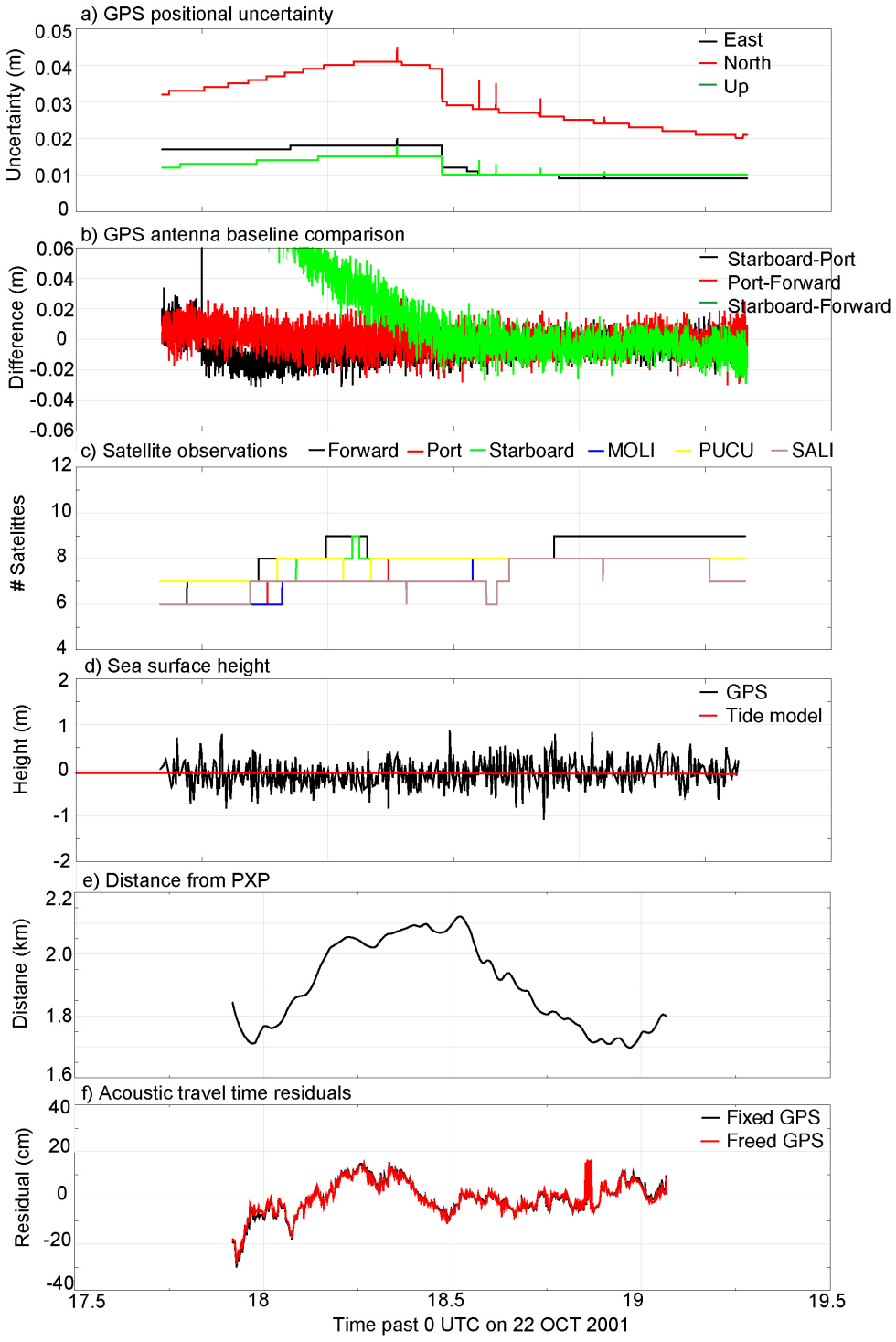

Figure II.12: Moving survey around transponder D13, 2001.

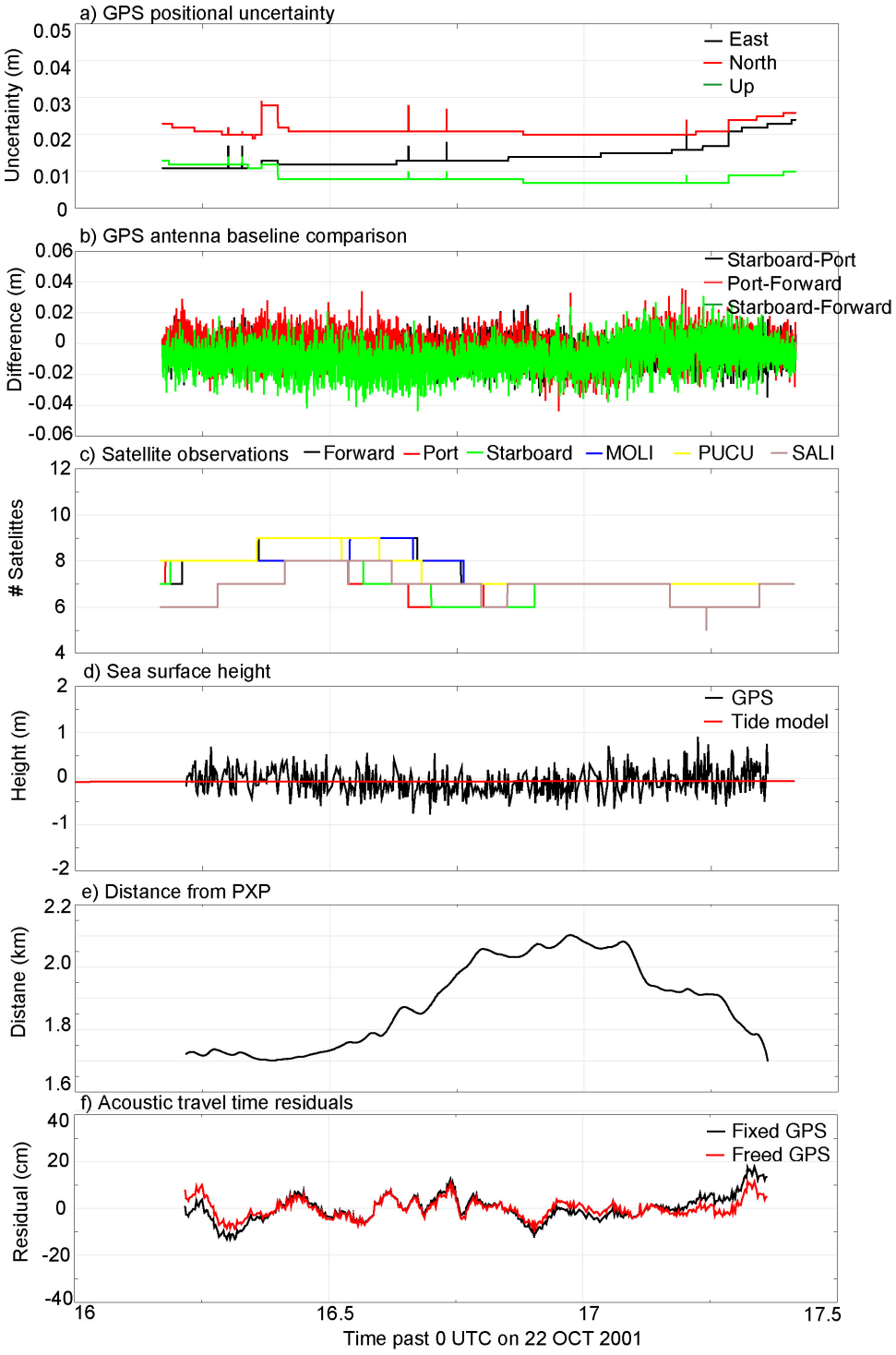

Figure II.13: Moving survey around transponder D20, 2001.

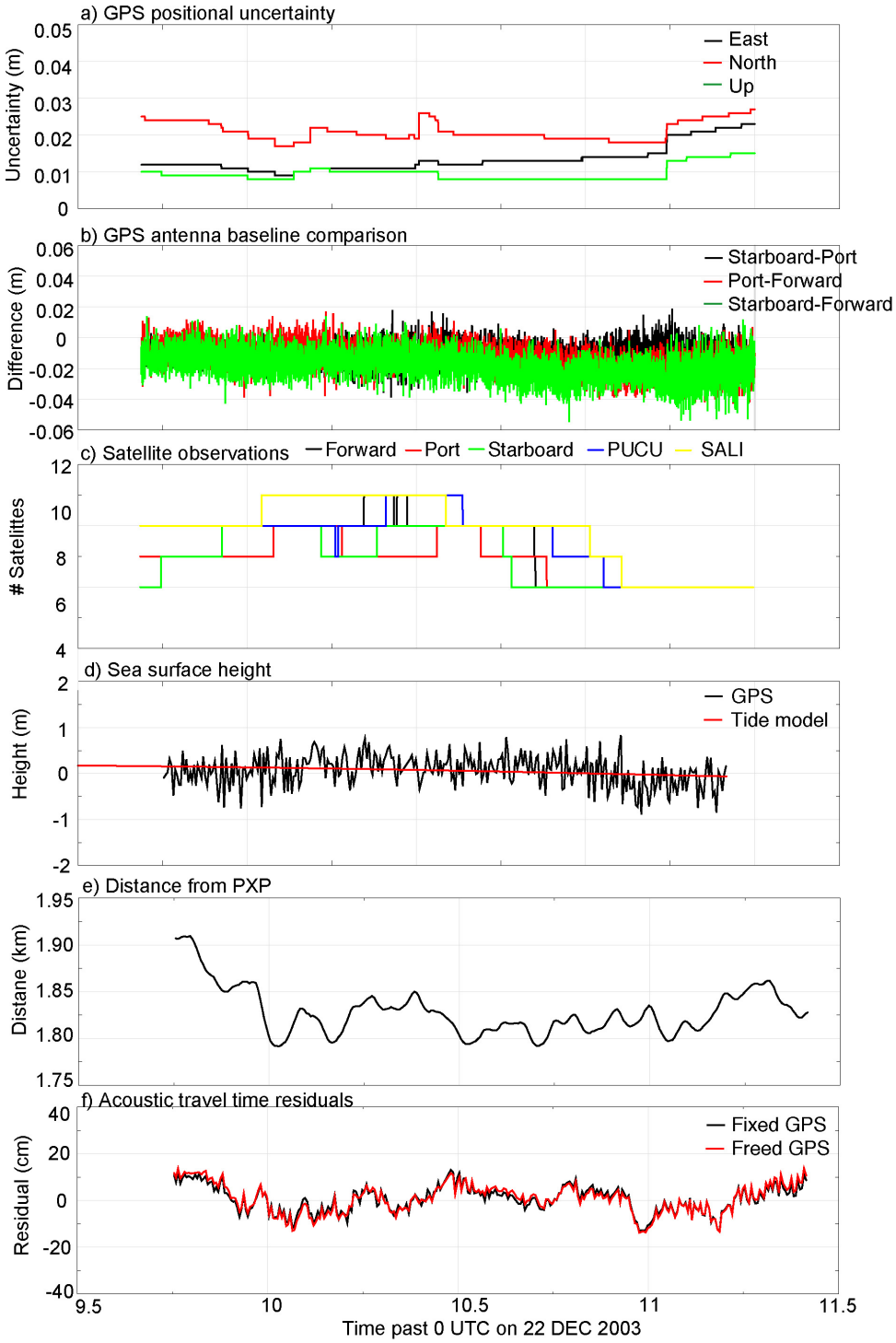

Figure II.14: Moving survey around transponder D14, 2003.

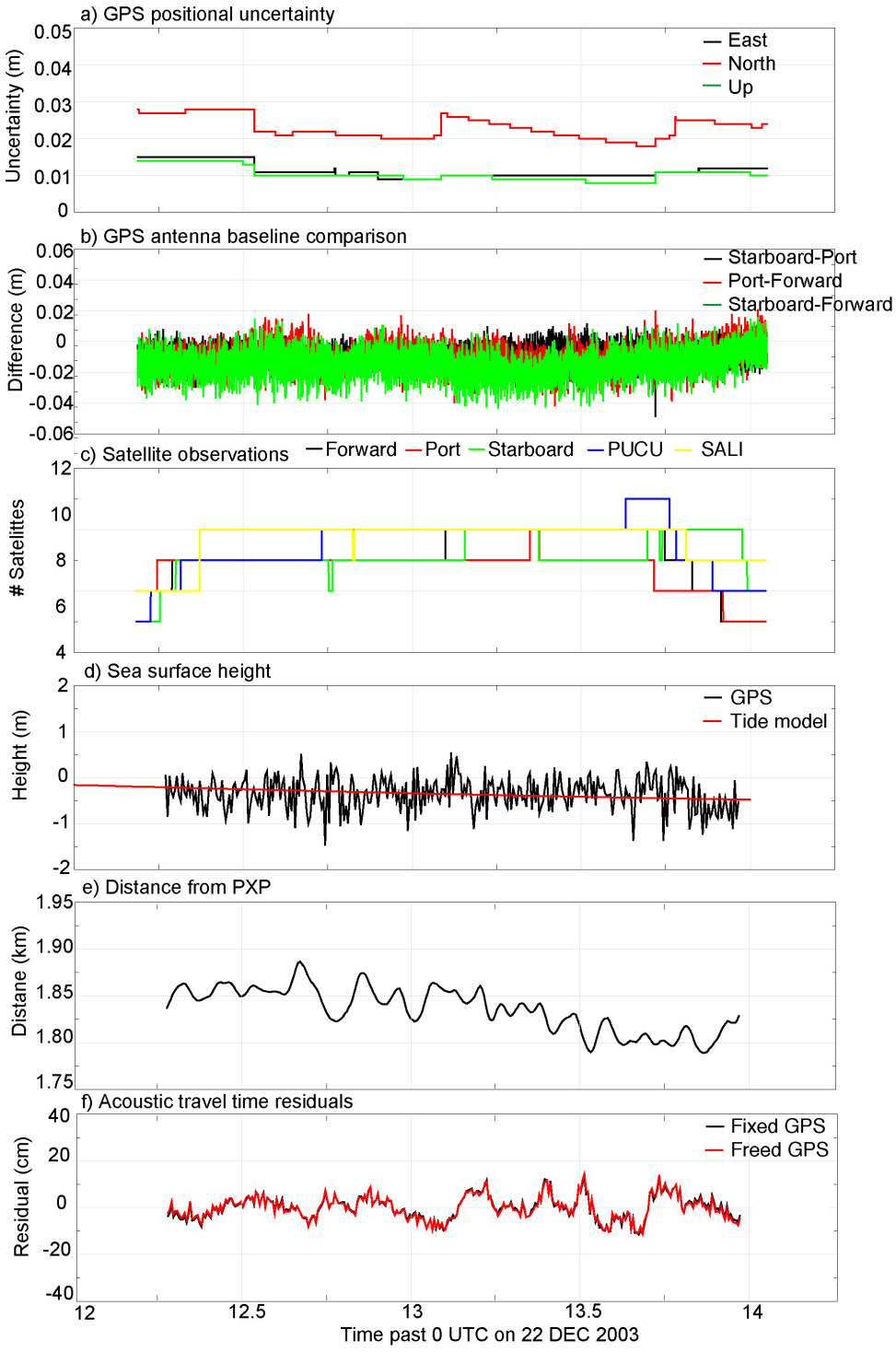

Figure II.15: Moving survey around transponder D16, 2003.

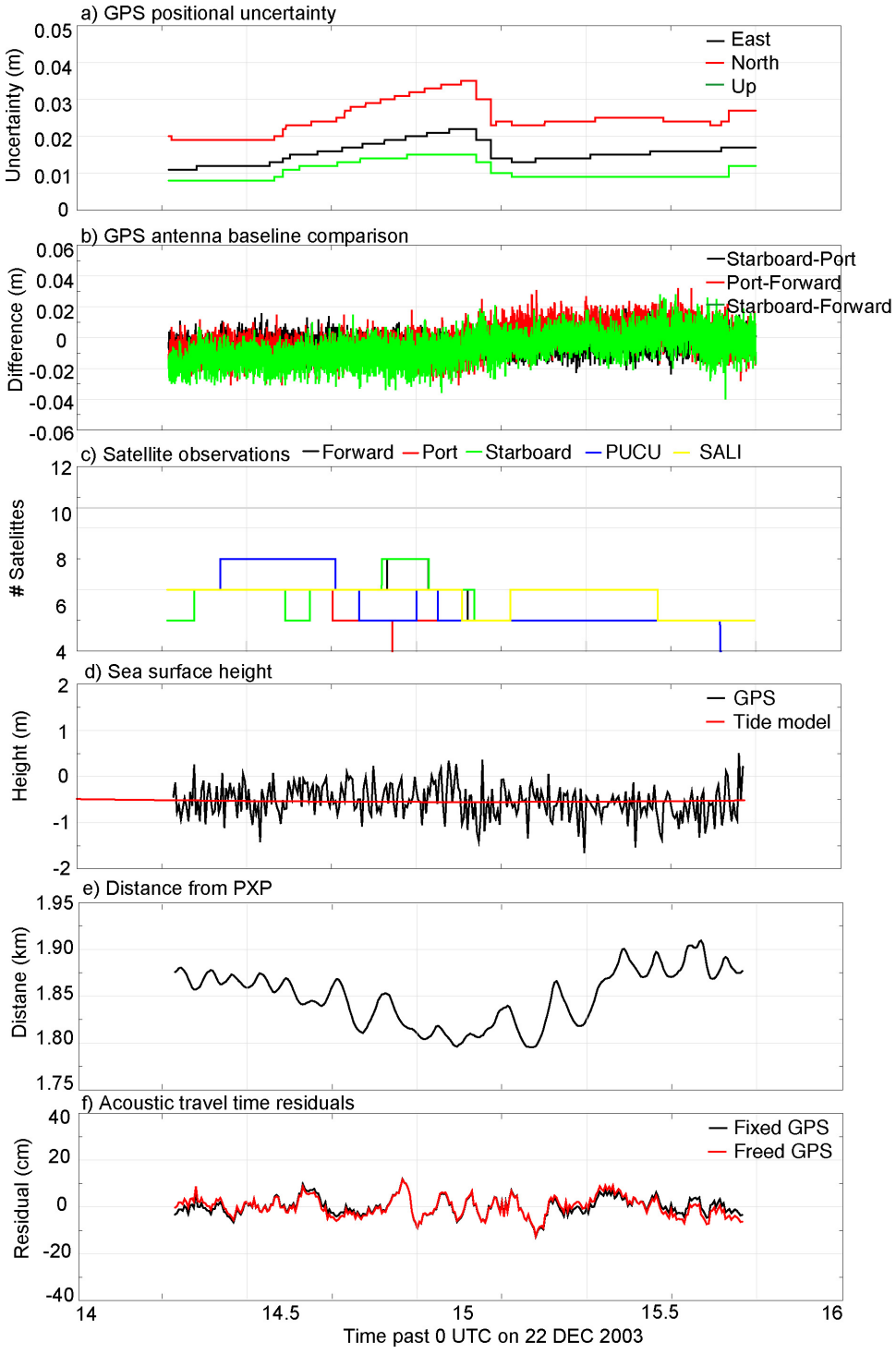

Figure II.16: Moving survey around transponder D18, 2003.

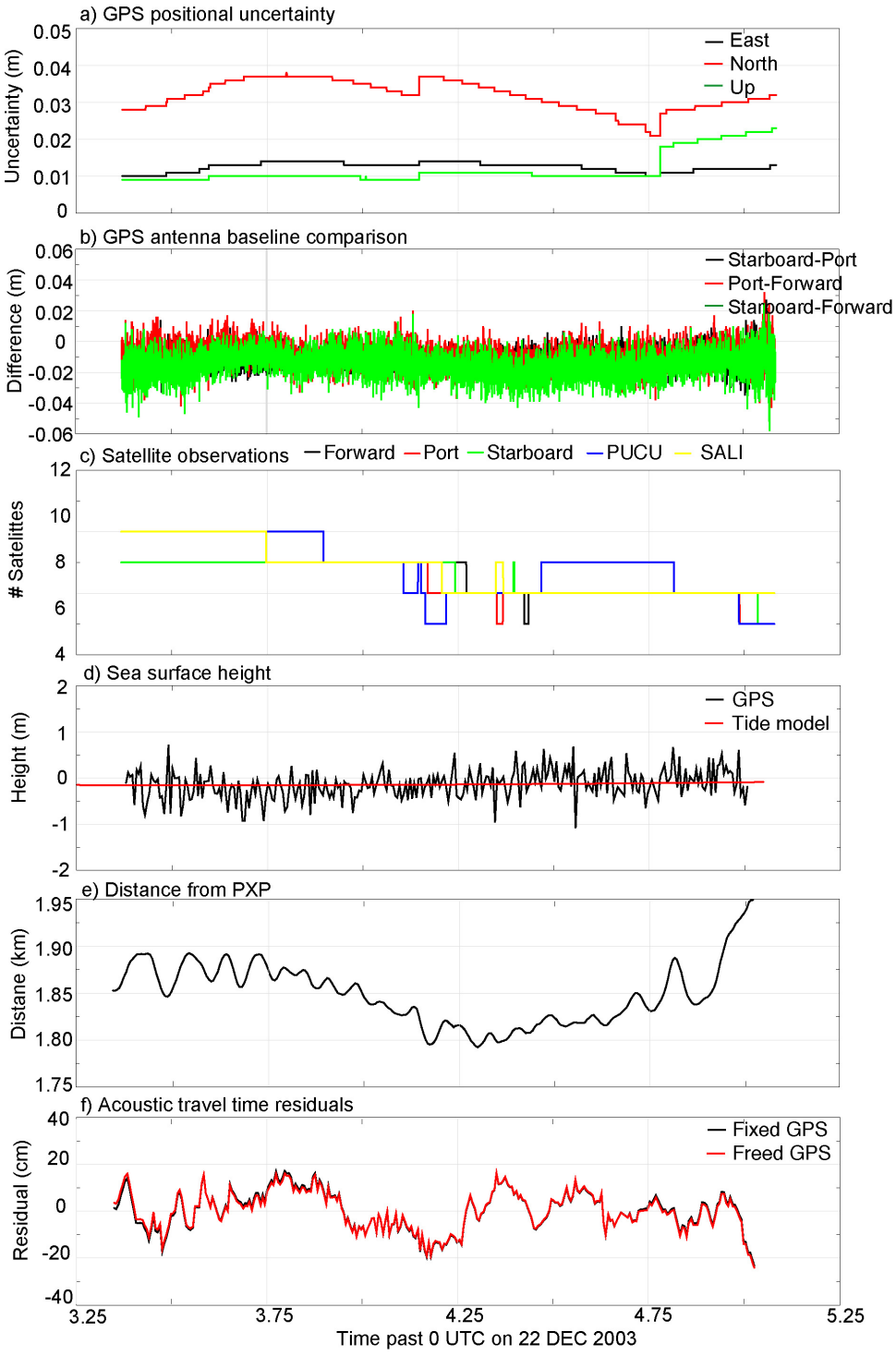

Figure II.17: Moving survey around transponder D13, 2003.

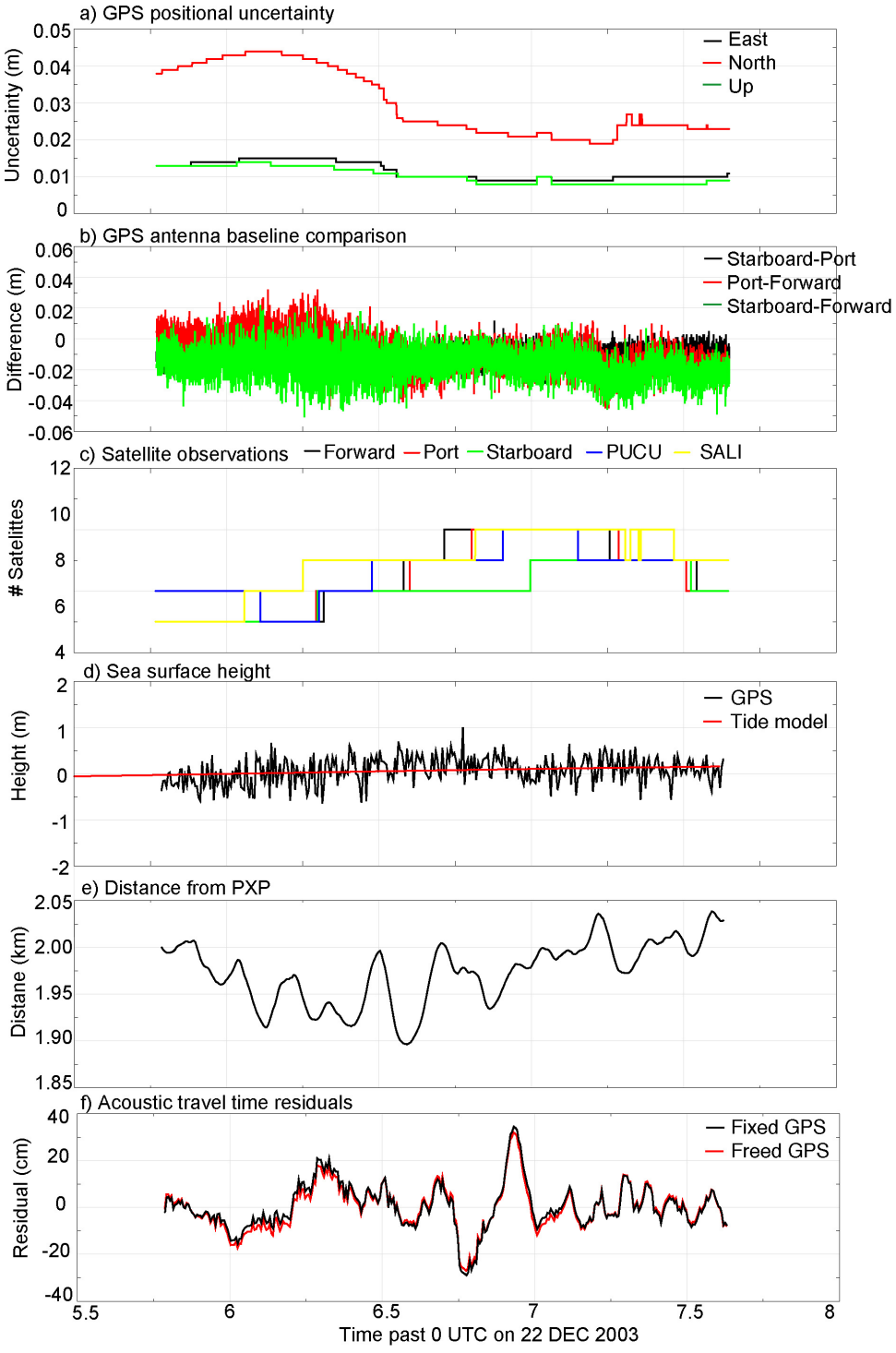

Figure II.18: Moving survey around transponder D20, 2003.

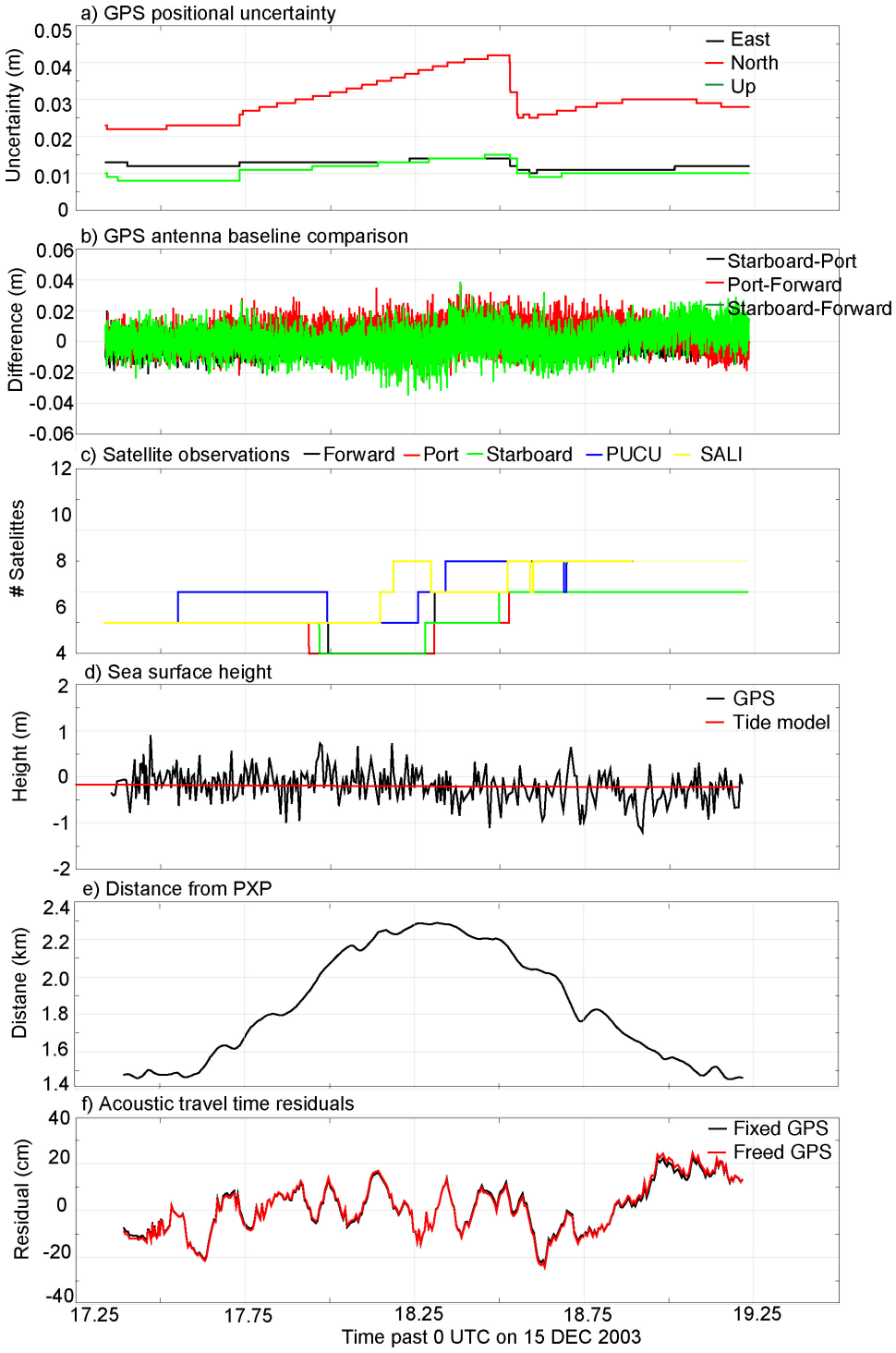

Figure II.19: Moving survey around transponder E11, 2003.

Table II.4 shows transponder positions from the moving surveys in 2001 and 2003. The 2003 circle drive positions were used as a priori positions in the array center solution. Individual transponder displacements were calculated (Table II.5) though the positional uncertainty was assumed to be too large to accurately predict plate motion. Averaging individual transponder displacements at each array, the initial predictions for array motion are 4.2 cm/yr at N75E at the deep array and 6.5 cm/yr at N25E at the shallow array, shown at the array center in Figures II.20 and II.21. The deep array is lacking a circle drive estimate for the D17/E11 relocation site. Also, the antenna baseline difference is large at transponder D20 in the deep array (Figure II.18) compared to the other moving surveys. This suggests that the 2003 moving survey solution for D20 may have additional uncertainties. The individual transponder displacements match the array center solutions (discussed in the following section) to within ±10 mm, which is better than expected.

Table II.4: Results of moving GPSA surveys: transponder locations

Array	PXP	2001 moving surveys		2003 moving surveys	
		Lat °-’	Lon °-’	Lat °-’	Lon °-’
Deep	D13	-12-17.2549	-78-30.7053	-12-17.2547	-78-30.7052
Deep	D20	-12-17.2399	-78-27.6372	-12-17.2399	-78-27.6373
Deep	E11	n/a	n/a	-12-14.800	-78-29.300
Shallow	D14	-12-10.6421	-78-10.9708	-12-10.6421	-78-10.9707
Shallow	D16	-12-10.6464	-78-8.9205	-12-10.6463	-78-8.9205
Shallow	D18	-12-8.9202	-78-9.9259	-12-8.9201	-78-9.9258

II.4.B Array center survey

For several days, GPS, CTD and acoustic data are collected from near (∼10 m) the equi-angle point. This creates an equal launch and receive angle from the ship to each transponder as well as uniformly spaced ray paths through the horizontally stratified sound speed profile. This ensures that sound speed variability in the upper water column will not affect the horizontal position estimate though the array will appear to fluctuate vertically (Spiess et al., 1998).

Table II.5: Results of moving GPSA surveys: transponder displacements in cm/yr relative to stable South America in east and north and trench perpendicular and parallel components.

Array	PXP	V_e	V_n	V	Az (°)	V_{dip}	V_{str}
Deep	D13	8.0	10.1	12.9	52	11.2	6.4
Deep	D20	-3.5	-2.9	4.5	-240	-4.0	-2.1
Deep	E11	-	-	-	-	-	-
Average		3.3	2.5	4.2	53	3.6	2.1
Shallow	D14	4.2	0.1	4.2	1	3.9	-1.5
Shallow	D16	3.6	7.1	8.0	63	6.0	5.3
Shallow	D18	9.8	1.0	9.9	6	9.5	-2.8
Average		5.9	2.7	6.5	25	6.5	0.3

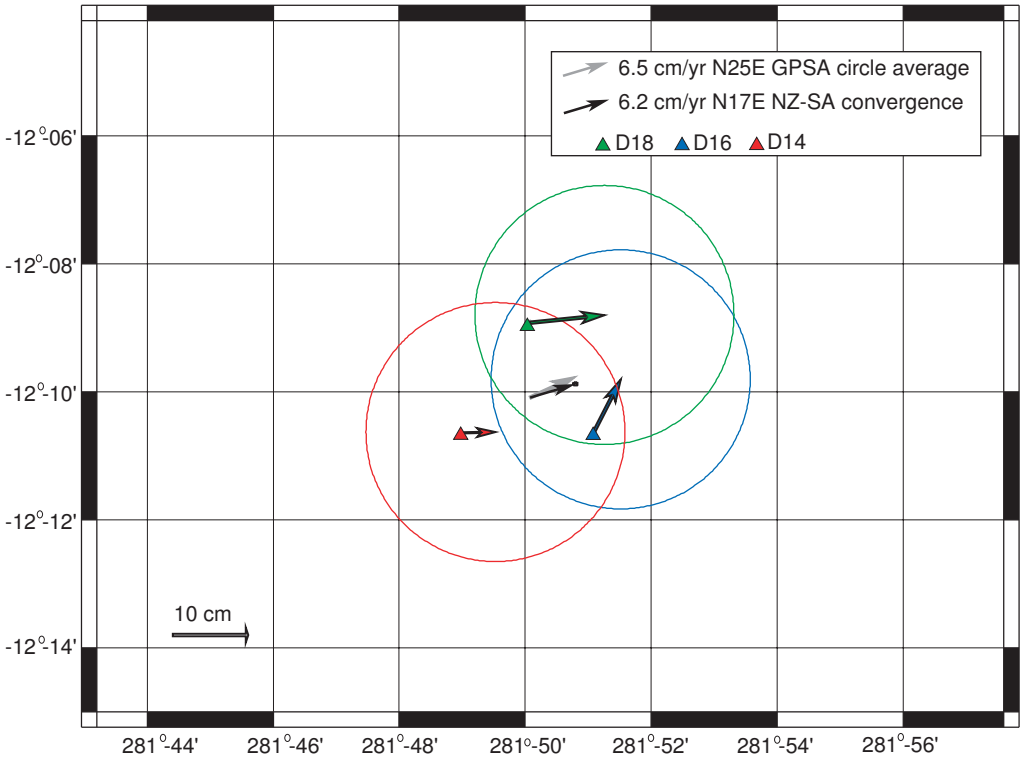

Figure II.20: Transponder displacements relative to stable South America at the shallow array. Displacement was calculated by differencing 2001 and 2003 GPS-acoustic circle drive solutions at each transponder. Average transponder displacement plotted in the center of the array (black) as well as vector of plate convergence (gray) (Altimini et al., 2002). Error ellipses are color coded and likely overestimated, at ±10 cm.

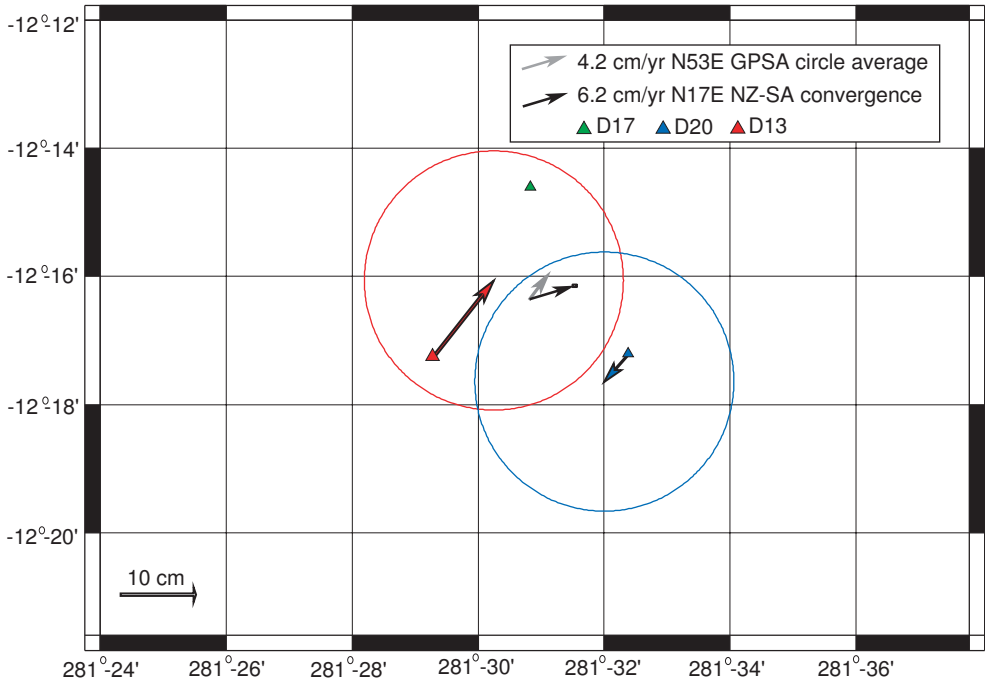

Figure II.21: Transponder displacements relative to stable South America at deep array. Symbols match those in Figure II.20.

FIGURES II.4.B-II.29

GPS and acoustic diagnostics for GPS-acoustic array solutions in 2001 and 2003. a) GPS 1-σ east (E), north (N) and up (U) uncertainty for port antenna. Legend shows average uncertainties. (100) signifies 1 in every 100 points plotted. b) GPS antenna baseline comparison between GPS derived antenna baselines and the daily total station antenna survey with respect to hours on site. Port-starboard antenna baseline is ∼13.2m, (black), forward-port antenna baseline ∼38 m (red) and forward-starboard antenna baseline ∼39m, (green). For ease in representation, a 10 point running average is plotted. c) Number of satellite observations at each shipboard and coastal receiver during GPS-acoustic data collection. d) Sea surface height record from shipboard GPS ellipsoid height, normalized to mean sea level (black), tide gauge (red) and tide model fes95.2 (green). e) Differences between tide model and tide gauge (black) and tide model and shipboard GPS ellipsoid height, normalized to mean sea level (red). f) Acoustic, two-way travel times from the ship to each transponder. f) Ship position referenced to the array's equal angle point during GPS-acoustic data collection. g) Ship heading during GPS-acoustic data collection. h) Acoustic range residuals from GPSA least-squares solution using fixed GPS data. i) Acoustic range residuals from GPSA least-squares solution using freed GPS data.

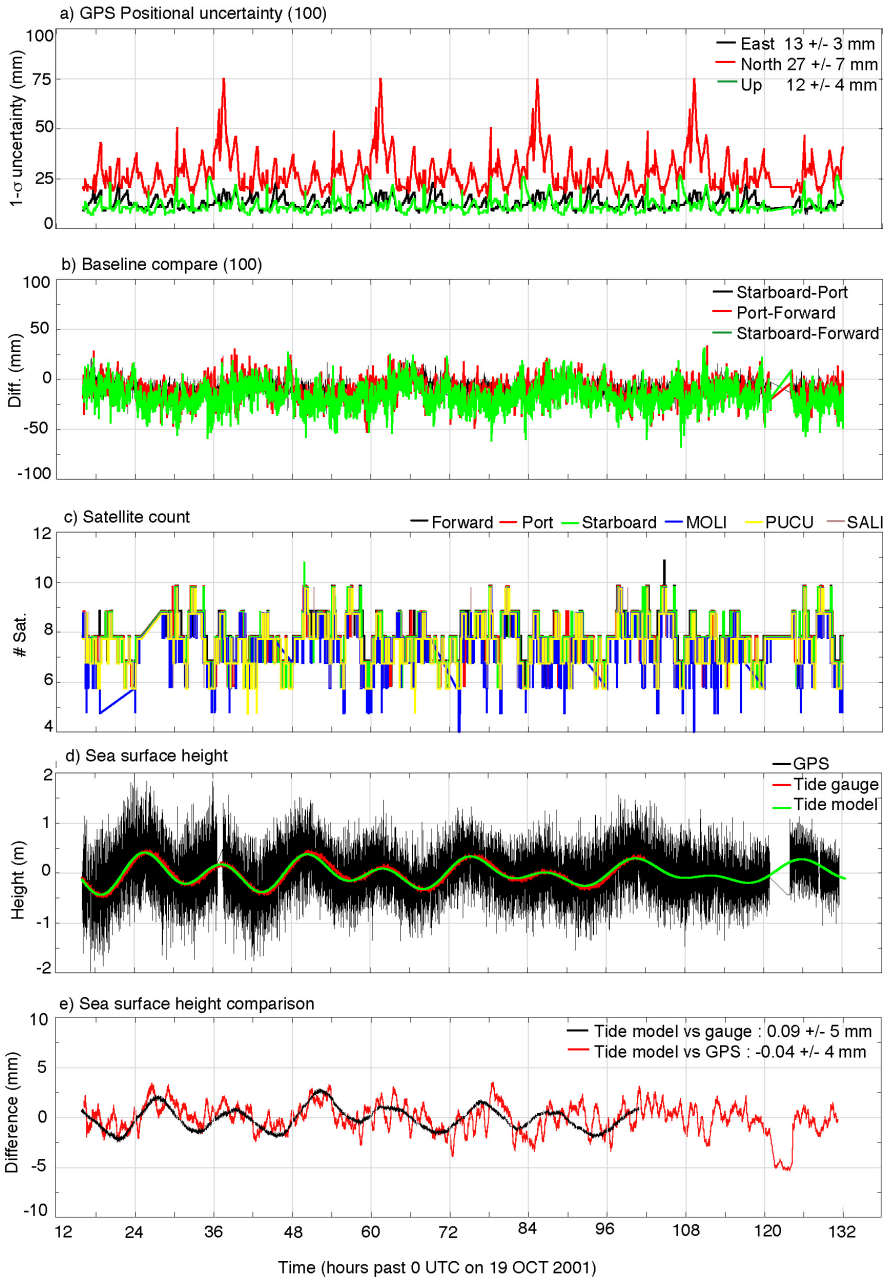

Figure II.22: Deep array, 2001, GPS diagnostics (a-e).

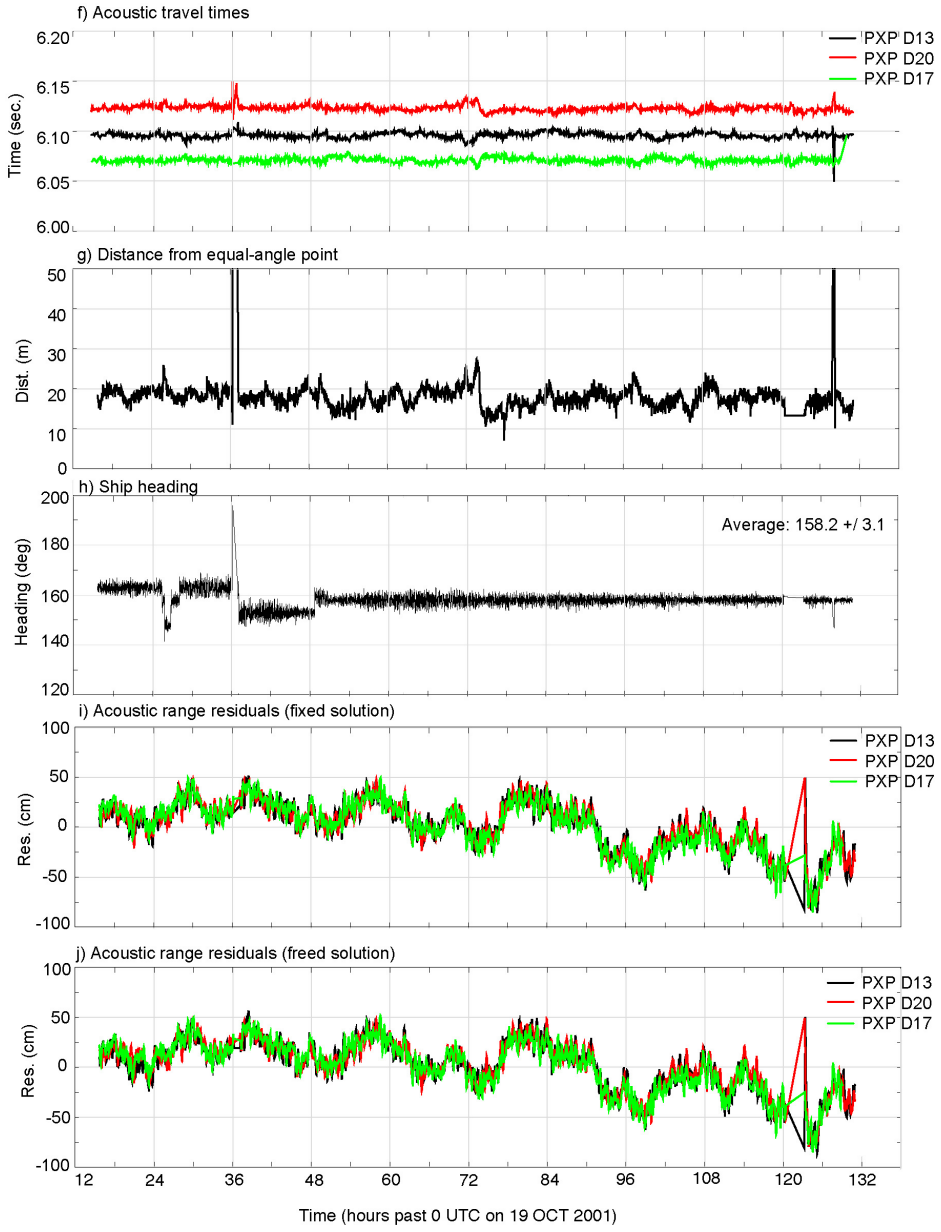

Figure II.23: Deep array, 2001, acoustic diagnostics (f-j).

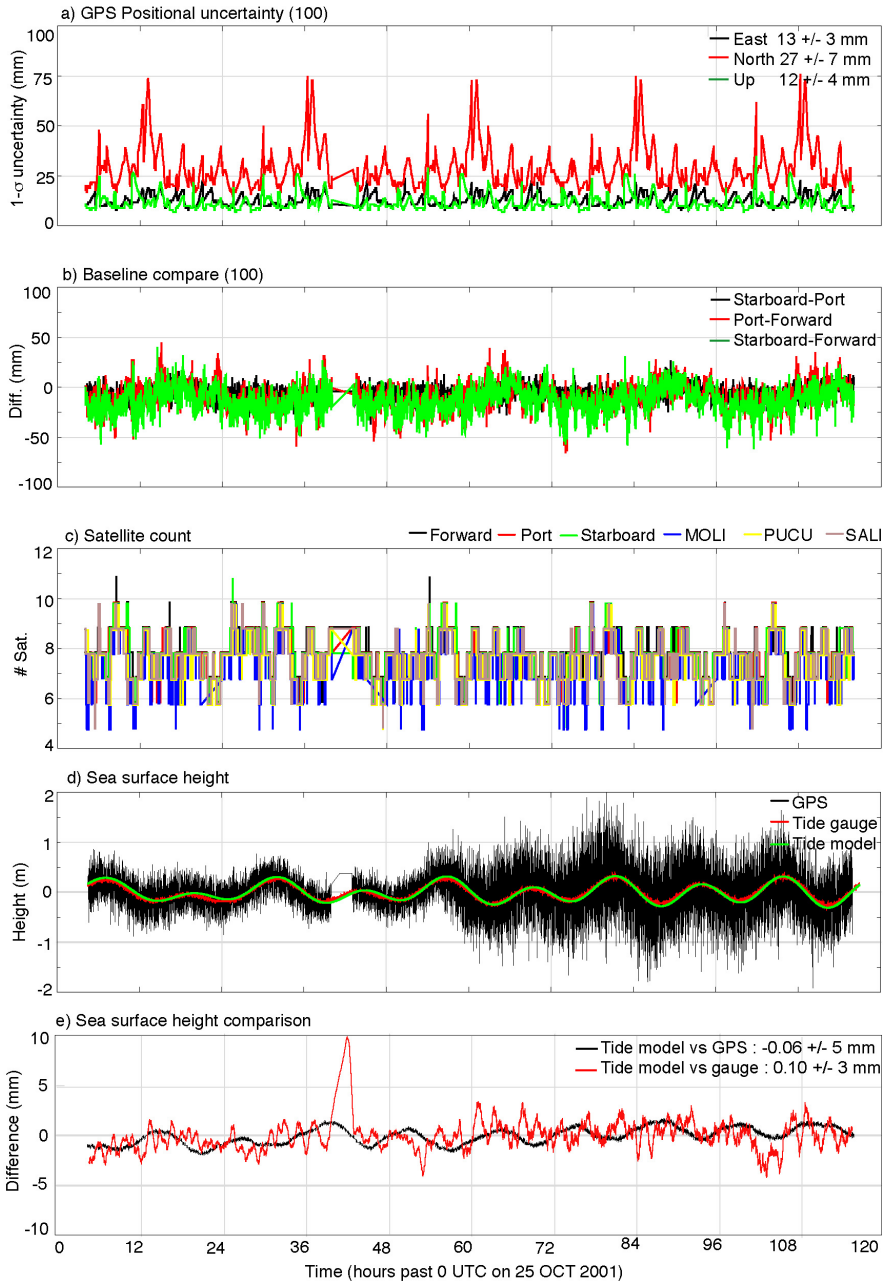

Figure II.24: Shallow array, 2001, GPS diagnostics (a-e).

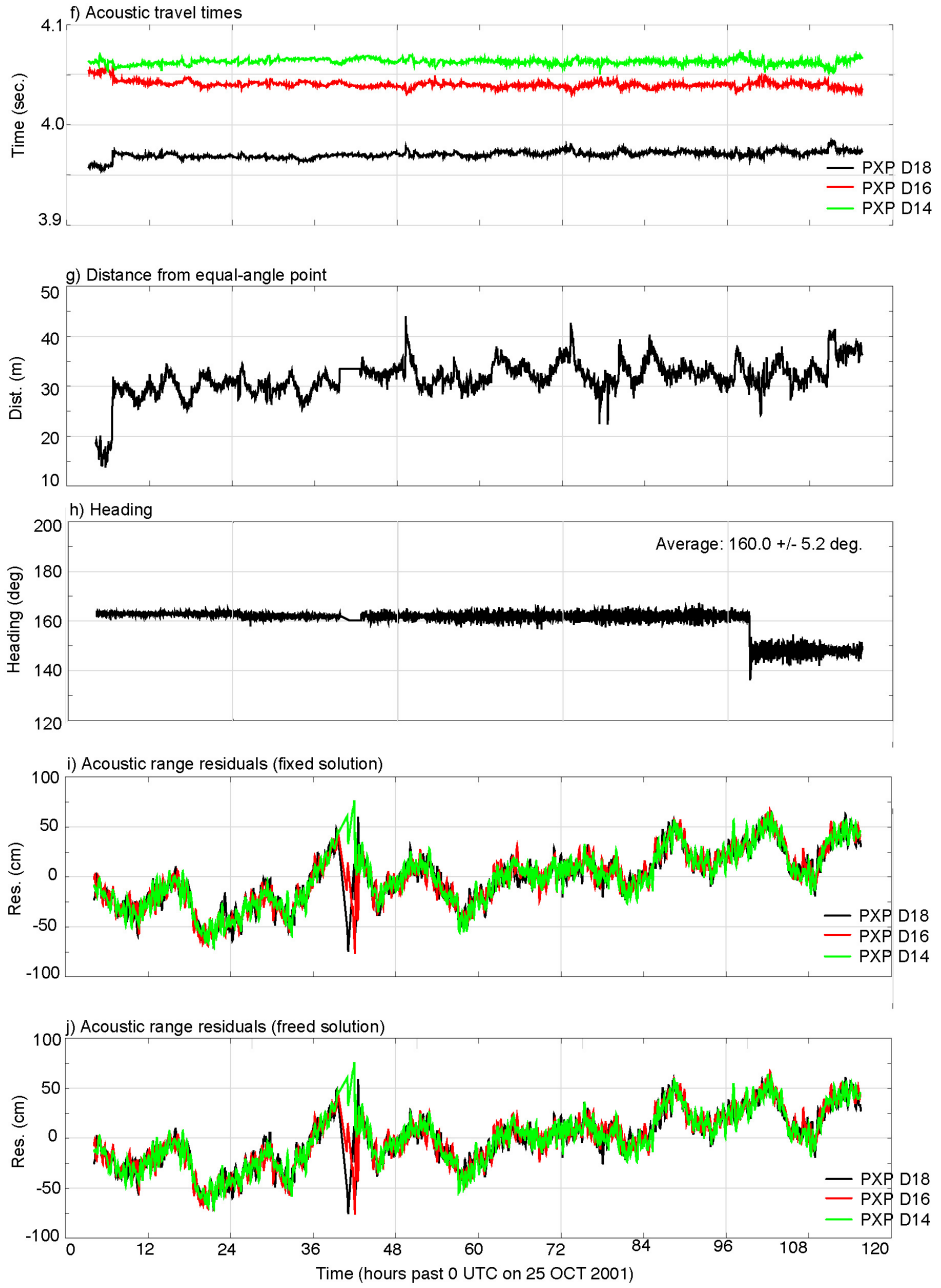

Figure II.25: Shallow array, 2001, acoustic diagnostics (f-j).

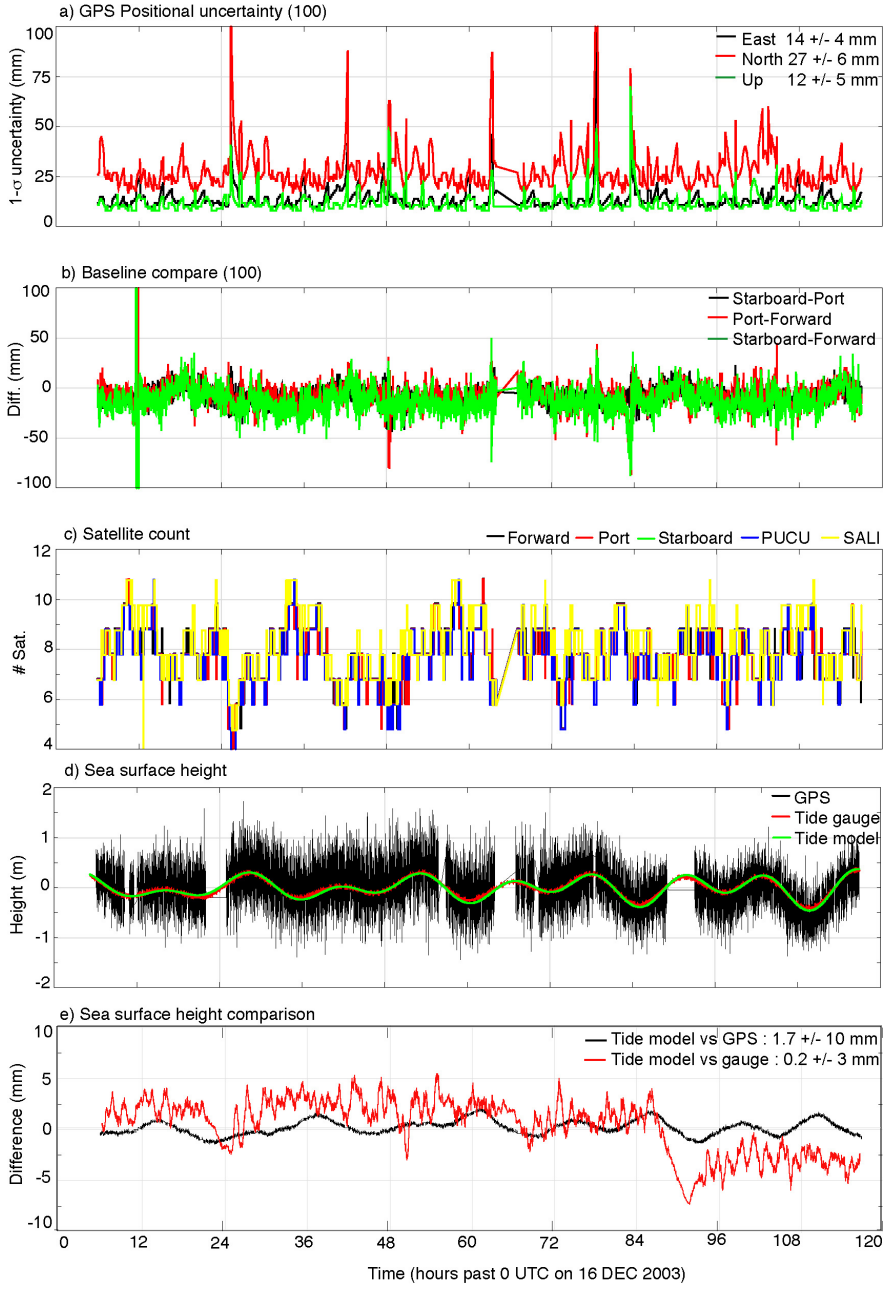

Figure II.26: Deep array, 2003, GPS diagnostics (a-e).

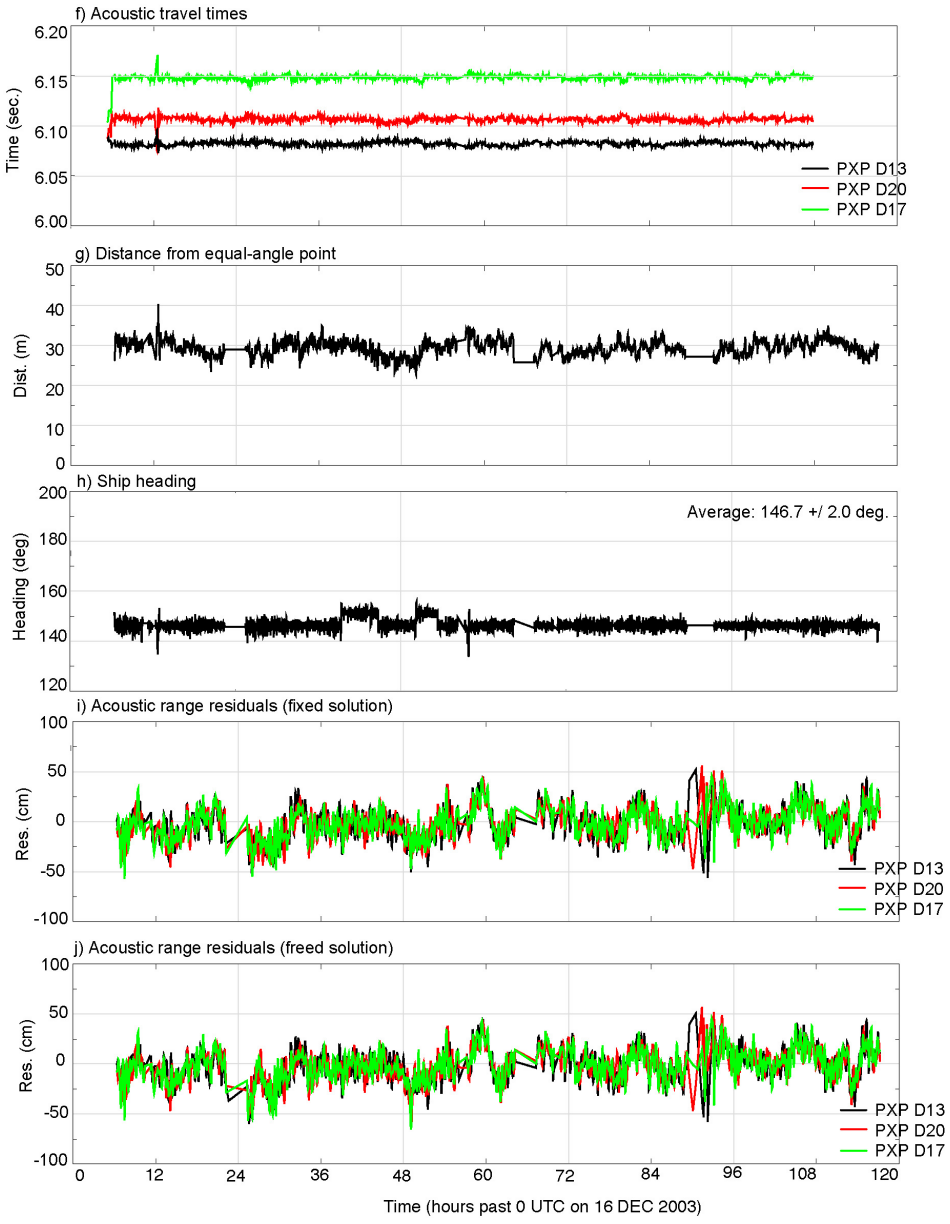

Figure II.27: Deep array, 2003, acoustic diagnostics (f-j).

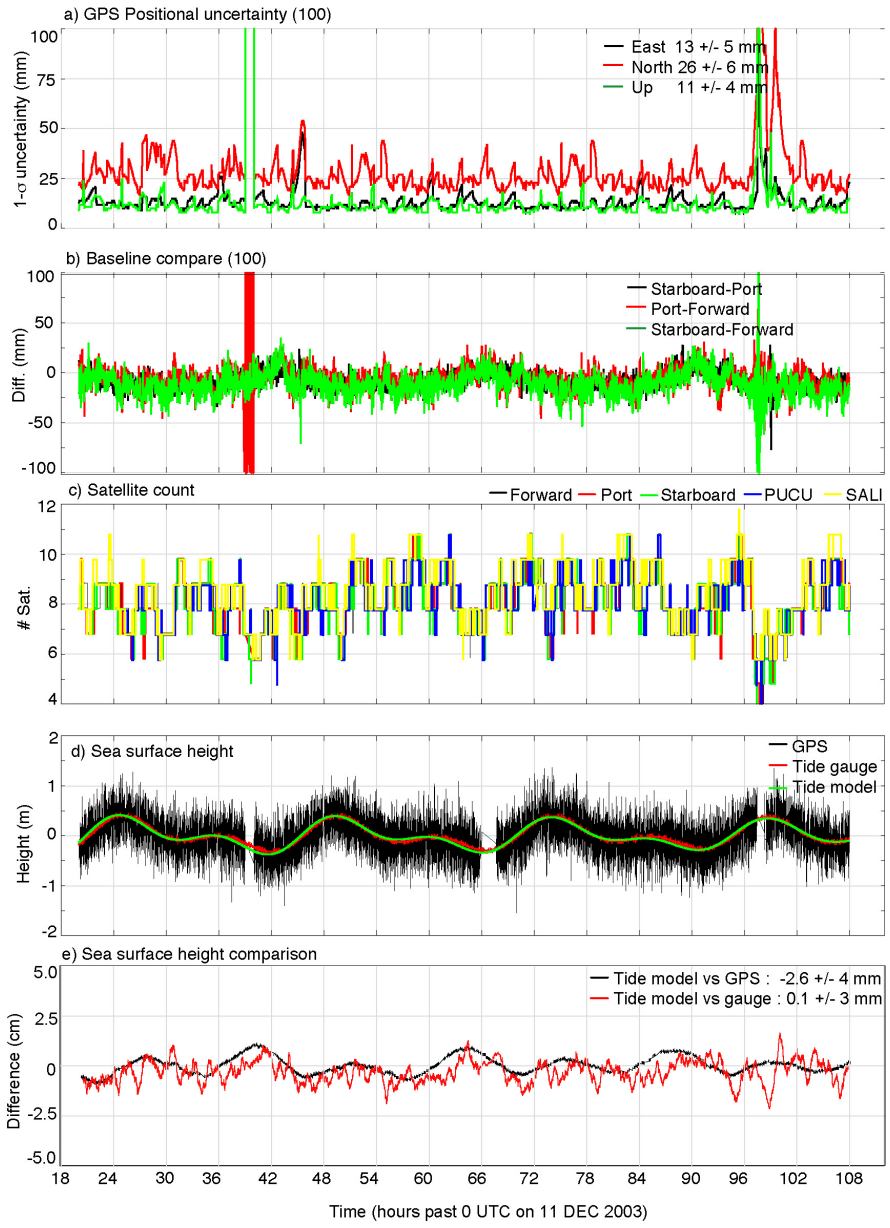

Figure II.28: Shallow array, 2003, GPS diagnostics (a-e).

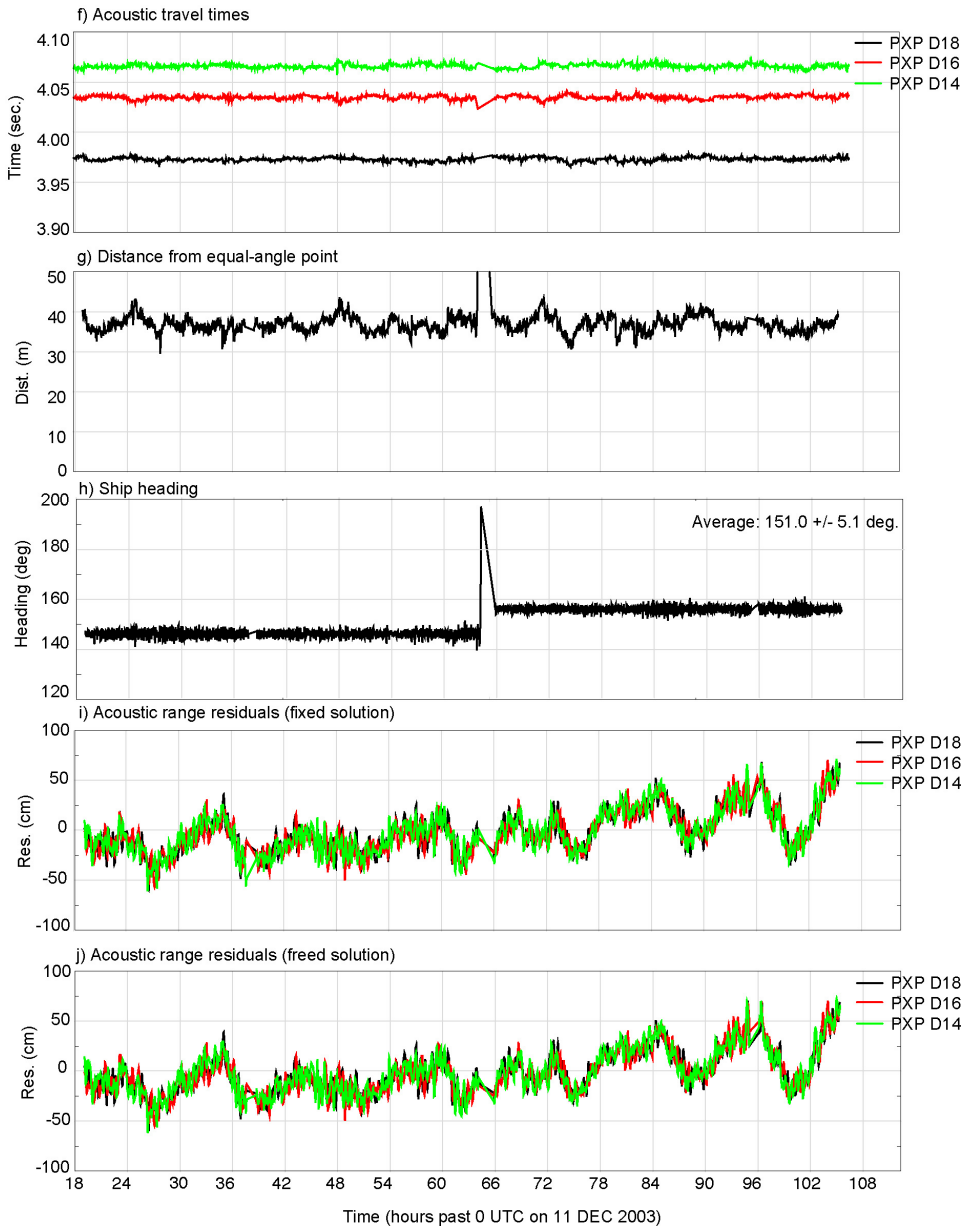

Figure II.29: Shallow array, 2003, acoustic diagnostics (f-j).

Information on the GPS-acoustic solutions in each epoch and in each array are shown in Figures II.4.B to II.29. The top plot (a) shows GPS east, north and up positional uncertainty from the kinematic solution for shipboard antennas. One representative antenna is used (Port). Large residuals indicate a low number of satellites. At the shallow array in 2003 (Figure II.25), two periods of low satellite observation counts increased the uncertainty to >100 mm, or the maximum uncertainty permitted in the GPSA solution. As in the moving surveys, the northward component of uncertainty is largest due to the geometry of coastal stations. There is also a 24 hour cycle of peak uncertainties due to the diurnal cycle of solar heating which changes electron density in the ionosphere. The average values are shown in the legend and range from 1-2 mm. The second plot (b) shows the comparison between GPS calculated antenna baselines and daily shipboard surveys for each antenna pair. The average baseline difference is -10 ±40 mm and follows a daily trend caused by solar heating of the ships frame. The negative average suggests a small systematic error in the measurement that has not yet been determined. The third plot shows the number of visible satellites throughout data collection. The number of satellites was above the minimum (4) for the majority of the data collection period. The next plot (d) shows sea surface height from the tide model, tide gauge and GPS height above the ellipsoid, normalized to the geoid. Finally, plot (e) at the bottom of the page shows a comparison between GPS height, 10-point running time average and tide gauge versus the tide model. The average difference ranged from 0.09-0.2 mm for the tide gauge and 0.04-1.7 mm for the GPS height.

The plot at the top of the second page (f) shows the acoustic signal two-way travel times for each transponder. The travel times did not change more than ±0.01 seconds, or ±15 m along the ray trace, during data collection. The second plot (g) shows the ships distance from the equi-angle point, again showing little variation (averaging < 10 m) in ship position due to dynamic positioning. The third plot (h) shows the ships heading. A full revolution of the ship would cause

Table II.6: Array displacement

Array	Lat. (°S)	Lon. (°W)	V (mm/yr)	Az (°)
Deep	12-16.36	78-29.18	53	78
Shallow	12-10.09	78-09.92	55	89

GPS phase wrap in the kinematic solution. The ship was able to maintain heading to within ±5° in each of the data collection periods. The bottom two plots show the acoustic range residuals for each transponder from the GPSA least-squares solution using fixed (i) and freed (j) GPS data. The residuals vary 20 to 50 cm peak-to-peak. Outliers were removed from the solution though they represented less than 0.0003% of the data. The random scatter of the residuals ensures that the solution is independent of cyclical changes in the sound speed such as ocean or solid earth tides. The resulting vectors of horizontal displacement relative to stable South America are shown in Table III.1 in the following section.

The largest contribution to the residuals is the un-modeled fluctuations in the upper ocean sound speed structure. This can be seen by calculating the harmonic mean sound speed (ss_{hm}) for each CTD cast to the depth of the transponder. The sound speed residual is calculated as

$$v_{ss} = (ss_{hm} - \bar{ss}_{hm}) * \bar{tt}, \tag{II.6}$$

where $\bar{ss}_{hm}$ is the average harmonic mean sound speed of all casts and $\bar{tt}$ is the average one-way travel time from the ship to the transponder. Figure II.30 shows the GPS-acoustic residuals and sound speed residuals. The residuals have similar trends thought some disagreement is expected since the CTD casts provide only 1 sound speed profile per hour and GPSA data are collected at once each 20 seconds. The frequency of GPSA data is much closer to the real time sound speed fluctuations. To a low order, this test does show that much of the fluctuation of GPSA residuals can be attributed to sound speed variability.

The GPS, acoustic and CTD observation equations are reiterated to minimize the acoustic range residuals. Two variations of this method were also per-

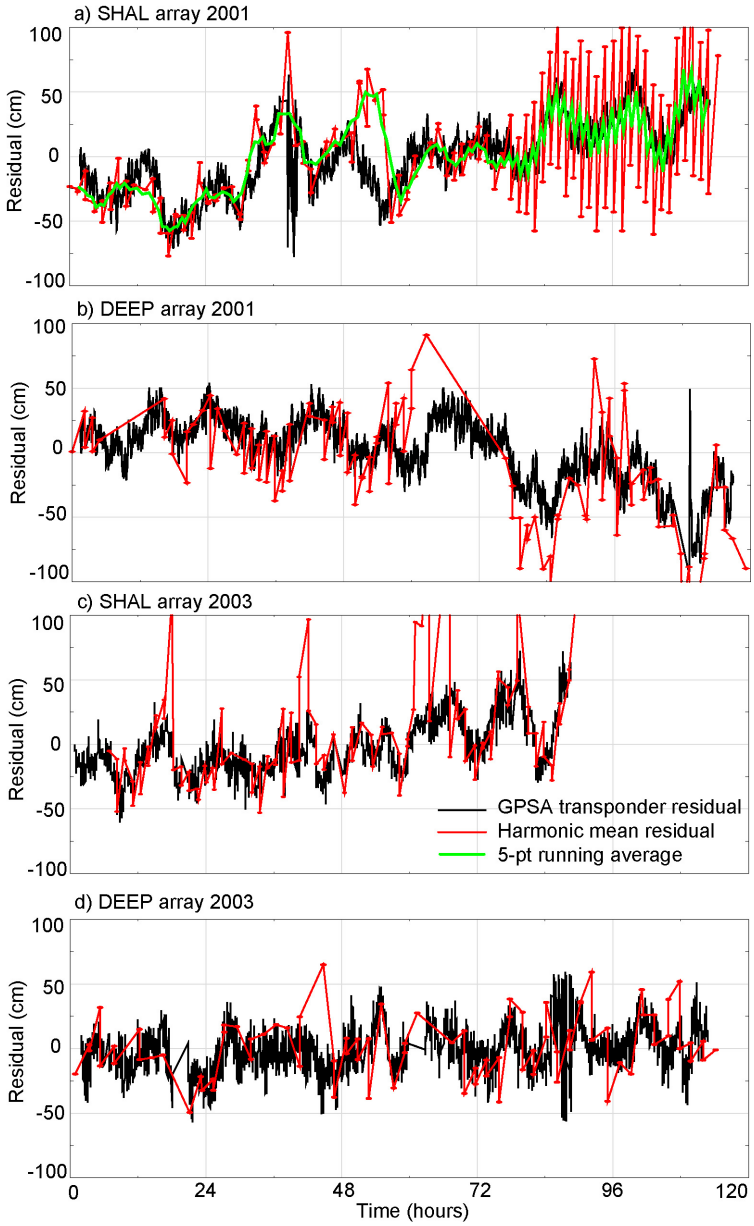

Figure II.30: a) Acoustic range residuals for transponder D16 in the shallow array, 2001 (black) and sound speed residuals (red), derived from the harmonic mean sound speed of each CTD cast. Ten-point time average (green) is shown during times of large variation in the harmonic mean sound speed. Large outliers have been removed. b) Acoustic range residuals for transponder D13 in the deep array, 2001. c) Acoustic range residuals for transponder D16 in the shallow array, 2003. d) Acoustic range residuals for transponder D13 in the deep array, 2003.

formed in order to analyze the repeatability of the final solution. The first variation divides the data into time bins of increasing length (cumulative solution). This provides an estimate on the amount of data needed to attain a certain level of repeatability. The second variation includes dividing the solution into set time bins, or a set number of acoustic replies (discrete solution). This randomized inversion shows the time dependence of the solution, e.g. if data collection began 24 hours later, would the data converge to the same solution.

The cumulative solution was performed with increasing 1-hour bins to determine how much data was needed to approach the final solution with ±10 mm repeatability (Figure II.31). Latitude and longitude are normalized to the final estimated position of the array. For all but the deep array in 2001, there is an initial convergence (within 10-30 mm) toward the final solution. For <10 mm repeatability, between 76 hours (shallow array, 2001) and 110 hours (deep array, 2001) of observations are needed.

The discrete solution was performed using 5-hr data bins. The normalized positions for the discrete solution are shown in Figure II.32. Using only 5 hours of data, the solution is not repeatable to more than 10 mm (shallow array, 2001) and can be as much as 700 mm distant (deep array, 2003). The deep array in 2001 remains more than 50 mm from the final solution for each 5-hr data bin.

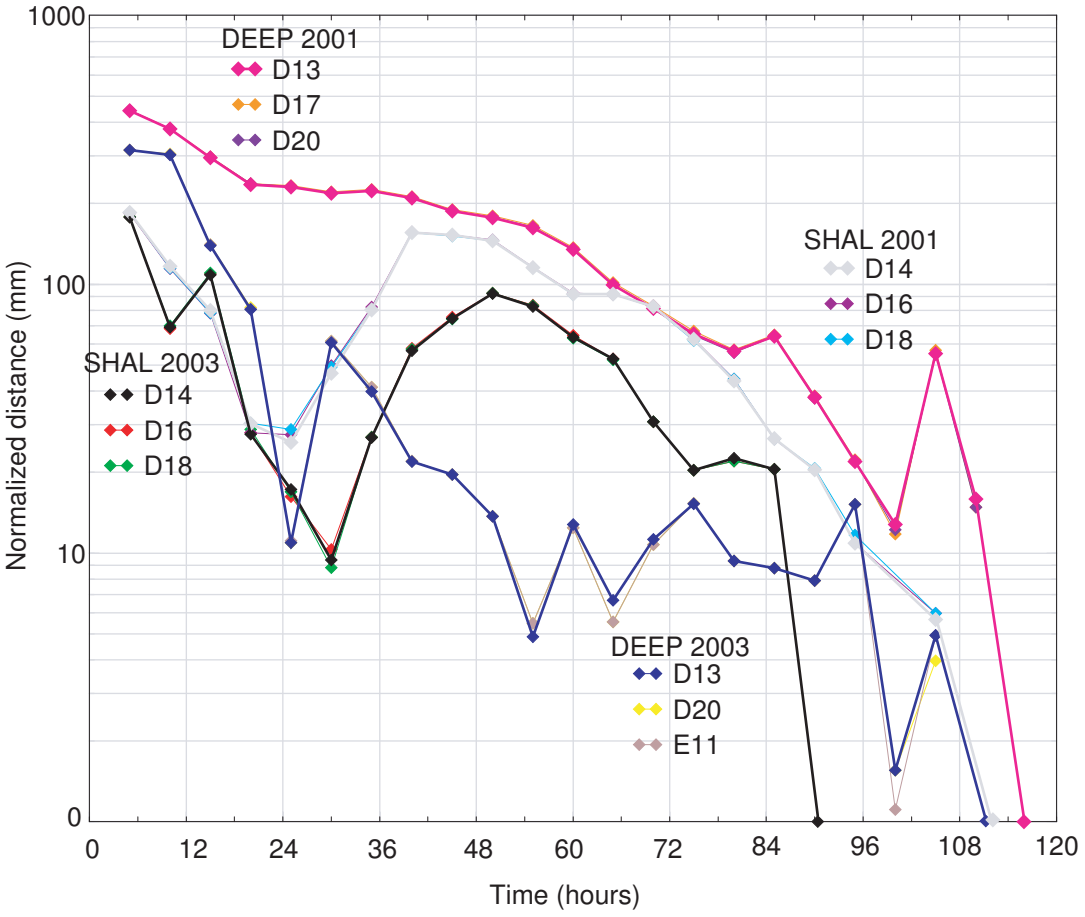

Figure II.31: Normal-log plot of GPS-acoustic, cumulative, 5-hour time bin, least-squares solutions at each array, in each epoch. Text indicates the array, epoch and array transponders. The solutions are normalized to final array position, i.e. with 5 hours of data, the deep array in 2001 is estimated to be 400 mm away from the position estimated with 115 hours.

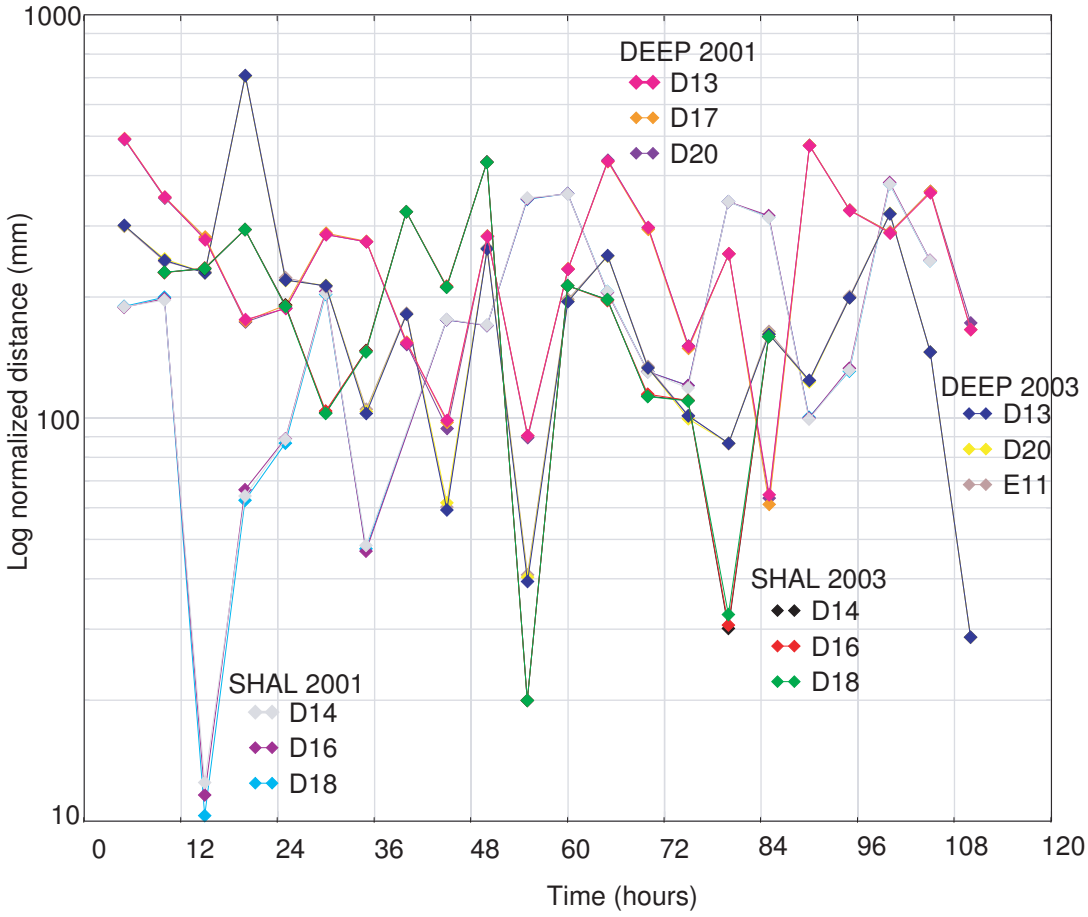

Figure II.32: Normal-log plot of GPS-acoustic, 5-hour set bin, least-squares solutions at each array, in each epoch. The solutions are normalized to final array position, i.e. after the first 5 hours of data collection, the shallow array in 2001 is estimated to be 200 mm from the final position using all data.

III

GPS-Acoustic results

This section includes an analysis of GPS-acoustic measurements from the shallow and deep arrays on the Peruvian margin. The plate motion estimates are used in kinematic models to investigate initiation of stick-slip behavior on the thrust fault. The results are interpreted in terms of local rheology, thermal properties, gravity surveys and seismic history. Also, an error analysis is performed for the land GPS stations and GPS-acoustic arrays to show uncertainty of the plate motion vectors.

The GPS-acoustic technique was used to determine plate motion on the submerged portion of the continental South America plate relative to stable South America. Additional campaign GPS stations on the coast were included to investigate deformation across the convergent margin. Table III.1 shows the perpendicular distance from the trench axis, latitude, longitude and velocity in the strike and dip direction for coastal GPS stations and the GPSA arrays. A bathymetric map of plate convergence, site velocities and 95% confidence ellipses is shown in Figure III.1.

An elastic dislocation model was created using 3D-def from the University of Memphis (Gomberg and Ellis, 1994). The geometry of the thrust fault is based on seismic reflection and refraction profiles from GEOPECO expeditions (Krabbenhoeft et al., 2004; Hampel et al., 2004). The surface of the elastic halfs-

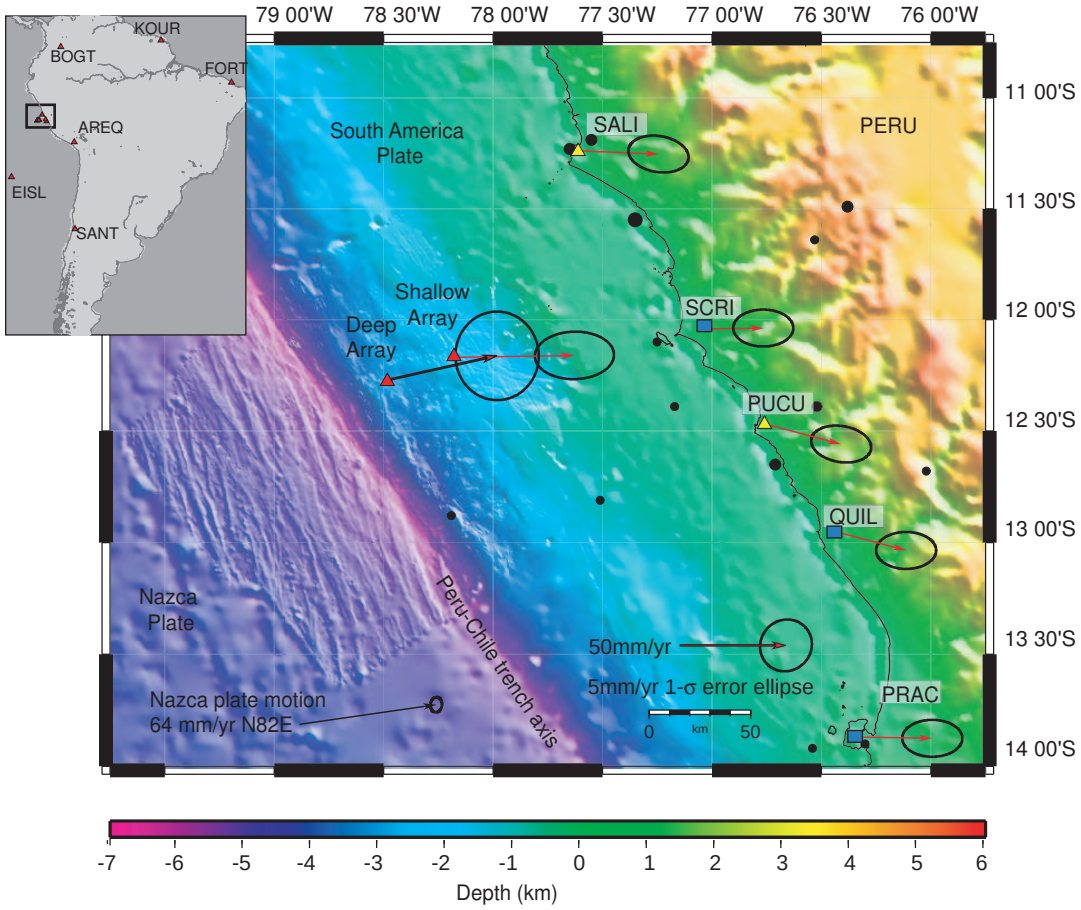

Figure III.1: Seafloor bathymetry offshore Peru with additional topography data from satellite altimetry (Smith and Sandwell, 1997). Red triangles represent deep and shallow transponder arrays 20 and 50 km from the Peru-Chile trench axis. Yellow triangles show campaign, land GPS stations at Pucusana (PUCU) and Salinas (SALI). Blue squares show additional land GPS stations from (Norabuena et al., 1999). Bathymetric data was collected in 2001 and 2003 from R/V Roger Revelle using SIMRAD EM 120. The REVEL plate convergence vector (64 mm/yr at N82E) is shown relative to stable South America (Sella et al., 2002). Vector solutions for campaign GPS stations and GPSA arrays were solved in ITRF00 (Altimini et al., 2002) and are shown with 1-σ error ellipses. Black circles show seismic events from USGS/NEIC PDE solutions between data collection periods in 2001 and 2003. Inset shows distant low-rate GPS stations (red triangles) Arequipa (AREQ), Bogota (BOGT), Galapagos (GALA), Kourou (KOUR), Fortaleza (FORT) and Santiago (SANT).

Table III.1: GPS station and GPSA array perpendicular distance from the trench axis, position, velocity (mm/yr) in strike and dip components and uncertainty (±mm/yr).

Station	Distance (km)	Lat. (°S)	Lon. (°W)	V_{dip} (mm/yr)	V_{str} (mm/yr)	Vector (mm/yr)	Az (°)
Deep	20	12-16.36	78-29.18	50±7	15±8	53	78
Shallow	50	12-10.09	78-09.92	48±7	26±6	55	89
PRAC	130	13-52.20	76-21.60	32±5	19±4	37	91
PUCU	170	12-27.96	76-45.54	26±6	26±4	37	105
QUIL	170	12-57.00	76-26.40	24±5	24±4	34	105
SALI	150	11-14.28	77-36.72	31±6	19±4	37	92
SCRI	160	12-02.40	77-01.80	22±5	13±4	26	89

pace was chosen at the depth of the trench axis, 6 km below sea level, similar to models created at the Juan de Fuca ridge (Flueck et al., 1997). This will preserve the geometry and material properties of the two plates near the trench axis, which is the area of concern in this study. The deep and shallow arrays overlie thrust fault depths of 2 and 6.7 km below the top of the elastic half space and roughly 4 and 10 km below the seafloor. Two planes account for varying dip of the fault plane: 5.7° from 0-3 km depth and 10.5° to 60 km depth below the seafloor, or the bottom of the model profile, shown in Figure III.2. The inspection plane, or the plane of model output, is at the seafloor. The updip limit is modeled from 0 down to 11 km depth while the downdip limit is modeled at 40 km depth with one profile extending down to 50 km depth. The relative displacement of elements along the thrust fault was determined using components of the convergence vector along strike, down dip and normal. Sella et al. (2002) estimated the Nazca-South America convergence vector to be 64 mm/yr at 82° using global GPS velocities in the ITRF00 frame. This is the most comprehensive and widely accepted plate motion model and is used for the interpretation of results. Additional estimates, shown in Table III.2, were also used to investigate horizontal deformation of the

Table III.2: Convergence rate (mm/yr), azimuth and strike, dip (6° and 10.5°) and normal components of convergence. The star shows the model used for interpretation of the results. Model A ((Sella et al., 2002)), B ((DeMets et al., 1994)), C ((Larson et al., 1997)), D ((Larson et al., 1997)), E ((Norabuena et al., 1999)).

Model	V (mm/yr)	Az (°)	V_s (mm/yr)	$V_{d=6°}$ (mm/yr)	$V_{d=10.5°}$ (mm/yr)	$V_n^{d=6°}$ (mm/yr)	$V_n^{d=10.5°}$ (mm/yr)
A*	64	82	24.0	59.6	60.3	5.9	10.8
B	75	81	26.9	70.4	71.2	6.9	12.7
C	68	85	28.7	61.9	62.7	6.1	11.2
D	58	80	19.8	54.8	55.4	5.4	9.9
E	64	80	21.9	60.4	61.2	6.0	10.9

seafloor as a result of displacement on the thrust fault.

Table III.3 shows additional input to the deformation model. The area and grid spacing of the deformation model and inspection plane were chosen to minimize edge effects. The resulting surface deformation perpendicular to the trench for model A is shown in Figure III.3. (Kinematic models using each convergence estimate are plotted in trench perpendicular, parallel and normal components in Figures III.13, III.14 and III.15.) The kinematic models show seafloor deformation as a result of relative motion of the hanging wall with respect to the footwall. These models are similar to those created by (Norabuena et al., 1999) with land GPS data, shown in Figure I.11. The GPSA array displacements agree with models of a thrust fault locked from the trench axis to 40 km depth (orange line) and 2 to 40 km depth (green line). The results do not allow differentiation between these models. The following section includes an interpretation of these results in terms of the nature of the shallow portion of the seismogenic zone during interseismic periods.

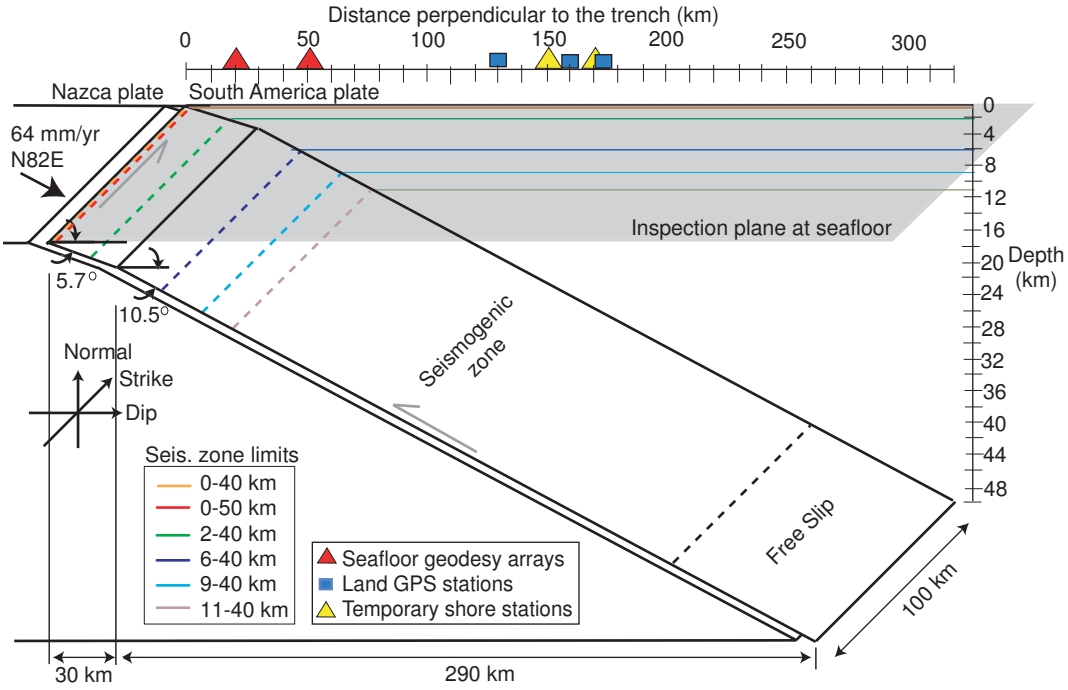

Figure III.2: Fault geometry used in the three dimensional model. Thrust fault includes two planes at 5.7° and 10.5°. Shaded area shows inspection plane, or the plane of the deformation model output, at the seafloor. Dashed, colored lines show increasing depth for initiation of unstable sliding on the thrust fault, from the trench axis, or 0, to 11 km depth. Legend shows width of the seismogenic zone for each model. The thrust fault slips freely updip and downdip of the seismogenic zone. Distances are in km, velocities in mm/yr. Light grey arrows show motion of the hanging wall with respect to the footwall. Station symbols match Figure III.1.

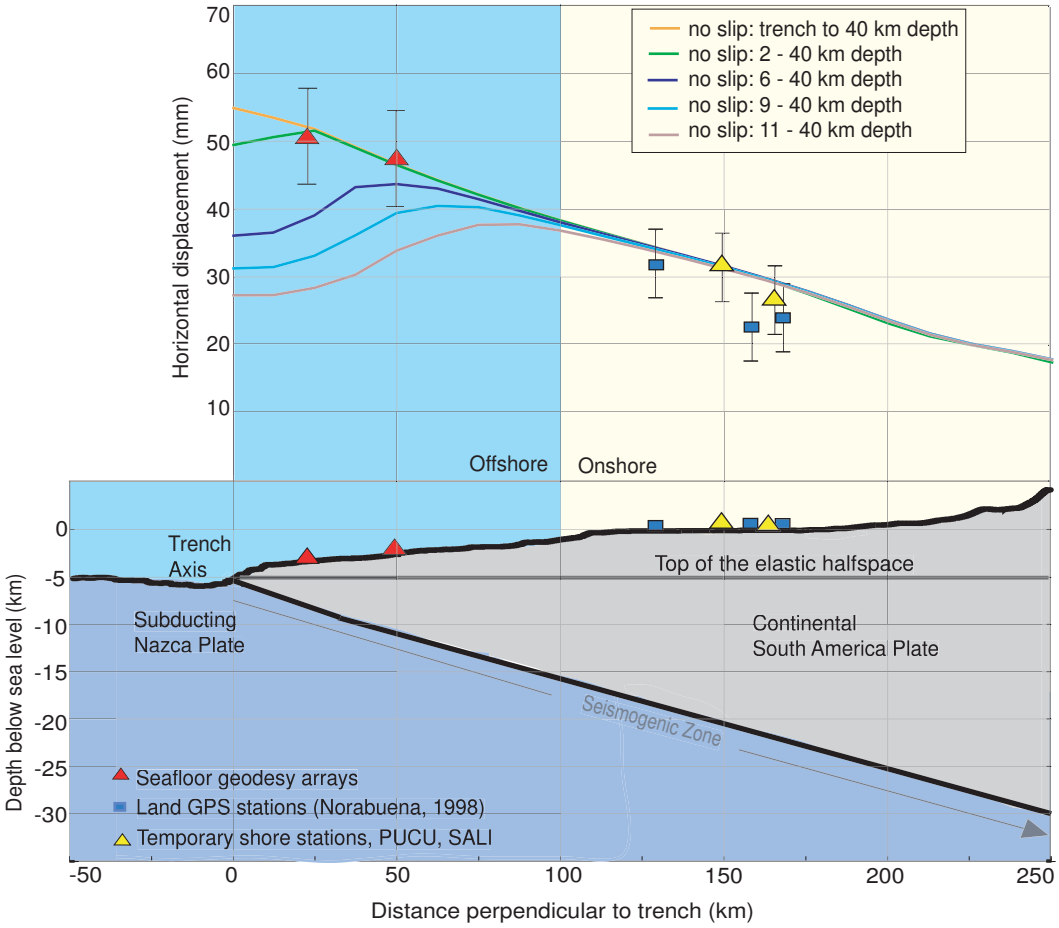

Figure III.3: Top frame shows kinematic model showing trench perpendicular component of seafloor displacement driven by convergence rates in model A (Table III.3). Colored lines show surface deformation in mm as a result of successively deeper initiation of unstable sliding (colors match Figure III.2). Stations symbols match Figure III.1. All distances plotted perpendicular to the trench axis. 1-σ error bars are shown for all velocities. Bottom frame shows seafloor topography from multibeam surveys and locations of GPS stations onshore and GPS-acoustic arrays offshore.

Table III.3: 3ddef model input

Poissons ratio, ν	0.25
Youngs modulus, ϵ	7.0E10
Coefficient friction, μ	0.6
Grid spacing	20 km

III.1 Interpretation

GPSA measurements agree with a kinematic model of shallow, interseismic coupling or a wide locked zone. This interpretation is limited to the timescale of the seismic cycle but provides an important and unique measurement of displacement on the upper plate. The kinematic model treats the continental plate as an elastic material and the interseismic period as a time when strain accumulates uniformly in the continental plate. Although this is a simplification of the problem, this approach is taken in the majority of kinematic and mechanical models of plate interactions from Section I.2. Shallow strain accumulation at the Peruvian margin is explored below with respect to seafloor structure and seismic history. Thermal properties, gravity and tectonic erosion of the margin are also discussed with respect to coupling, though these observations represent a much longer timescale. The possibility that shallow sediments do not behave elastically will also be explored below.

Seismic reflection and refraction profiles from GEOPECO (GEOphysical experiments along the PEruvian COntinental margin) reveal the subsurface rheology of the margin. Figure III.4 shows the GPSA arrays over different rheologic units (Krabbenhoeft et al., 2004) and Figure III.5 shows earlier studies of seismic reflection images at 12°S. Landward dipping reflectors close to the trench axis indicate off-scraped sediments from the oceanic plate, while the Eocene basement is seen roughly 20 km from the trench axis (Kukowski et al., 1994). The deep array, also 20 km from the trench axis, overlies roughly 3 km of sediments and the landward edge of the frontal, sedimentary prism. The shallow array overlies roughly 1

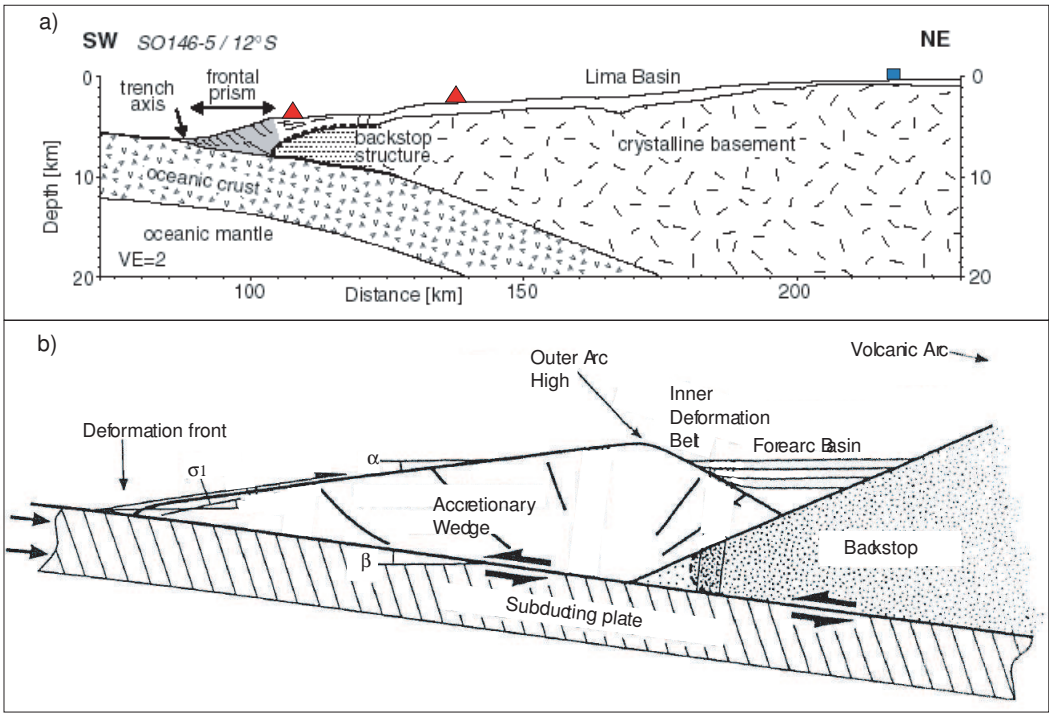

Figure III.4: a) Cross section of the convergent boundary at 12°S from GEOPECO seismic reflection and refraction surveys from (Krabbenhoeft et al., 2004). GPS station and transponder array symbols match Figure III.1. Rheologic units are contrasted by hatching. Deep array is located at the edge of the frontal accretionary prism, above the crustal backstop. The shallow array is located over a veneer of sediments and the crystalline basement. The Lima Basin is located roughly 50 km east of the shallow array. b) Sketch showing a cross section of forearc rheologic units from the accretionary wedge or frontal prism to the backstop from Byrne et al. (1993). Inner deformation belt is landward of the outer-arc high, followed by an undisturbed forearc basin between the accretionary wedge and the crustal backstop. Taper variables α and β are shown as well as maximum compressive stress, σ_1.

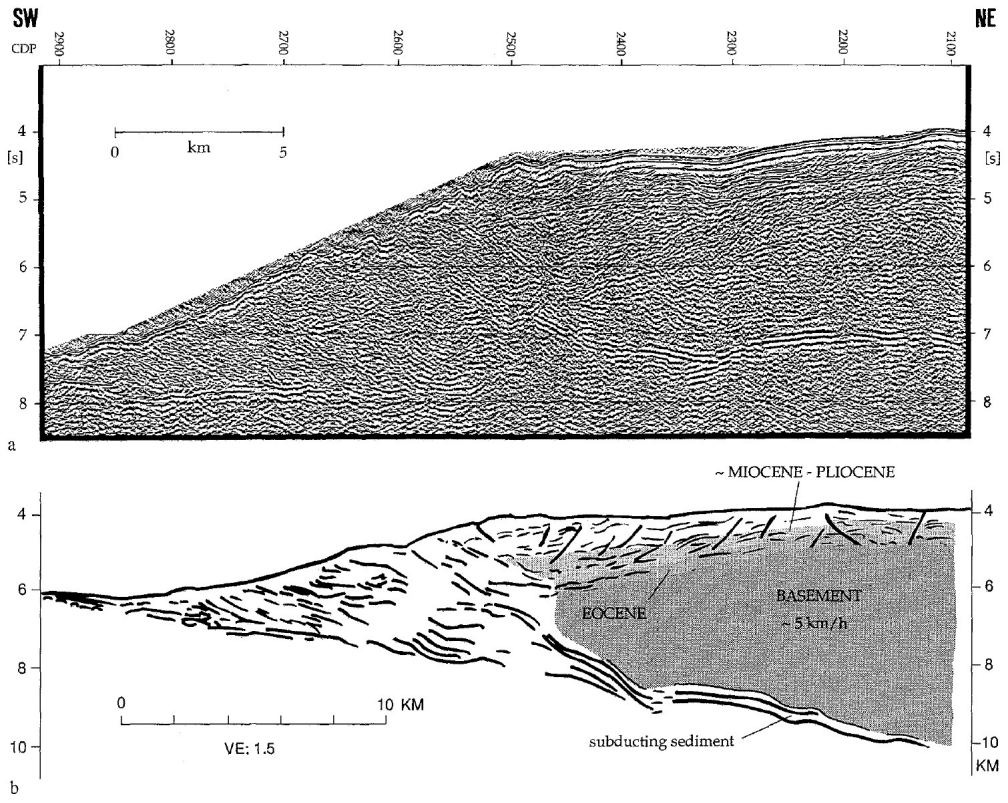

Figure III.5: a) Time migrated stack from seismic reflection line CDP-1, perpendicular to the trench axis from the southwest to northeast at 12°S, from (Kukowski et al., 1994). Plot shows shot number versus signal travel time in seconds. b) Interpretive drawing from seismic reflection image. Landward dipping reflectors are seen close to the trench axis while an Eocene, intermediate type backstop is shown as solid gray. Some sediment is seen below the backstop.

km of sediments and the crystalline basement. These units are discussed below.

The frontal prism is composed of accreted sediments from the oceanic plate or sediments derived from failure on the continental slope. The prism grows in strength and bulk density towards the continent (Byrne et al., 1993). It is generally convex with a topographic high, or outer-arc high, overlying the trenchward edge of the backstop. The outer-arc high can be seen at several margins that possess a backstop structure (Byrne et al., 1988). Seismic velocity observations and sand box models suggest the outer-arch high is created by upward buckling due to the initiation of coupling beneath the strong material of a type I to intermediate backstop (Byrne et al., 1988, 1993; Wang and Davis, 1996). Type I is reserved for backstops with a trenchward dipping contact with the frontal prism whereas a type II backstop has a shallow toe and dip (Byrne et al., 1993).

The backstop is generally defined as being able to support more deviatoric stress (mean of the normal stress components minus the normal stress components of the stress matrix) than the frontal prism. It can be composed of accreted, lithified sediment, allocthonous terrane or cystalline basement (Byrne et al., 1993). Sand box models show that a backstop assumes the majority of compressive stress and allows a relatively undeformed forearc basin to form. Uplift and deformation of the trenchward edge of the basin occurs as a result of basal friction (Byrne et al., 1993). Wells et al. (2003) observed a correlation between forearc basin formation and the downdip extent of megathrust events. At 12°S the Lima Basin has formed 100 km from the trench axis. It includes ponded terrigenous sediments bounded by a trenchward high in the continental basement. The Lima Basin is similar in shape to the Yaquina and Trujillo Basins to the north and the Pisco Basin to the south. Davis (1996) suggested the thickness of basin sediments reflects coupling strength beneath the backstop, with the strongest coupling along the Peru margin beneath the backstop near the Lima Basin. Landward of the prism and backstop, the crystalline basement is composed of metamorphic rock of Paleozoic or Precambrian age (Kulm et al., 1981).

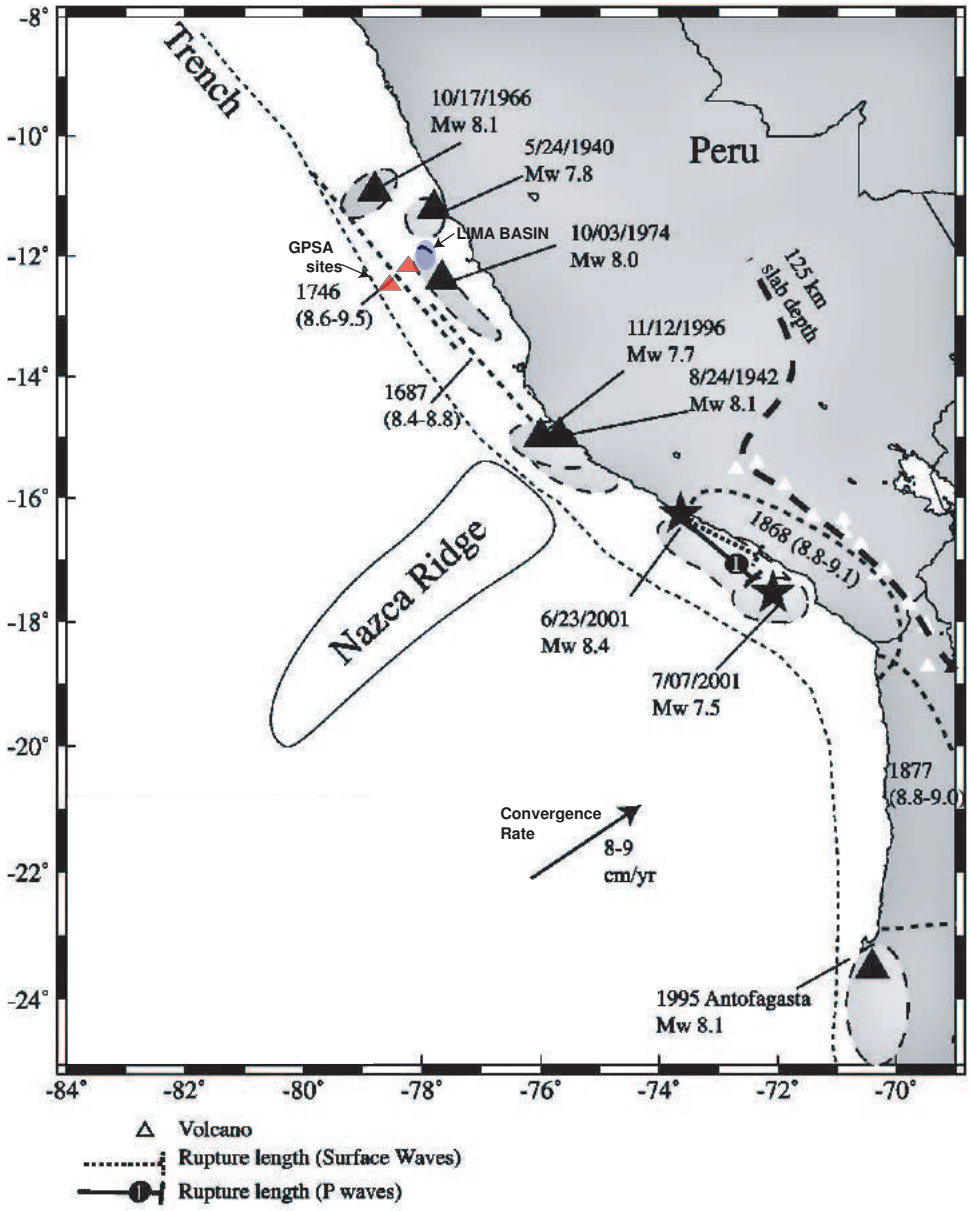

Figure III.6: Earthquakes, dates, magnitudes and rupture areas (shaded areas inside of dashed lines) at the Peruvian margin from (Bilek and Ruff, 2002). GPS-acoustic seafloor arrays shown as red triangles and Lima Basin shown as blue region landward of seafloor arrays. Bold, dashed line represents 125 km depth contour. Active holocene volcanoes shown as white triangles.

The agreement between shallow locking models and GPSA array displacements suggests that shallow, frictional instabilities exist on the thrust fault beginning between 0 and 2 km depth. In this case, elastic strain was accumulating between campaign measurements and could be released in a coseismic event that extends to within 20 km of the trench axis. Seismic records show several large events that ruptured within 50 km of the trench axis in this region. Earthquakes (M_w >7.5) occurred in 1940, 1942 (60 km depth), 1960, 1966, 1974 (13 depth km), 1996 (33 depth km) and 2001 (33 km depth) between 11-15°S (Figure III.6) (Bilek and Ruff, 2002). The seismic style offshore Peru is coupled, where large earthquakes occur infrequently followed by long periods of interseismic strain accumulation. This is contrasted with decoupled subduction zones, which have frequent, small events through conditionally stable regimes (Scholz, 1998). The seismic record portrays the spatial extent of frictional instabilities both along and across strike. Mechanical models in Section I.2 suggested that the shallow portions of the subduction zone may be conditionally stable, where earthquakes may propagate but do not nucleate.

Over a longer timescale, topography of the fore-arc may also indicate frictional instabilities. Topographic depressions, or regions with negative free-air gravity, are more likely to experience large coseismic moments (Song and Simons, 2003; Wells et al., 2003). Figure III.7 shows free-air gravity and recent, major seismic events around the Lima Basin. Low free-air gravity indicates a bathymetric depression or low-density sediment or thinner crust. Wells et al. (2003) find that on average, 79% of an earthquakes asperity area occur beneath the gravity-low, or deep sea terrace. At the Peruvian margin, long term basal erosion is thought to have caused forearc subsidence, estimated at 500 m/my or 25-50 km^3/my (Wells et al., 2003; von Huene and Lallemand, 1990; von Huene and Scholl, 1991). They suggest that there may be a relationship between slip, interseismic subsidence and subduction erosion.

In a similar study, Song and Simons (2003) showed a correlation between

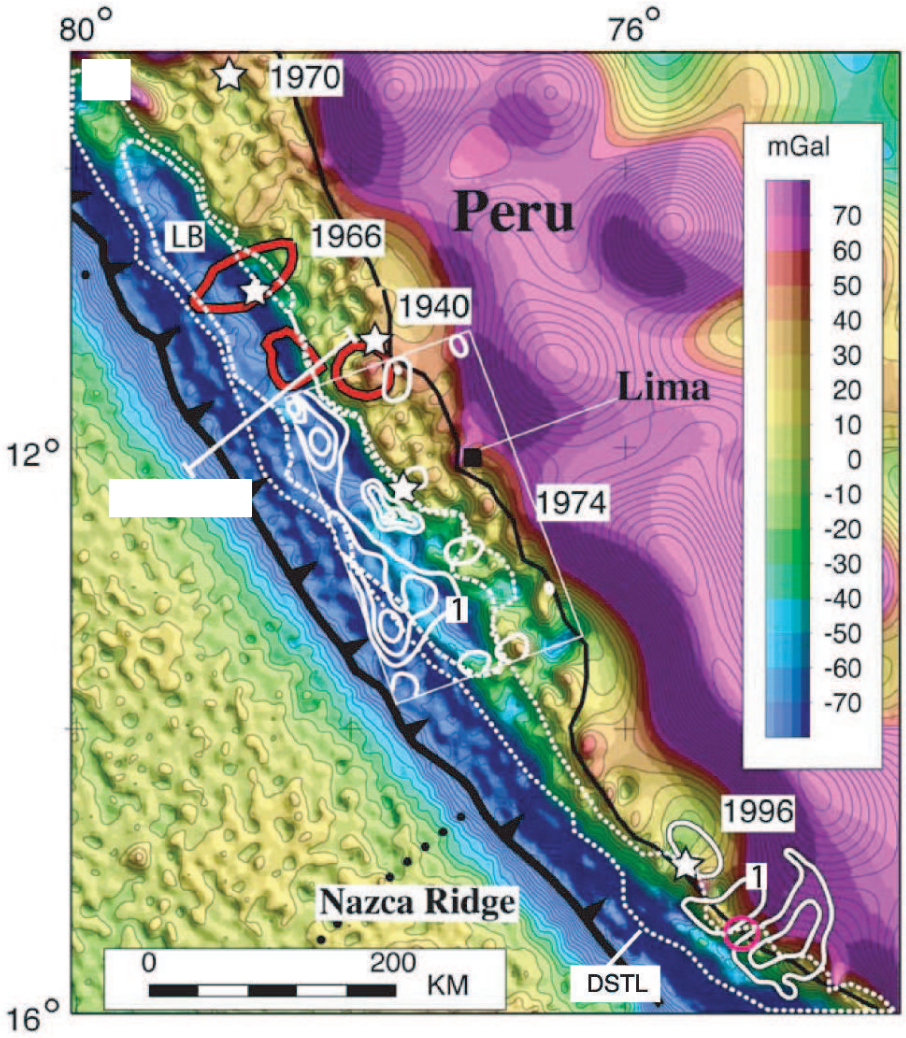

Figure III.7: Satellite derived free-air gravity (Smith and Sandwell, 1997) and seismic moment release for the largest twentieth century events at the Peruvian margin (Beck and Ruff, 1987; Hartzell and Langer, 1993; Spence et al., 1999; Swenson and Beck, 1999) illustrate the correlation between topographic depressions and large seismic moment, from (Wells et al., 2003). White stars show earthquake epicenters for 1940, 1966, 1970, 1974 and 1996 events. Seismic slip is shown in meters (solid, white contours show 1 meter slip). Bold, red lines show areas of highest moment release. Topographic depressions outlined in dashed white line: deep sea terrace low (DSTL) and Lima basin (LB). Black solid line shows Peruvian coast.

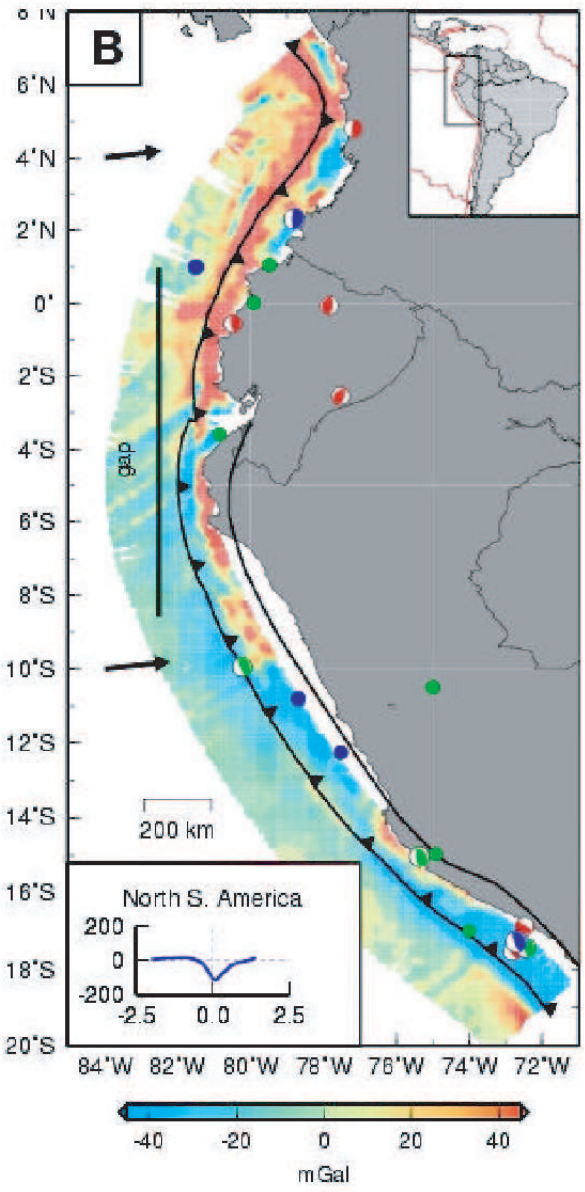

Figure III.8: Free-air gravity anomaly and seismic moment release to illustrate high correlation between great earthquakes and negative trench-parallel gravity anomalies (∼8-20°S), from (Song and Simons, 2003). Lower left inset shows the average trench-normal gravity profile (mGal) for northern S. America versus trench-normal distance from the trench axis (degrees). The average profile is subtracted from the observed free-air gravity to obtain the anomaly. Seismic events with M_w >7.0 (Harvard CMT 1976-2001) shown as solid circles and M_w >7.5 (ISC 1900-1976) shown as moment tensors. Black line shows 50-km slab depth contour and black barbed line shows trench axis. Black arrows show convergence direction. Black bar between 1°N and 8°S shows previously determined seismic gap from (Lay et al., 1982).

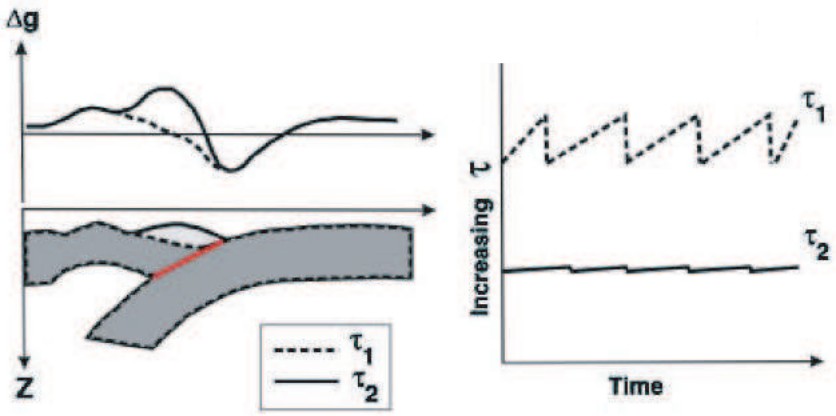

Figure III.9: Left frame shows topographic depression at the convergent boundary caused by high shear traction, τ_1 (dashed line) from (Song and Simons, 2003). Low shear traction, τ_2 (solid line), causes a topographic high. Right frame shows the seismic cycle as shear stress versus time. A higher shear traction (τ_1) causes large, infrequent seismic events.

trench parallel (free-air) gravity anomalies (TPGA) and great earthquakes at several convergent margins, including northern South America (Figure III.8). The trench-parallel gravity anomaly is calculated by subtracting the average trench-normal free-air gravity profile from the observed free-air gravity. A negative anomaly parallels the trench from 1°N and 8°S. Their model indicated a correlation between increasing shear traction (dashed line in Figure III.9) on the plate interface and a decrease in vertical compressive stress. A surface depression is created by high shear traction, a function of normal stress and the coefficient of friction (Song and Simons, 2003). Both studies indicate shallow frictional instabilities at this latitude of the margin: including investigations of both higher amplitude trench-normal free-air gravity and the smaller amplitude signature from trench-parallel gravity anomalies.

Thermal models have not been constructed for the subduction zone offshore Peru. Though thermal models average over a much longer timescale, they

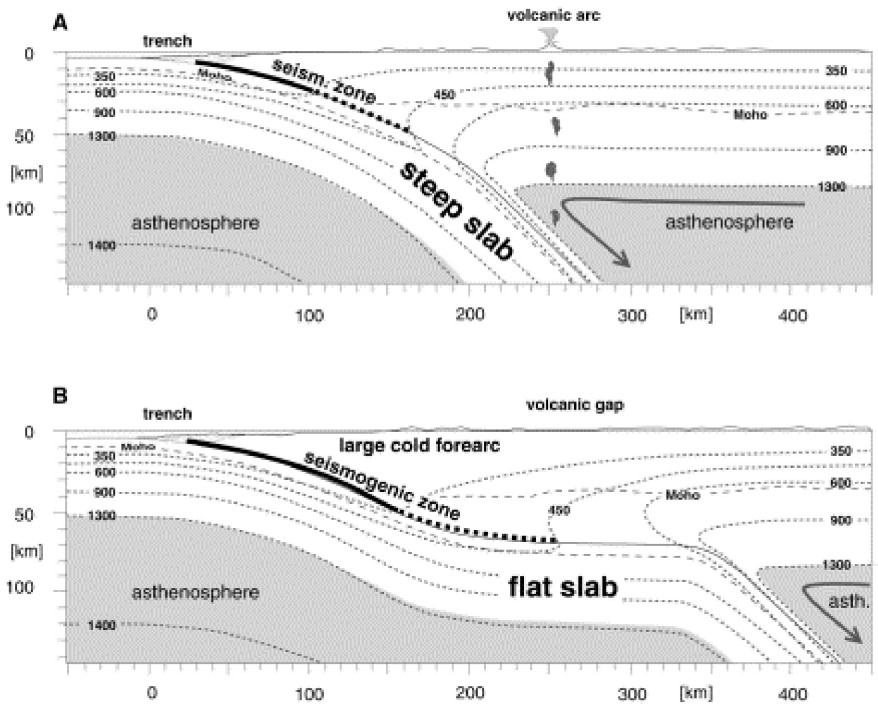

Figure III.10: Cartoon of thermal structure for flat and steep slab subduction at the Peru-Chile margin from (Gutscher, 2002). Large, cold forearc is expected to widen the seismogenic zone for regions of flat slab subduction. Seismogenic zone is shown in bold between 150-350°C and dashed from 350-450°C for downdip transition.

indicate differences between subduction style and thermal regime in the forearc. In southern Chile (32°S), a postive correlation was drawn between flat slab segments and large seismic energy release.Between 11-15°S the oceanic slab also descends at a shallow dip (6°) before leveling out for several hundreds of kilometers (Krabbenhoeft et al., 2004). The flat slab region in Peru is outlined by the dashed line, or 125 km depth contour, in Figure III.6. In regions of flat slab subduction, a large, cold forearc could widen the seismogenic zone, illustrated in the cartoon of thermal structure (Figure III.10) (Gutscher, 2002).

The GPSA observations cannot distinguish between models of the updip limit at 0 or 2 km depth. Based on various models and observations, it is likely that the upper 2 km are not fully coupled. The weak, unconsolidated sediments

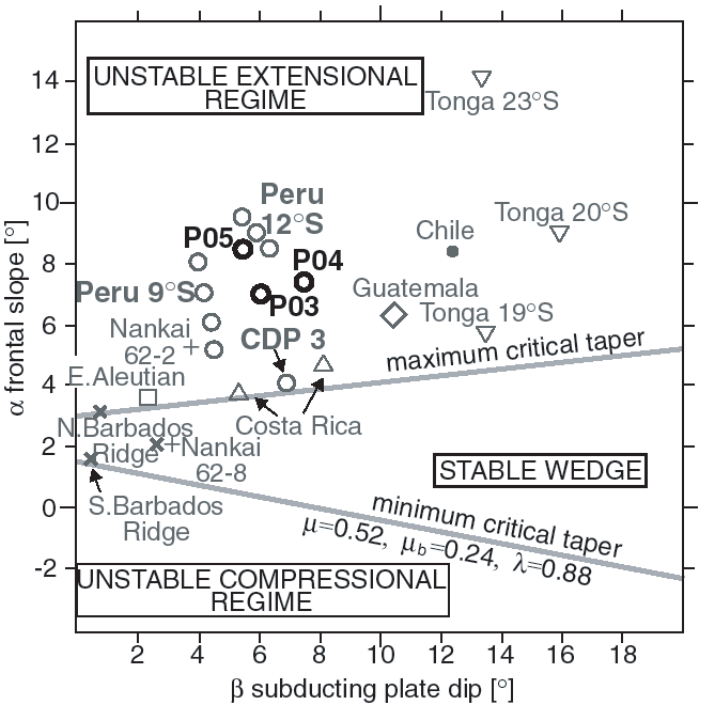

Figure III.11: Taper stability field for accretionary wedges at several margins based on frontal wedge slope (α) and subducting plate dip (β) in degrees from (Lallemand et al., 1994; von Huene et al., 1996). The lower boundary (solid, gray line) delimits minimum critical taper, below which continuous frontal accretion occurs. The upper gray line delimits maximum critical taper, above which erosion dominates. Between these boundaries the accretionary wedge is stable. Model parameters include friction (μ), basal friction (μ_b) and pore fluid pressure (λ).

in the accretionary prism may lack the strength to resist motion of the subducting plate. Byrne et al. (1988) suggested that unconsolidated or semiconsolidated sediments near the trench axis allow stable sliding, or aseismic deformation. Incoming sediments from the oceanic plate are either underplated on the base of the continental plate, accreted to the toe or deposited on the surface. Between 4-12°S, trench sediments are mostly southward migrating silt and sand turbidites interlayered with mud (Schweller et al., 1981). The porosity is initially high and permeability low. As the sediments are compacted, pore fluid pressures increase, which decreases the effective normal stress and results in low shear strength (Byrne et al., 1988). Unconsolidated sediments cannot accumulate strain until the shear

stress is greater than lithostatic. The seismic reflection and refraction generated profile (Figure III.4) shows low seismic velocity in the frontal prism, suggesting high porosity and low strength (Krabbenhoeft et al., 2004).

A shallow, aseismic region would be dominated by velocity-strengthening materials and high pore fluid pressures. These conditions are supported by subduction erosion, which contributes young (unconsolidated) sediments and fluid to the plate interface. Sallares and Ranero (2005) created a tectonic model of mass wasting (Figure III.12) for the Antofogasta region at 23°S. Basal erosion of the overriding plate brings sediments that release fluid during compaction. Increased fluid pressure allows stable sliding by decreasing the effective normal stress. Krabbenhoeft et al. (2004) observed large margin taper and evidence of bending of the oceanic plate between 8-15°S with wide-angle seismic data. Figure III.11 shows frontal prism angle, α, and ocean plate dip, β, at several margins, which demonstrate accretionary prism stability (Lallemand et al., 1994). The region discussed here is labeled as 12°S and is dominated by tectonic erosion. This interpretation represents an average behavior over many seismic cycles at the Peruvian margin.

The along-strike component of convergence was also investigated in the kinematic model. At 12°S convergence is oblique to the trench by $\sim$22°, such that the trench parallel, or along-strike, component of motion is directed southeast at 24 mm/yr. Figure III.14 shows along-strike displacement driven by convergence in models A-E (Table III.2). In general, the model predicts less trench parallel displacement than was measured with land GPS stations. The discrepancy may be caused by a decrease in obliquity away from the trench axis (Bevis and Martel, 2001) or motion of forearc slivers.

Figure III.15 shows the predicted vertical displacement, normal to the inspection plane, driven by convergence in models A-E. Small vertical displacements on the order of 10-20 mm/yr result from the stick-slip condition in the seismogenic zone. The predictions are limited to the vicinity of the trench as the model does not include far-field deformation or landward increase in plate thickness. Vertical

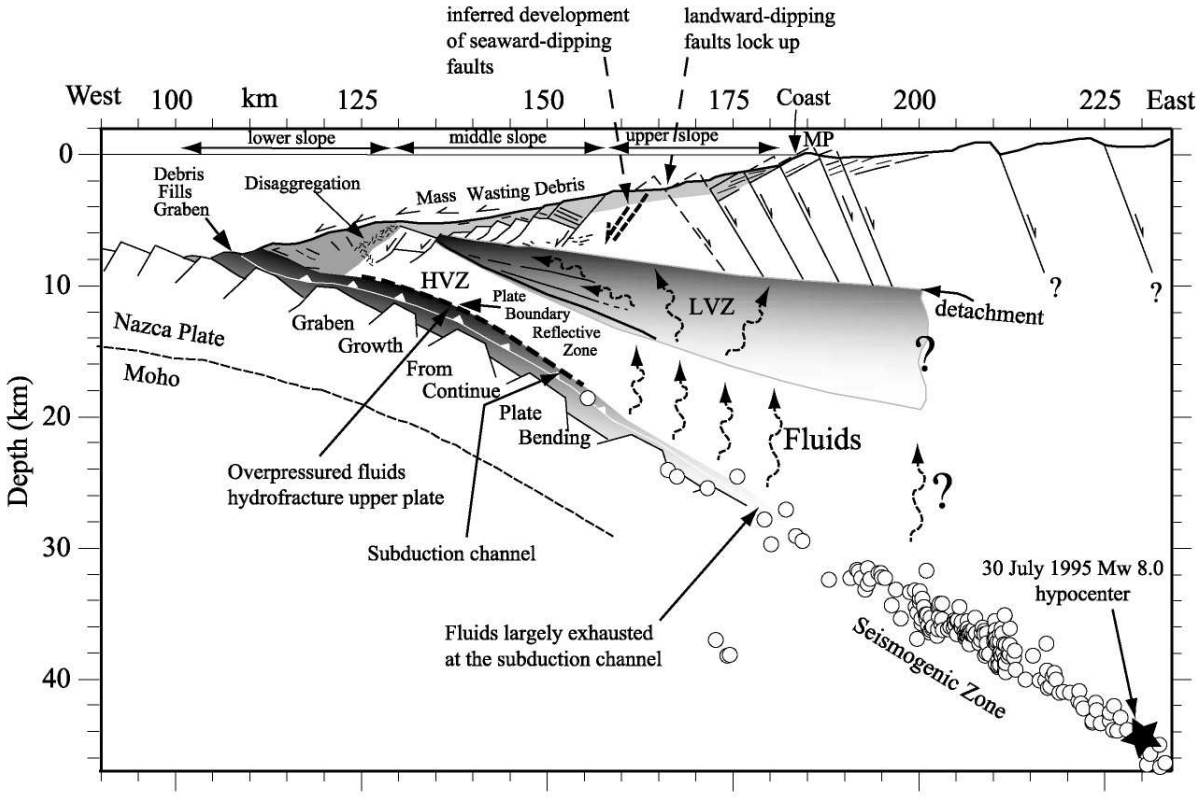

Figure III.12: Model of mass wasting, sediment subduction and fluid release based on the Chilean margin at 23° (Sallares and Ranero, 2005). Star marks hypocenter location of 30 July 1995, M_w8.0 earthquake and circles show aftershocks. Low-velocity zone (LVZ) exists below the lower slope where fluids have been expelled from subducted sediment compacted on the thrust fault. High-velocity zone (HVZ) exists above the decollement.

displacement is difficult to resolve with the GPSA technique due to poor observation geometry. Three methods for investigating vertical displacement are discussed in the following chapter. The vertical displacement observations are not shown in Figure III.15 since depth resolution was on the order of 30 mm.

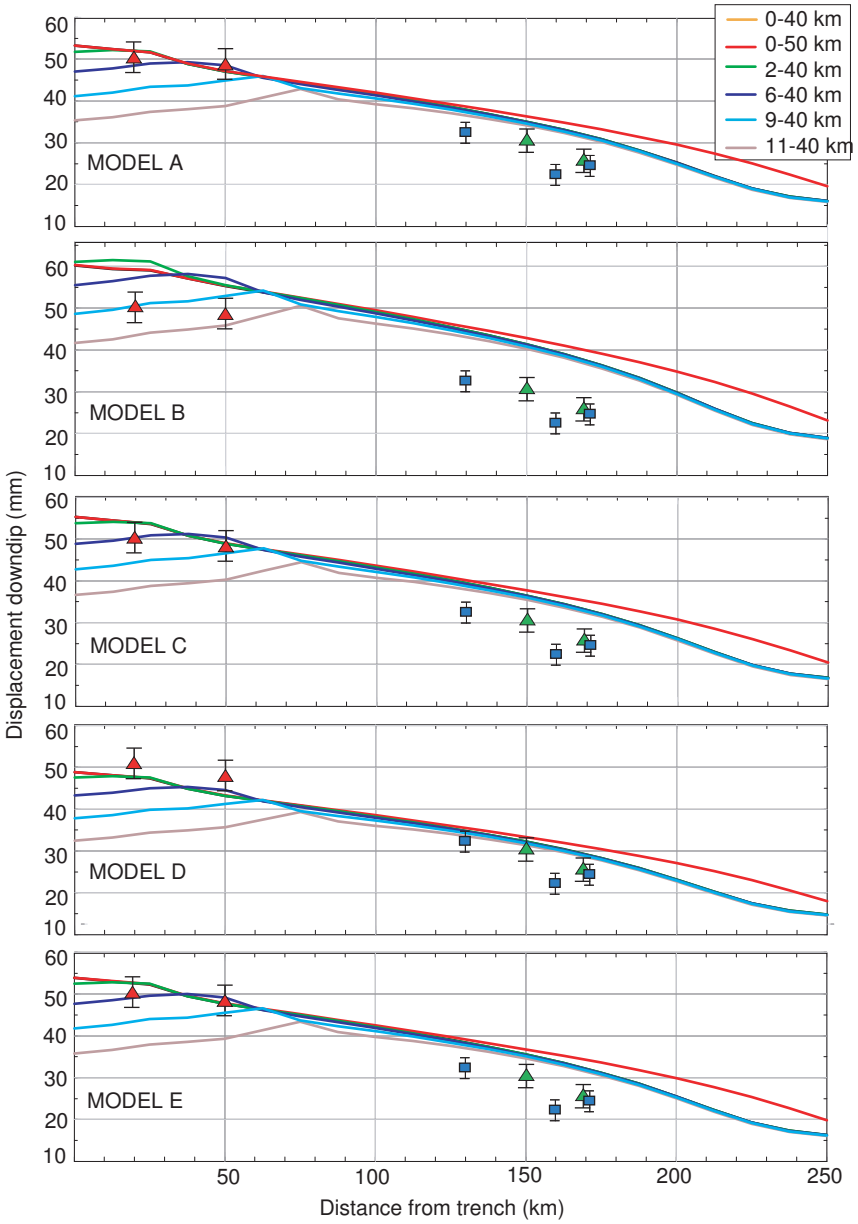

Figure III.13: Kinematic model showing down-dip, or trench perpendicular, component of seafloor displacement driven by convergence rates in models A-E, Table III.3. Trench perpendicular displacement of GPSA and GPS sites are shown; symbols match Figure III.2.

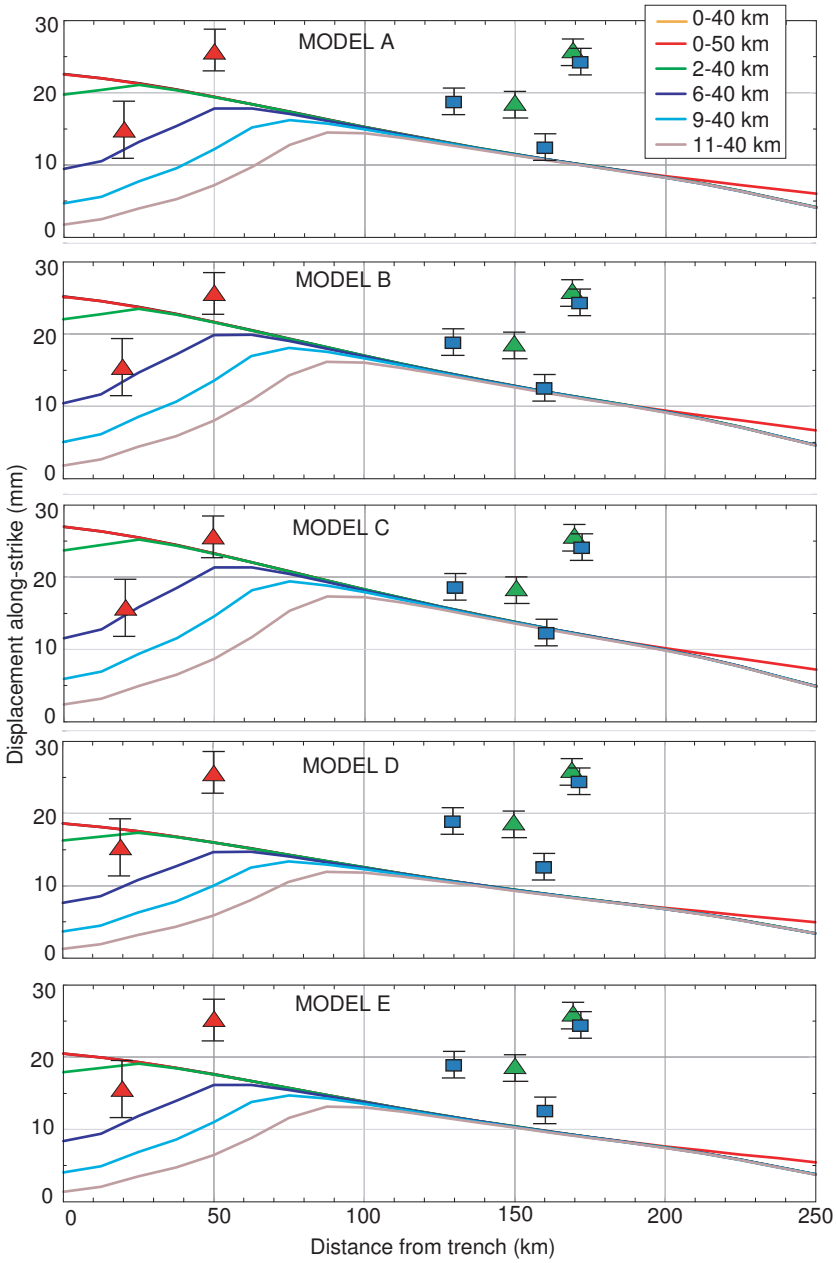

Figure III.14: Kinematic model showing along-strike component of seafloor displacement driven by convergence rates in models A-E, Table III.3.

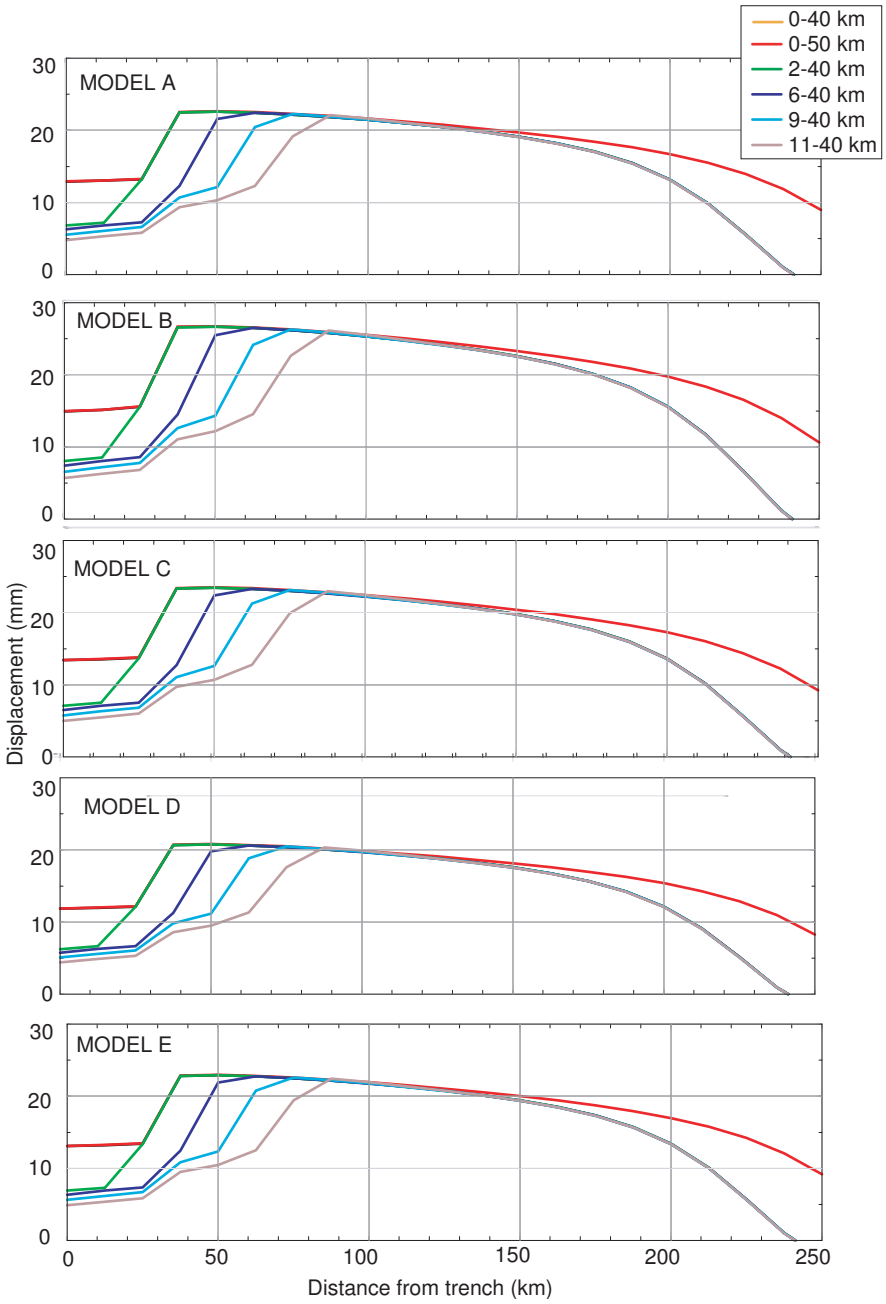

Figure III.15: Kinematic model showing normal component (vertical) of seafloor displacement driven by convergence rates in models A-E, Table III.3.

III.2 Error Analysis

The positional uncertainty of the GPSA array, $\mathbf{\Sigma}_P$, is a combination of several factors. The uncertainty from the kinematic GPS solution is multiplied by the formal error factor (3) from GIPSY-OASIS (Larson et al., 1997). Additional uncertainties are propagated from the shipboard total station survey, acoustic travel times and sound speed estimation. Finally, the uncertainty is scaled by the misfit of the data in the GPSA least-squares solution. As discussed in Section IV.1, a transponder relocation will add an additional ±16-29 mm to the positional uncertainty. At the deep array, the relocation contributed ±19 mm of uncertainty to the plate motion estimate. Table III.4 shows 1-σ x, y and z positional uncertainties and correlation coefficients for the GIPSY-OASIS solution for coastal GPS stations PUCU and SALI. The error is transformed from xyz to east, north and up coordinates with the rotation matrix,

Table III.4: 1-σ x, y and z uncertainties (±mm) and correlation coefficients (ρ) from GIPSY-OASIS.

Site	σ_x	σ_y	σ_z	ρ_{xy}	ρ_{xz}	ρ_{yz}
PUCU 2001	0.4488	1.4564	0.4424	-0.7178	-0.5773	0.7741
PUCU 2003	0.4221	1.3418	0.3967	-0.7453	-0.5732	0.7657
SALI 2001	0.4327	1.4584	0.4143	-0.6973	0.7433	-0.5474
SALI 2003	0.4077	1.3418	0.3697	-0.7078	-0.5293	0.7344

$$\mathbf{G}_{enu} = \begin{bmatrix} -sin\ \theta & cos\ \theta & 0 \\ -sin\ \lambda cos\ \theta & -sin\ \lambda sin\ \theta & cos\ \lambda \\ cos\ \lambda cos\ \theta & cos\ \lambda sin\ \theta & sin\ \lambda \end{bmatrix}, \tag{III.1}$$

where λ is longitude and θ is latitude. The covariance matrix for PUCU and SALI are represented in each epoch by

$$\mathbf{\Sigma}_{xyz} = \begin{bmatrix} \sigma_x^2 & \sigma_{xy}^2 & \sigma_{xz}^2 \\ \sigma_{yz}^2 & \sigma_y^2 & \sigma_{yz}^2 \\ \sigma_{zx}^2 & \sigma_{zy}^2 & \sigma_z^2 \end{bmatrix}. \tag{III.2}$$

Table III.5: East and north covariance ($\pm mm^2$), correlation coefficients (ρ), error factor (EF) and relocation uncertainty ($\pm$mm).

Site	σ_e^2	σ_n^2	σ_{en}	EF	σ_r
DEEP 2001	1.9174E-8	9.12118E-9	2.8157E-9	15.0	–
DEEP 2003	2.4529E-8	1.44813E-8	6.52905E-9	8.3	19
SHAL 2001	1.9778E-8	9.132E-9	2.6774E-9	16	–
SHAL 2003	2.8584E-8	1.5447E-8	6.4274E-9	12	–

and rotated with

$$\mathbf{\Sigma}_{enu} = \mathbf{G_{enu}}\mathbf{\Sigma}_{xyz}\mathbf{G}'_{enu}. \tag{III.3}$$

Table III.5 shows the east and north covariance, correlation coefficient and error factors of the deep and shallow array positions from the GPSA least squares adjustment. The 1-σ relocation uncertainty is included for the deep array in 2003. The observations of east and north array position in the t_o and t_i epochs include

$$\mathbf{obs} = \begin{bmatrix} E_o \\ N_o \\ E_i \\ N_i \end{bmatrix}. \tag{III.4}$$

The east and north velocity is

$$Ve = \frac{E_i - E_o}{t_i - t_o}, \tag{III.5}$$

and

$$Vn = \frac{N_i - N_o}{t_i - t_o}. \tag{III.6}$$

The rotation matrix of partial derivatives is written

$$\mathbf{G}_{VeVn} = \begin{bmatrix} \frac{\delta Ve}{\delta E_o} & \frac{\delta Ve}{\delta N_o} & \frac{\delta Ve}{\delta E_i} & \frac{\delta Ve}{\delta N_i} \\ \frac{\delta Vn}{\delta E_o} & \frac{\delta Vn}{\delta N_o} & \frac{\delta Vn}{\delta E_i} & \frac{\delta Vn}{\delta N_i} \end{bmatrix}, \tag{III.7}$$

where

$$\frac{\delta Vn}{\delta N_o} = \frac{-1}{t_i - t_o}, \tag{III.8}$$

$$\frac{\delta Vn}{\delta N_i} = \frac{1}{t_i - t_o}, \tag{III.9}$$

$$\frac{\delta Ve}{\delta E_o} = \frac{-1}{t_i - t_o}. \tag{III.10}$$

$$\frac{\delta Ve}{\delta E_i} = \frac{1}{t_i - t_o}. \tag{III.11}$$

The rotation matrix with these values becomes

$$\mathbf{G}_{VeVn} = \begin{bmatrix} \frac{-1}{t_i - t_o} & 0 & \frac{1}{t_i - t_o} & 0 \\ 0 & \frac{-1}{t_i - t_o} & 0 & \frac{1}{t_i - t_o} \end{bmatrix}. \tag{III.12}$$

The uncertainty of the observations is

$$\mathbf{\Sigma}_{obs} = \begin{bmatrix} \sigma^2_{eo} & \sigma^2_{eno} & 0 & 0 \\ \sigma^2_{neo} & \sigma^2_{no} & 0 & 0 \\ 0 & 0 & \sigma^2_{ei} & \sigma^2_{eni} \\ 0 & 0 & \sigma^2_{nei} & \sigma^2_{ni} \end{bmatrix}, \tag{III.13}$$

and rotating the uncertainty to east and north components is completed with

$$\mathbf{\Sigma}(gpsa)_{VeVn} = \mathbf{G}_{VeVn}\mathbf{\Sigma}_{obs}\mathbf{G}'_{VeVn}. \tag{III.14}$$

The motion of stable South America is added to the velocity of each array to isolate deformation of the convergent margin. The uncertainty of the motion of stable South America ($\mathbf{\Sigma}(sa)_{VeVn}$) is

$$\mathbf{\Sigma}(sa)_{VeVn} = \begin{bmatrix} \sigma^2_{Ve} & \sigma^2_{VeVn} \\ \sigma^2_{VnVe} & \sigma^2_{Vn} \end{bmatrix}, \tag{III.15}$$

and is derived from the absolute rotation pole in ITRF00 (Altimini et al., 2002). Table III.6 shows $\mathbf{\Sigma}(sa)_{VeVn}$ at the GPS and GPSA sites. Adding this to the GPSA uncertainty,

$$\mathbf{\Sigma}(conv)_{VeVn} = \mathbf{\Sigma}(gpsa)_{VeVn} + \mathbf{\Sigma}(sa)_{VeVn}. \tag{III.16}$$

Rotating the combined vector uncertainty to trench parallel (strike) and trench

Table III.6: 1-σ east and north uncertainties ($\pm$mm) and correlation coefficient (ρ) of $\mathbf{\Sigma}(sa)_{VeVn}$ at GPS and GPSA sites.

Site	σ_{Ve}	σ_{Vn}	$\rho_{e,n}$
SALI	0.00286	0.00621	-0.171
PUCU	0.00282	0.00618	-0.154
DEEP	0.00279	0.00617	-0.154
SHAL	0.00278	0.00618	-0.156

perpendicular (dip), the rotation matrix is

$$\mathbf{G}_{VsVd} = \begin{bmatrix} cos\ \omega & sin\ \omega \\ -sin\ \omega & cos\ \omega \end{bmatrix}, \tag{III.17}$$

where ω is the angle between the azimuth and the trench axis, $\sim$25°. The covariance matrix in the strike and dip directions is

$$\mathbf{\Sigma}(conv)_{VsVd} = \mathbf{G}_{VsVd}\mathbf{\Sigma}(conv)_{VeVn}\mathbf{G}'_{VsVd}. \tag{III.18}$$

The values of $\mathbf{\Sigma}(conv)_{VsVd}$ are shown in Table III.1 for campaign and coastal GPS stations and GPSA arrays.

IV

Transponder Relocation

The baseline length of the seafloor transponder array is held fixed in the least-squares solution such that the average horizontal displacement of each transponder reflects horizontal plate motion. If one transponder in the array ceases to function, a new one is installed. This chapter includes techniques to accurately position a replacement transponder (Gagnon and Chadwell, 2007). Using these techniques, a transponder relocation from 2003 is shown to contribute ±19 mm to array positional uncertainty. Finally, a simulation is performed to demonstrate optimal geometry of the survey network. Future relocations using this geometry could contribute as little as ±10 mm uncertainty.

In 2003, a transponder relocation was performed at the deep array, where PXP D17 was found inactive and a new PXP, E11, was placed within 3 m of D17. In order to reference the previous GPSA survey, the new array orientation, or more specifically, the precise offset from the inactive to the new transponder had to be determined. In general, when one transponder becomes inactive (PXP C in Figure IV.1), Equation IV.25 becomes,

$$\mathbf{P} = \frac{\mathbf{A} + \mathbf{B} + \mathbf{D}}{3}, \tag{IV.1}$$

where

$$\mathbf{D} = (\phi, \lambda, H)_{Dt_1} - (\phi, \lambda, H)_{Dt_0}. \tag{IV.2}$$

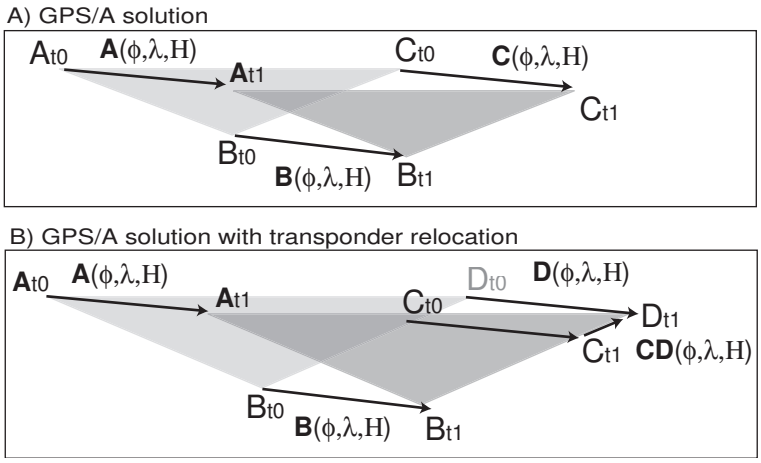

Figure IV.1: A) Displacement of a rigid array of transponders A, B and C from time t_0 to t_1. The position of each transponder is made up of the absolute latitude, ϕ, longitude, λ and height, H. B) Displacement of the array when transponder C is inactive and replaced by transponder D at t_1.

Assuming that $\mathbf{C} = \mathbf{D}$, Equations II.4 and IV.2 become,

$$(\phi, \lambda, H)_{Dt_0} = (\phi, \lambda, H)_{Ct_0} + [(\phi, \lambda, H)_{Dt_1} - (\phi, \lambda, H)_{Ct_1}], \tag{IV.3}$$

where $(\phi, \lambda, H)_{Dt_0}$ is the position of the new transponder in the previous epoch which is used in the t_1 GPSA least-squares solution. The term $[(\phi, \lambda, H)_{Dt_1} - (\phi, \lambda, H)_{Ct_1}]$ represents the offset from the new transponder to the inactive and can be more simply written as

$$\mathbf{CD}_{t_1} = (\phi, \lambda, H)_{Dt_1} - (\phi, \lambda, H)_{Ct_1}. \tag{IV.4}$$

Two techniques are used to determine $\mathbf{CD}_{t_1}$ in components of the global reference frame, i.e., latitude, longitude, and height offsets, at the seafloor. These techniques are a GPSA circle drive with range differencing and an acoustic/optical survey at the seafloor. First, a temporary, recallable transponder (PXP E) is placed in the vicinity ($\sim$3 m) of the inactive and replacement transponders, shown in the relocation network in Figure IV.2. The ship drives a 1-nm-radius circle centered on the active transponders while acoustically interrogating (Figure IV.3). The direct

ranges to the replacement transponder are used in a least-squares adjustment to provide $(\phi, \lambda, H)_{Dt_1}$. Next, travel times to both the replacement and temporary transponders are differenced at each epoch to determine their latitude, longitude and height offsets ($\mathbf{DE}_{t_1}$ or bold, dashed line in Figure IV.2). The 1-3 m baseline, $\mathbf{DE}_{t_1}$, creates a common acoustic ray path to the transponders, eliminating any unmodeled variability in the sound speed and providing the length component of the baseline with millimeter resolution. The orientation of the length components is controlled by GPS and the uncertainty is constrained by

$$\frac{\sigma_{DE}}{\mathbf{DE_{t_1}}} \propto \frac{\sigma_{GPS}}{\phi_{circle}}, \tag{IV.5}$$

where σ_{GPS} represents the GPS positional uncertainty and ϕ_{circle} is the diameter of the circle drive. The ratio of the baseline to the circle diameter is roughly 1:1800, reducing the baseline uncertainty, σ_{DE}, by a factor of 0.05 %. The acoustic range residuals of the dual transponder circle drive is shown in Figure IV.4a. Figure IV.4b shows the difference in replacement and temporary transponder residuals revealing an occasional 5 cm gap caused by peak jumping during acoustic signal correlation. These few points do not affect the $\mathbf{DE}_{t_1}$ calculation. The offset between the temporary and live transponder had an uncertainty of ±1.7 mm east, ±2.1 mm north and ±0.8 mm up.

The second technique used in the relocation is the acoustic and optical (A/O) survey. Acoustic ranges are measured from the seafloor survey package (SSP) to active transponders (solid lines in Figure IV.2) and optical ranges are measured to all transponders (gray, dashed line in Figure IV.2). This provides not only the depth of each transponder, but the offset from the live to the inactive transponder ($\mathbf{CD}_{t_1}$ or double line in Figure IV.2). Calculations for transponder depth using the acoustic and optical survey are explained in Section V.2.

A linearized least-squares adjustment with the above observation models is used to determine the position of all SSP landings and active/inactive transponders. The overdetermined system of observations, $\mathbf{O}$, and unknown parameters, $\mathbf{x}$, are listed in Table IV.1. They are related by

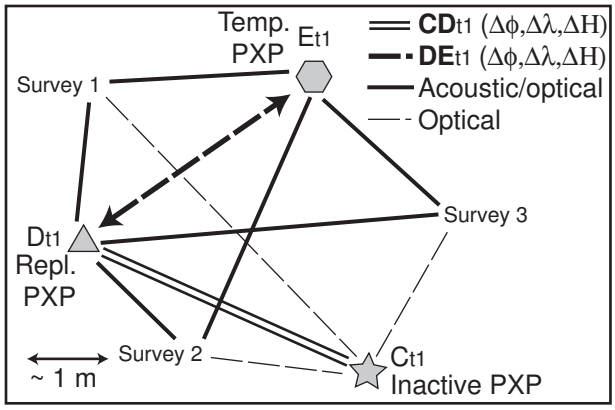

Figure IV.2: Relocation network showing three survey landings with the seafloor survey package (SSP) and three transponders. The star represents the acoustically inactive transponder (Ct_1), the triangle represents the replacement transponder (Dt_1) and the hexagon represents the temporary transponder (Et_1). Acoustic ranges are taken from the transducer on the survey package to the active transponders while optical ranges are taken from the survey camera to each transponder. The latitude, longitude and height offsets from the replacement to the temporary transponder ($\mathbf{DE}t_1$) are determined with the GPSA circle drive. The latitude, longitude and height offsets from the replacement to the inactive transponder ($\mathbf{CD}t_1$) are determined with the acoustic/optical survey.

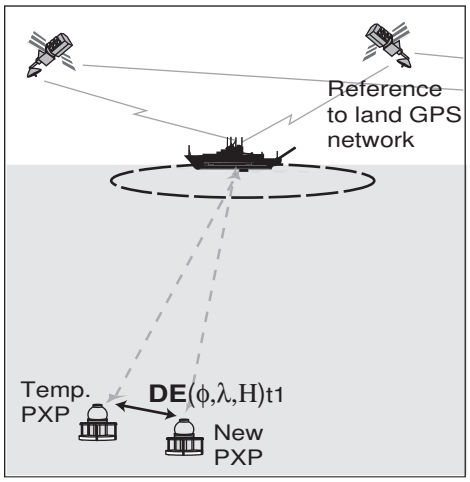

Figure IV.3: Dual transponder GPSA circle drive around a temporary and replacement transponder to orient the observation network in latitude, longitude and height and estimate $\mathbf{DE}t_1$ ($\sim$3 m), the baseline of the two active transponders. The depth of the transponders is on the order of km.

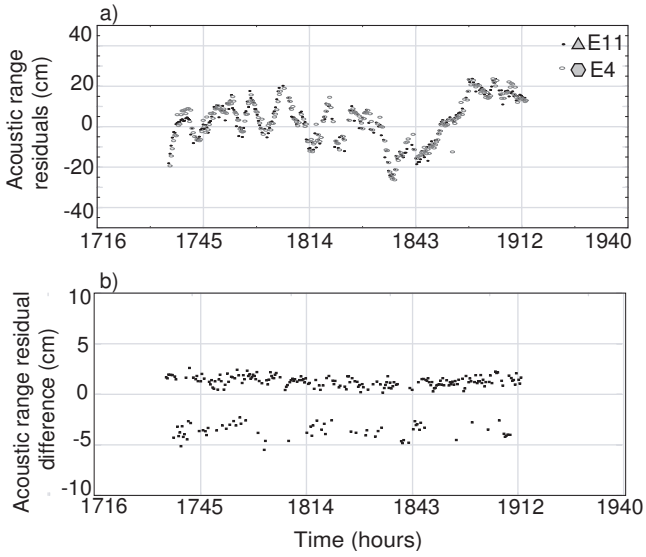

Figure IV.4: a) Acoustic range residuals for the dual transponder circle drive around PXP E11 (black) and E04 (gray). b) Acoustic range residual difference at each epoch. Occasional 5 cm offset due to improper peak selection during acoustic signal correlation.

$$\mathbf{O} = f(\mathbf{x}), \tag{IV.6}$$

$$\mathbf{c} = g(\mathbf{x}), \tag{IV.7}$$

where $f(\mathbf{x})$ are the functional relationships given in Section V.2 and $g(\mathbf{x})$ are the inner constraints. Inner constraints fix the net horizontal translation and azimuthal rotation of the network to zero (Leick, 2004). The remaining coordinate frame definitions, vertical translations, tilting of the horizontal plane and scale are controlled by the observations. The linear model is defined by

$$\mathbf{v}_o = \mathbf{A}\mathbf{x} + \mathbf{L}, \tag{IV.8}$$

$$\mathbf{v}_c = \mathbf{G}\mathbf{x} + \mathbf{C}, \tag{IV.9}$$

where $\mathbf{v}_o$ defines the residuals of the observations, $\mathbf{v}_c$ defines the residuals of the constraints, $\mathbf{A} = \delta f/\delta\mathbf{x}$ and $\mathbf{G} = \delta g/\delta\mathbf{x}$, evaluated at x. For the inner constraint solution, $\mathbf{C} = \mathbf{0}$ and the covariance matrix of the constraints, $\mathbf{\Sigma}_c = \mathbf{0}$. The non-unique matrix $\mathbf{E}^T$ (Leick, 2004) is introduced to form the null space of $\mathbf{A}$ such

Table IV.1: Observables and unknown parameters in the A/O least-squares adjustment.

Observables and 1-σ Uncertainty	Parameters
Camera Pitch (μ_{dcr}) $\pm 0.4^{\circ}$	Focal length
SSP depth (Z_{ssp}) ± 3 cm	Optical distance bias
Travel time (tt) ± 3 μs	Vertical angle bias
Sound speed (ss) ± 0.015 m/s	Temp. PXP time bias
Distance to the rng (d_{rng})	Repl. PXP time bias
Baseline $\mathbf{DE}_{t_1}$ ± 2.3 mm	ϕ, λ, H Repl. PXP, t_1
Initial position $(\phi, \lambda, H)_{Ct_0}$ ± 200 mm	ϕ, λ, H Temp. PXP, t_1
Transducer height pixels ($H_{dcr-pxl}$) ± 2 pxl	ϕ, λ, H SSP landings, t_1
Ring width pixels ($W_{rng-pxl}$) ± 1 pxl	

that

$$\mathbf{A}\mathbf{E}^T = \mathbf{0}. \tag{IV.10}$$

The corrections to the initial estimate of unknowns, $\mathbf{x}_o$, can be written as

$$\Delta\mathbf{x} = -\mathbf{Q}_{\Delta\mathbf{X}}\mathbf{A}^T\boldsymbol{\Sigma}_0^{-1}\mathbf{L}, \tag{IV.11}$$

where

$$\mathbf{Q}_{\Delta\mathbf{X}} = (\mathbf{A}^T\boldsymbol{\Sigma}_0^{-1}\mathbf{A} + \mathbf{E}^T\mathbf{E})^{-1} - \mathbf{E}^T(\mathbf{E}\mathbf{E}^T\mathbf{E}\mathbf{E}^T)^{-1}\mathbf{E}, \tag{IV.12}$$

and the covariance matrix of the adjusted parameters is

$$\boldsymbol{\Sigma}_x = \sigma_0^2\mathbf{Q}_{\Delta\mathbf{X}}. \tag{IV.13}$$

The new estimate of the unknown parameters can be written

$$\hat{\mathbf{x}} = \mathbf{x}_o + \Delta\mathbf{x}. \tag{IV.14}$$

The adjustment is reiterated until $\Delta\mathbf{x}$ is below a threshold, in this case 0.001 m. The observations are analyzed for outliers with Pope's method based on the Studentized residual, τ, and rejected if greater than a critical value, c, based on a risk level of $\alpha = 5\%$, or 95% confidence (Caspary, 1988; Leick, 2004).

A redundancy number (r_i) is calculated to investigate each observation's contribution to the redundancy of the model, i.e., the degrees of freedom. This value is defined by

$$r_i = q_i p_i (0 < r_i > 1), \tag{IV.15}$$

where q_i is the diagonal element of the cofactor matrix for the residuals ($\mathbf{Q}_v$), Leick04 and p_i is the weight of the i^{th} observation. The redundancy number exposes weak parts of the adjustment whereby if r_i nears 0, the observation is uniquely used in the solution and it does not increase the degrees of freedom ($\Sigma r_i = d.f.$). If r_i equals 1, the observation is redundant and increases the $d.f.$ by 1. Observations with a $r_i < 0.3$ should be avoided to ensure the model can identify when the observation is an outlier (Caspary, 1988). That threshold, i.e. each observation's maximum error that can be detected as an outlier is the marginally detectable blunder (mdb), ∇_i, and is defined as

$$\nabla_i = \frac{u_{\alpha,\beta}}{\sqrt{r_i}} \sigma_i, \tag{IV.16}$$

where $u_{\alpha,\beta}$ represents risk level, $\alpha = 5\%$, and probability of type II error, $\beta = 20\%$, Caspary88 and σ_i is observation uncertainty. A high mdb indicates an unreliable part of the network where the geometry or set of observations should be strengthened. The effect of each observation's mdb on the unknowns is

$$\nabla x_i = (\mathbf{A}^T \mathbf{\Sigma}_0^{-1} \mathbf{A})^{-1} \mathbf{A}^T \mathbf{\Sigma}_0^{-1} \nabla_i, \tag{IV.17}$$

which represent coordinate shifts to the survey package and transponder positions. The a priori variance of unit weight,

$$\hat{\sigma}_0^2 = \frac{\hat{\mathbf{v}}^T \mathbf{\Sigma}_0^{-1} \hat{\mathbf{v}}}{d.f.}, \tag{IV.18}$$

where $\hat{\mathbf{v}}$ is the residual matrix, is also sensitive to the mdbs. This value should converge to 1 if the model is consistent with the observations and their uncertainties.

Table IV.2: Acoustic/optical survey

No. observations	50
No. unknowns	32
No. iterations	5
$d.f.$	22
c	1.71
$\hat{\sigma}_o^2$ (Eqn IV.18)	0.31

Table IV.3: Output model parameters

Focal length dcr (m)	1697.240±49.810
Opt. dist. bias (E-5 units)	5.25±4.21
Vert. angle bias (dec. deg)	-2.51E-14±5.55E-9
Temp. PXP bias (sec)	1.43E-14±5.55E-9
Repl. PXP bias (sec)	-1.38E-14±5.55E-9

IV.1 Relocation results

Six survey landings were performed around the relocation site. The details of the acoustic/optical survey, including degrees of freedom ($d.f.$), corresponding critical value (c), and the aposteriori variance of unit weight ($\hat{\sigma}_o^2$) are shown in Table IV.2. The parameters of the adjustment, including focal length of the transducer and distance, angle and travel time biases are shown in Table IV.3.

Figure IV.5 shows each SSP landing, replacement, temporary and inactive transponders with 95% confidence ellipses and marginally detectable blunders for each observation. The uncertainty of the inactive-replacement transponder baseline is ±33 mm east, ±42 mm north and ±17 mm up ($\rho_{e,n} = 0.45$, $\rho_{e,u} = -0.01$, $\rho_{n,u} = -0.02$). The survey geometry produced a well constrained solution with only 3 optical ranges 4 vertical angles removed as outliers.

The uncertainty of the array position is a combination of the positional uncertainty of each transponder in the array. The uncertainty added by performing a relocation is dependent on the number of transponders in the array (N_{pxp}), their

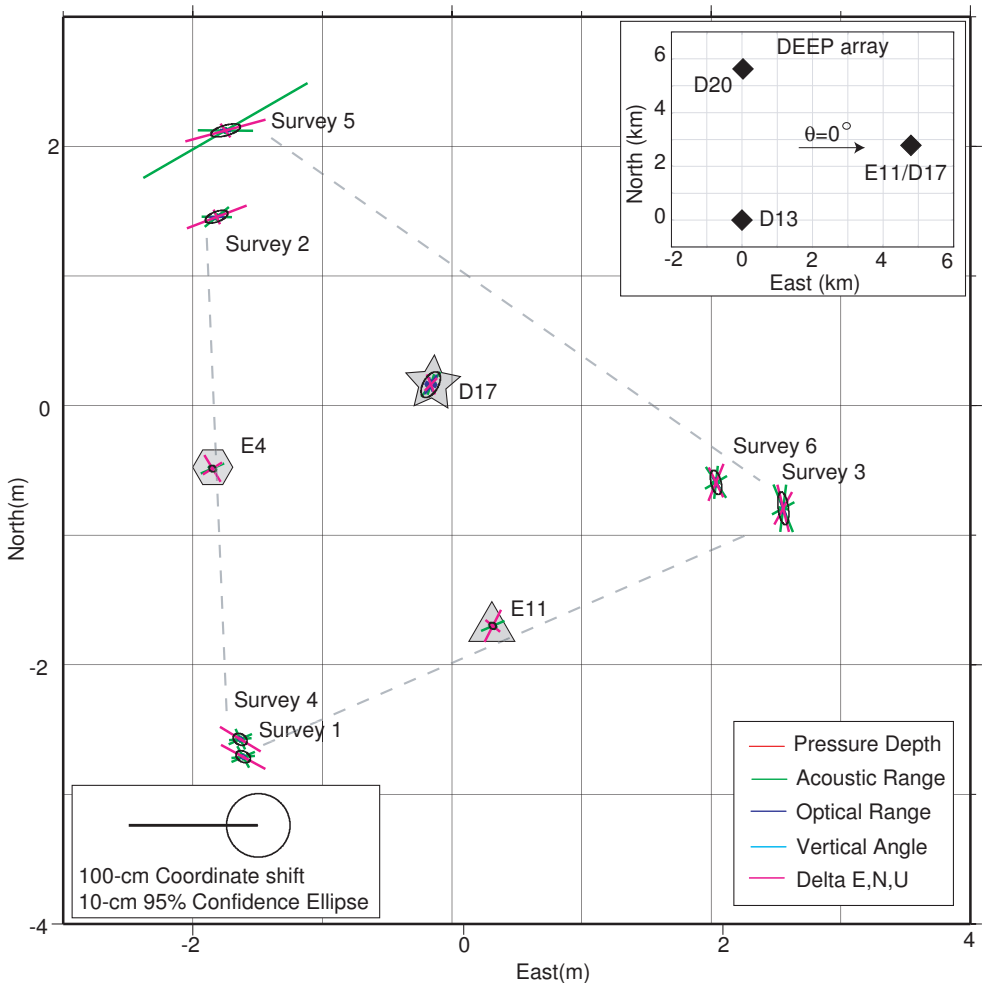

Figure IV.5: Plot of positional uncertainty (black ellipse) for each SSP landing, active transponders (E11, E4), and inactive transponder, D17. Black circles represent error ellipses with 95% confidence and colored lines represent marginally detectable blunders in each observation that was used in the adjustment. Dashed gray lines show the area inscribed by the survey landings. The orientation of the deep array is shown in the inset.

relative position, and the fit of the A/O survey observations in the least-squares adjustment. Since data is collected from the array center, the GPSA technique is most sensitive to positional shifts in the radial direction and insensitive to shifts in the tangential direction. The east and north uncertainty of $\mathbf{CD}_{t_1}$ is rotated into radial and tangential components using

$$\mathbf{\Sigma}_{r,\theta} = \mathbf{G}\mathbf{\Sigma}_{e,n}\mathbf{G}^T. \tag{IV.19}$$

The rotation matrix is defined by

$$\mathbf{G} = \begin{bmatrix} cos\ \theta & sin\ \theta \\ -sin\ \theta & cos\ \theta \end{bmatrix}, \tag{IV.20}$$

where θ is the angle between east and the replacement transponder, originating at the center of the array and positive counterclockwise. At the deep array, θ equals 0° and is indicated in Figure IV.5. The radial and tangential contribution to the positional uncertainty of the array, divided by the square root of N_{pxp}, is ±19 mm and ±24 mm, respectively. The contribution is included in the error analysis in Section III.2.

An additional component of the deep array solution is that PXP D17 became inactive prior to a GPSA survey in 2001. Therefore the initial position of PXP D17 ($D17_{to}$) was unknown. The position of D17 in the final epoch, $D17_{ti}(a)$, was roughly estimated from a down-looking screen capture from the CV showing both D17 and E11. The first iteration of the relocation least-squares adjustment provided the east, north and up offset $[CD_{ti}(a)]$ and a new E11 position, $E11_{ti}a$. A new absolute position of D17, $D17_{ti}(b)$ could be calculated using this offset,

$$D17_{ti}(b) = E11_{circ} + CD_{ti}(a), \tag{IV.21}$$

where $E11_{circ}$ is the position of PXP E11 from the circle drive in final epoch. The adjustment was performed again with $D17_{ti}(b)$ in order to provide a new position for E11, $E11_{ti}(b)$, which we expect to be equivalent to $E11_{circ}$. The offset from the second iteration of the adjustment, $CD_{ti}(b)$, was used to calculate the final

position for D17,

$$D17_{ti}(c) = E11_{circ} + CD_{ti}(b). \tag{IV.22}$$

The offset between the live/inactive transponders from the adjustment is not sensitive to the initial position of the inactive transponder. If the calculation for the D17-E11 offset was consistent from one iteration of the adjustment to the next, we would expect that,

$$D17_{ti}(b) \simeq D17_{ti}(c), \tag{IV.23}$$

and

$$E11_{circ} \simeq E11_{ti}(b). \tag{IV.24}$$

The difference for the relationships in Equation IV.23 and Equation IV.24 were less than 1 mm. The a priori position in the GPSA least-squares adjustment at the deep array was $D17_{ti}(c)$, from Equation IV.22, in 2001 and $E11_{circ}$ in 2003. The resulting array motion is represented by

$$\mathbf{P} = -(\frac{\mathbf{A} + \mathbf{B} + \mathbf{C}}{3}), \tag{IV.25}$$

where A, B and C represent transponders D13, D20 and D17. The scenarios for calculating plate motion with a relocation are shown in Figure IV.6. The special case where no initial circle drive is performed is shown in Figure IV.6c.

IV.2 Relocation simulation

A simulation was performed to decrease the transponder relocation's contribution to the array positional uncertainty. The uncertainty of the relocation, or more specifically the uncertainty of the baseline between the inactive and replacement transponders, depends on the geometry of the survey observations. The strongest observation in the A/O survey is the temporary-replacement transponder baseline ($\mathbf{DE}_{t_1}$) with the dual transponder circle drive. To strengthen the geometry of the network, the temporary and replacement transponders should be placed on either side of the inactive transponder to provide both orientation and a scale

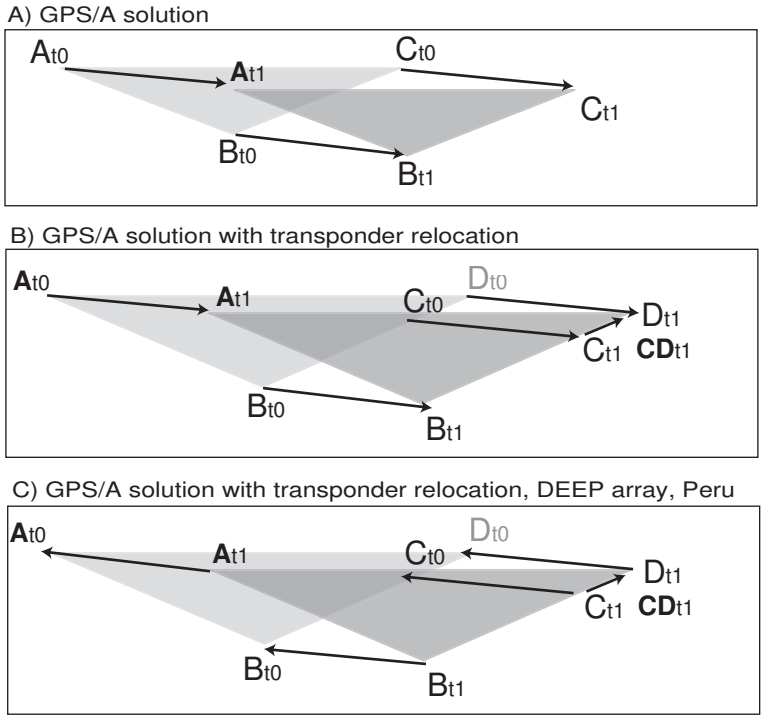

Figure IV.6: GPSA solution for plate motion with (A) no transponder relocation, (B) transponder relocation and (C) transponder relocation with no initial survey of the inactive transponder.

measurement that constrains $\mathbf{CD}_{t_1}$ inside of $\mathbf{DE}_{t_1}$. A network with this geometry is shown in Figure IV.7. It was also seen in Section IV.1 that the SSP-active transponder acoustic travel times have a low uncertainty while the optical observations have the highest. To enhance the strength of the acoustic measurements, 4 survey landings would better constrain the SSP and active transponder positions. A simulation was performed using this geometry and varying the A/O survey input within the standard deviation of each observation (Gagnon and Chadwell, 2007). The uncertainty of $\mathbf{CD}_{t_1}$ was roughly ± 15 mm east and north. Assuming an array of 4 transponders where $\theta = 45°$, the uncertainty added to the array position is ± 10 mm, compared to the previous average of ± 26 mm. Future relocation surveys should be performed with the simulation geometry in order to decrease the contribution to array positional uncertainty.

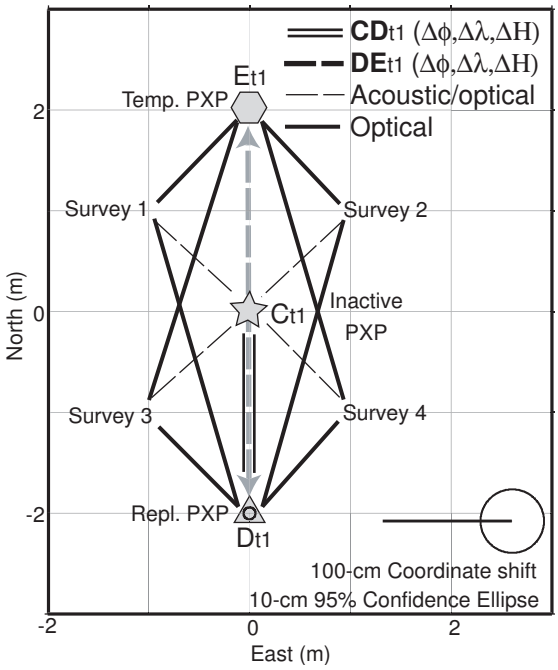

Figure IV.7: Network simulation to better constrain the uncertainty of the replacement-inactive transponder baseline, $\mathbf{CD}_{t_1}$.

V

Related Work

This section includes results related to the GPS-acoustic investigation at the Peruvian margin. First, a simulation of kinematic GPS over long baselines (100 km) is shown to have an uncertainty of 2-4 mm. This value is necessary in order to appropriately scale the GPS contribution to array vector uncertainty. Next, three methods for investigating vertical transponder displacement are discussed. The results help resolve the internal rigidity of each array. Finally, acoustic data from towed-interrogator surveys were also collected to help determine rigidity of the arrays. These data are presented though results are inconclusive.

V.1 Long-baseline kinematic GPS

GPS antenna baselines rely on a double difference phase observable to cancel clock errors and hardware delays. Lengthening the antenna baseline decreases the accuracy of this assumption. The repeatability of the kinematic solution over baselines of roughly 150 km was investigated by using the high rate coastal stations at Salinas (SALI), Pucusana (PUCU) and Molina (MOLI). Each receiver operated for the duration of the seagoing expedition in 2001, collecting roughly 300 hours of data. The position of SALI was determined both statically and kinematically, first using only PUCU, then both MOLI and PUCU. Figure

V.1 shows the baselines between the coastal GPS stations and offshore GPSA sites. The baselines from SALI-PUCU and MOLI-PUCU are similar in magnitude to the baseline from the coastal stations to the deep and shallow seafloor geodesy sites. Although GPS processing software provides an error factor, representing the misfit of the data for each station, this test can be used to scale positional uncertainty as a result of long antenna baselines.

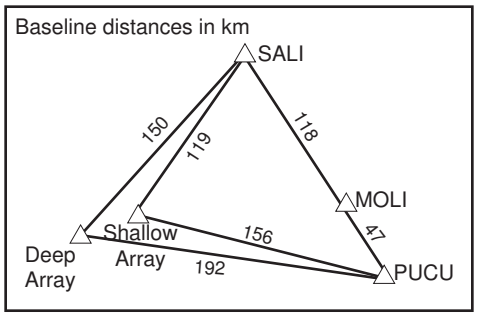

Figure V.1: Baseline lengths (km) for coastal, campaign GPS stations at Molina (MOLI), Pucusana (PUCU), and Salinas (SALI) and deep and shallow seafloor geodesy arrays.

Four geodetic solutions were performed with GIPSY-OASIS II. Static solutions were performed by first holding PUCU, then PUCU and MOLI fixed and estimating the position of SALI. Next, kinematic solutions were performed, again holding first PUCU, then PUCU and MOLI fixed and estimating the position of the SALI. The kinematic estimation for SALI was compared to the static holding just PUCU fixed (Figure V.2a). The difference varies on the order of centimeters. There is also a larger average difference in the north-south component than in the east-west. Due to the roughly north-south geometry of the stations, we expect the north-south component to have a higher uncertainty. This aspect of the test is also appropriate for the seafloor sites in that they are perpendicular to the coast, with a likely higher uncertainty in the east-west component. Fixing MOLI and PUCU, the kinematic-static comparison of SALI's position reduces to millimeters, Figure V.2c. The east and north residuals are also balanced when adding the extra station.

The positional uncertainty (1-σ) of the kinematic test is shown in Figure V.2b,d. A diurnal cycle of solar heating, or electron density in the ionosphere, is seen between peaks of the residuals. The average uncertainty for the kinematic solution is ±3.6 cm east and ±9.7 cm north, decreasing to ±1.8 cm east and ±4.2 cm north when MOLI is added to the solution. Again, the directionality of the solution causes a greater average residual in the northward direction.

The uncertainty is a function of the geometric strength and number of GPS stations as well as the length of the station baselines. The added uncertainty in the absolute position for a kinematic solution over the roughly 150 km long baseline to the shallow and deep array positions will be on the order of 2-4 cm. This is in agreement with other long-baseline kinematic simulations, (Jr. et al., 1993; Miura et al., 2002).

V.2 Transponder Depth

A rigid array is necessary for the GPSA technique to accurately measure horizontal plate motion. As discussed in Section II, plate motion is represented by the average displacement of each transponder. Vertical displacement of individual transponders between campaigns will translate to erroneous horizontal array motion in the acoustic travel time solution. This is caused by non-uniform shortening or lengthening of acoustic travel times. The depth of each transponder was measured in each epoch to ensure rigidity of the array's internal geometry. Three techniques for measuring transponder depth are discussed below: a moving GPSA survey, a timed-release pressure gauge and the acoustic/optical survey. This is followed by depth results in 2001 and 2003 at the shallow and deep array.

V.2.A Depth measurement techniques

The first method included driving a 1-nm radius circle around each transponder as discussed in Section II.4.A. The depth was estimated with a repeatability

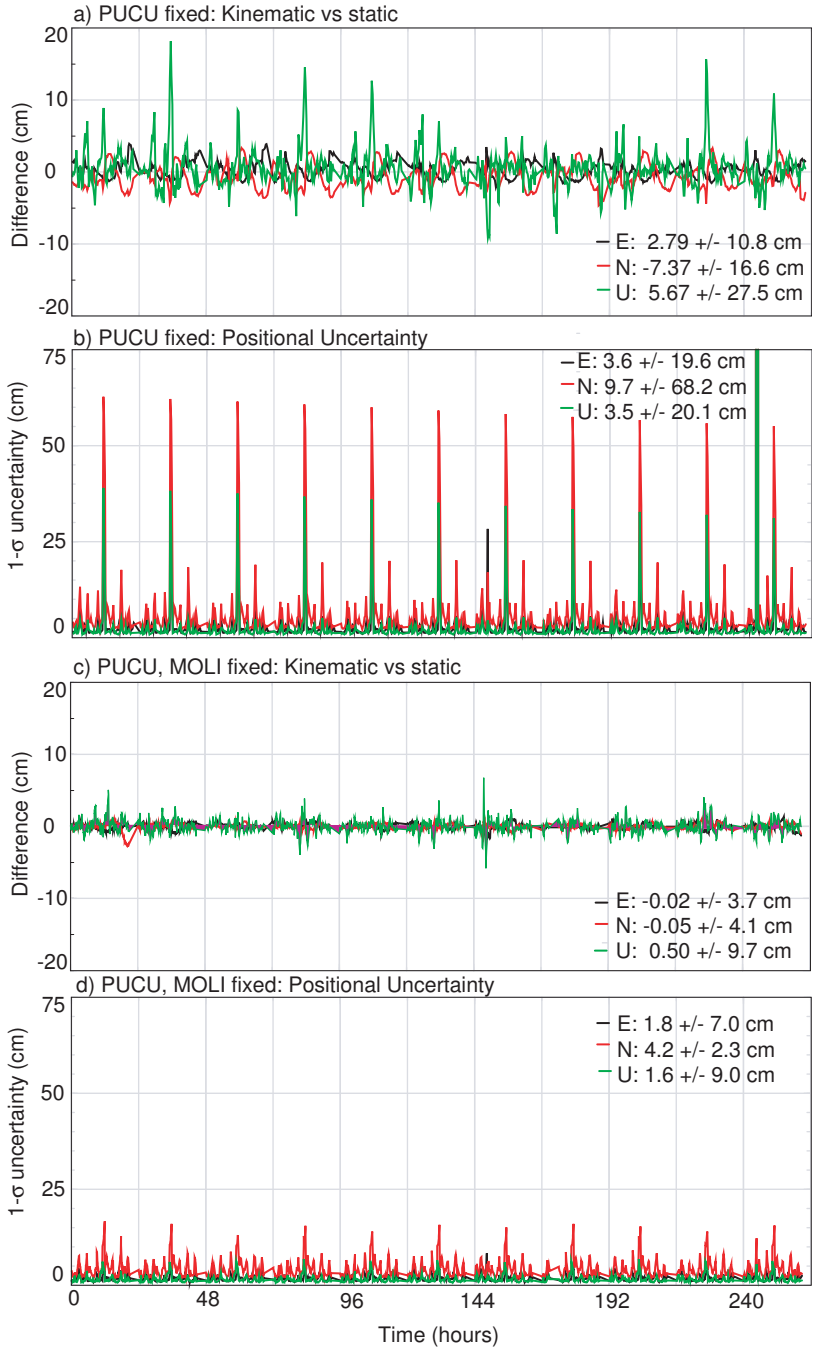

Figure V.2: a) Fixing only PUCU, difference between kinematic and static solution for SALI in east (black), north (red) and up (green) components. b) Fixing only PUCU, east (black), north (red) and up (green) positional uncertainty for SALI from the kinematic solution. c) Fixing PUCU and MOLI, difference between kinematic and static solution for SALI in east, north and up components. b) Fixing PUCU and MOLI, east, north and up positional uncertainty for SALI from the kinematic solution.

of 1 m. The large uncertainty is due to a weak geometry of survey points several kilometers above the transponder and sound speed fluctuations, which can shift the vertical solution by tens of centimeters.

A second method, independent of the GPS-acoustic solution, was attaching a timed-release pressure gauge to the transponder frame. The pressure gauge (dropper) was fastened with a mechanical release before instrument deployment. Roughly 13 hours of data were gathered before recovery. The depth of the transponder was calculated by converting pressure to depth, accounting for the tidal variation, inverse barometer effect, fresh to salt water conversion and geopotential anomaly.

The final method was the acoustic/optical (A/O) survey performed with the Marine Physical Lab Control Vehicle (CV) and a seafloor survey package (SSP) shown in Figure V.3. The CV is equipped with lateral thrusters, a pressure gauge, bottom looking hydrophone and a down looking camera (Figure V.3b) while the SSP carries 4 Paroscientific Digiquartz pressure gauges, a temperature sensor, conductivity sensor, tilt-meter, a side-facing transducer and a camera with surface controlled pan and tilt (Figure V.3c). After sufficient temperature sensor equilibration within 100 meters of the seafloor, the SSP is placed on the seafloor at three sites within 2 meters of the transponders such that each transponder is clearly visible. The pan and tilt video camera captures painted scale lines on the PXP transducer and opposite edges of the 1-m-diameter metal ring encompassing the PXP. Optical ranges are calculated later from the stored digital image by counting pixels of predetermined lengths on the PXP frame. The SSP transducer interrogates the two active transponders, once every 10 seconds, providing 10-20 travel times during each, roughly 2 minute survey. The range is calculated using the sound speed profile discussed above, extrapolated to the depth of the transponders. The SSP pressure record is averaged between the 4 pressure gauges and corrected for the ocean surface tidal signal, water column density, and atmospheric pressure.

The transponder package consists of a circular metal frame around a

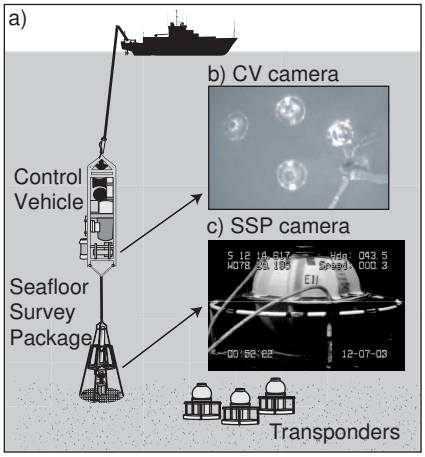

Figure V.3: a) Cartoon of the acoustic/optical survey with the ship, control vehicle (CV), seafloor survey package (SSP) and seafloor transponders (PXP). b) Digital image from the CV's down-looking camera illuminating the survey package, tethered below the CV, and the replacement, temporary and inactive transponders. c) Digital image from the survey camera looking toward a transponder on the seafloor.

pressure-resistant glass sphere housing the electronics and a cylindrical transducer at the top. The depth of the PXP transducer is calculated from the depth of the survey package's pressure case, Z_{ssp}, plus or minus a depth offset, Z_{off}, from the survey camera to the PXP transducer. Calculating Z_{off} requires measurement of the slant distance to the PXP. There are three methods to determine the slant distance; optical sighting to either the transducer or frame-ring and acoustic ranging to the active PXP transducer. As mentioned, acoustic ranges are taken to the two active transponders, while optical sightings are taken to all three transponders. The preferred optical target is the ring, which is $\sim$1 m wide and is more precise than sighting the transducer, $\sim$0.025 m tall. The latter is only used if the ring sighting is obscured. The observables and uncertainties collected during the survey are shown in Table V.1 and Figure V.4. For the optical measurement of the ring (Figure V.4a) the law of similar triangles allows the range from the camera to the opposite edges of the ring to be written as

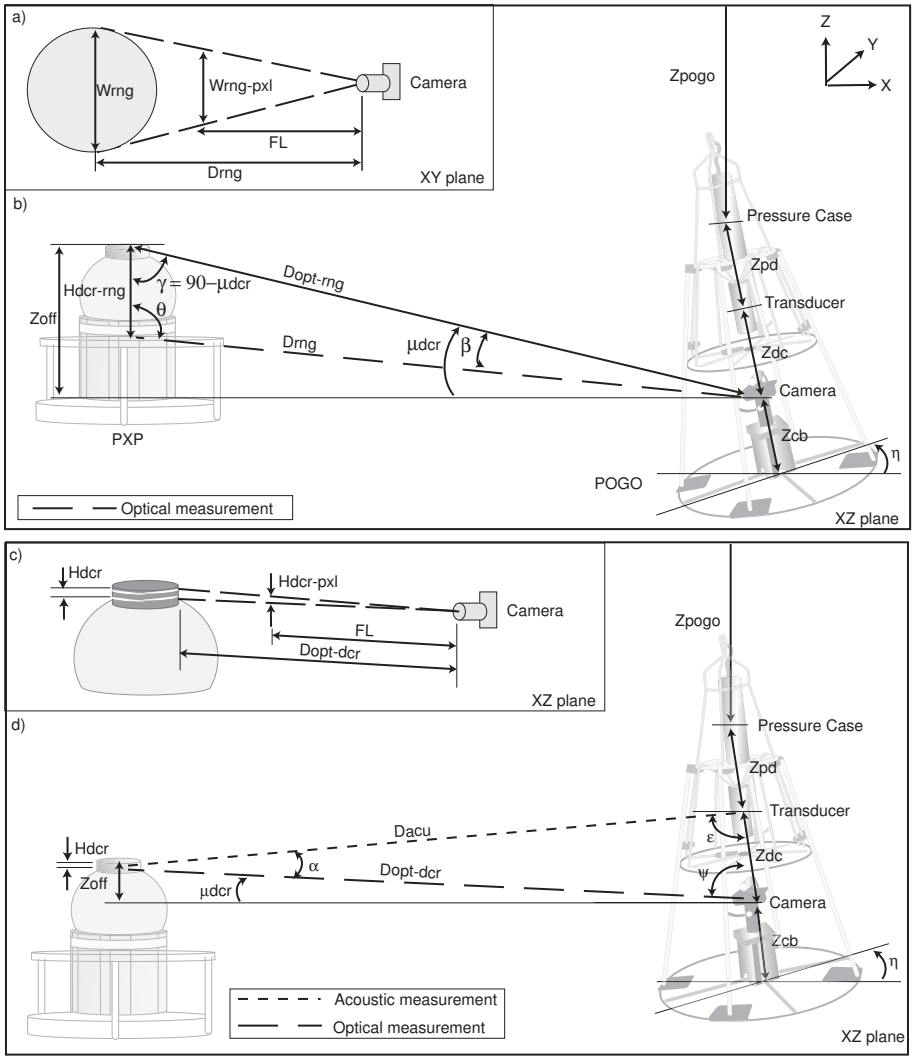

Figure V.4: a) Relating the optical range from the survey package camera to the ring, D_{rng}, and the focal length of the camera, FL. b) Measuring the depth of the PXP transducer from sighting the PXP metal frame (ring). c) Relating the optical range from the camera to the transducer, $D_{opt-dcr}$, and the focal length of the camera, FL. d) Measuring the depth of the PXP transducer from sighting the PXP transducer or using the acoustic range.

Table V.1: Observables in the A/O survey for transponder depth.

Observables	1-σ Uncertainty
Camera pitch to PXP transducer (μ_{dcr})	$\pm 0.4^{\circ}$
SSP depth (Z_{ssp})	± 3 cm
Travel time (tt)	± 3 μs
Sound speed (ss)	± 0.015 m/s
SSP X-plane tilt (η_x)	$\pm 0.5^{\circ}$
SSP Y-plane tilt (η_y)	$\pm 0.5^{\circ}$
Transducer height pixel count ($H_{dcr-pxl}$)	± 2 pixels
Ring width pixel count ($W_{rng-pxl}$)	± 1 pixel

$$D_{rng} = \frac{FL * W_{rng}}{W_{rng-pxl}}, \tag{V.1}$$

where W_{rng} was measured prior to deployment, $W_{rng-pxl}$ is from the digital image and FL is the camera's focal length, determined by self-calibration. From Figure V.4b, let γ be defined as

$$\gamma = 90^{\circ} - \mu_{dcr}, \tag{V.2}$$

where μ_{dcr} is the pitch of the camera measured with an onboard tilt sensor. Using the law of sines in the triangle with angles θ, β, γ,

$$\beta = \arcsin[\frac{H_{dcr-rng} \sin\gamma}{D_{rng}}], \tag{V.3}$$

and the range to the PXP transducer is

$$D_{opt-rng} = \frac{D_{rng} \sin\theta}{\sin\gamma}, \tag{V.4}$$

Figure V.4c shows the relationship between the transducer height, h_{dcr} and the focal length of the camera such that

$$D_{opt-dcr} = \frac{FL * h_{dcr}}{h_{dcr-pxl}}. \tag{V.5}$$

where

$$\theta = 180^{\circ} - \beta - \gamma. \tag{V.6}$$

The depth offset from the camera to the transducer is

$$Z_{off} = D_{opt-rng} \sin \mu_{dcr}. \tag{V.7}$$

The final depth of the PXP transducer from the ring sighting, incorporating the tilt of the survey package frame, η, is

$$Z_{pxp}^{opt-rng} = Z_{ssp} + (z_{pd} + z_{dc})cos\eta - Z_{off}, \tag{V.8}$$

where the height from the midpoint of the SSP pressure case to the SSP transducer, Z_{pd}, and the height from the SSP transducer to the camera, Z_{dc}, are measured prior to deployment.

For the optical measurement of the transducer (Figure V.4c) the relationship between the transducer height, H_{dcr}, and the focal length of the camera is

$$D_{opt-dcr} = \frac{FL * H_{dcr}}{H_{dcr-pxl}}, \tag{V.9}$$

where H_{dcr} was measured prior to deployment and $H_{dcr-pxl}$ is from the digital image. The height between the PXP transducer and survey package camera from Figure V.4d is

$$Z_{off} = D_{opt-dcr} \sin \mu_{dcr}, \tag{V.10}$$

and the final depth of the PXP transducer using the transducer sighting is

$$Z_{pxp}^{opt-dcr} = Z_{ssp} + (z_{pd} + z_{dc})cos\eta - Z_{off}. \tag{V.11}$$

The depth of active transponders can be determined using the acoustic range, D_{acu}, shown in Figure V.4d. The acoustic-based depth calculation is more accurate than the optical due to the higher uncertainty in counting pixels. The range of the acoustic signal is,

$$D_{acu} = tt\frac{ss}{2}, \tag{V.12}$$

where tt is the two-way or round trip travel time from the SSP to the PXP transducer and ss is the sound speed. Let ψ be defined as

$$\psi = 90^{\circ} - \mu_{dcr} - \eta. \tag{V.13}$$

Using the law of sines in the triangle with angles α, ϵ, ψ,

$$\alpha = \arcsin(z_{dc}\frac{\sin\psi}{D_{acu}}), \tag{V.14}$$

and

$$D_{opt-dcr} = \frac{\sin\epsilon}{\sin\psi}D_{acu}, \tag{V.15}$$

where

$$\epsilon = 180^{\circ} - \alpha - \psi. \tag{V.16}$$

The depth offset from the camera to the PXP transducer is

$$Z_{off} = D_{opt-dcr}\sin\mu_{dcr}, \tag{V.17}$$

and the final PXP depth using the acoustic signal is

$$Z_{pxp}^{acu} = Z_{ssp} + (z_{pd} + z_{dc})cos\eta - Z_{off}. \tag{V.18}$$

The results of transponder depth measurements are shown in Table V.2. The methods of depth measurement are compared by normalizing to one depth, in this case, the dropper depth in 2001 (D01). The last row of the table shows the average depth difference for each method. The circle drive and array center solutions exhibit systematic biases; the depth is consistently 1-2 m deeper than the dropper in both epochs.

V.2.B Depth results

The internal rigidity of the array was investigated by first calculating the depth difference between transponder pairs in each epoch (Z_{pxp}). Next, the relative depth difference was compared from one epoch to the next ($\Delta Z_{pxp\Delta t}$), shown in Table V.3. This calculation helps eliminate systematic errors in the seafloor depth survey technique. The average depth difference, compared from 2001 to 2003 is $\pm$5.3 cm (P03-D01) and $\pm$14.9 cm (P03-P01). A significant change in relative depth is indicated at PXP D14 in the seafloor survey 2003 versus seafloor survey

Table V.2: Transponder depths normalized to 2001 dropper (P01) depth measurement. P=seafloor survey, C=circle drive, A=array center solution. * denotes 2003 seafloor survey depth for PXP E11.

PXP	Z_{pxp}^{D01}	ΔZ_{pxp}^{P01}	ΔZ_{pxp}^{C01}	ΔZ_{pxp}^{A01}	ΔZ_{pxp}^{P03}	ΔZ_{pxp}^{C03}	ΔZ_{pxp}^{A03}
D13	3209.196	-0.402	-1.744	-2.124	-0.430	-1.879	-2.280
D17	3209.434	-0.451	n/a	-2.090	n/a	n/a	n/a
E11	3209.256*	n/a	n/a	n/a	0.000	-1.814	-1.849
D20	3201.788	-0.392	-1.631	-2.171	-0.478	-1.678	-2.327
D14	2113.220	-0.137	-1.189	-1.850	-0.605	-2.136	-1.847
D16	2076.215	-0.366	-1.476	-1.758	-0.535	-2.157	-1.755
D18	2108.317	-0.392	-1.291	-1.724	-0.572	-1.942	-1.720
AVG	–	-0.357	-1.466	-1.953	-0.501	-1.958	-1.986

2001 comparison (column 3), which is not seen in the seafloor survey 2003 versus dropper 2001 calculation (column 4). This discrepancy will be further investigated below. Using the P03-D01 measurement (column 3), the change in baseline depth difference ranges from 3.2±3 - 8.0±3 cm. (The repeatability of the relative depth calculation (±3 cm) is the product of seafloor depth surveys at various GPS-acoustic sites.)

Table V.3: Change in transponder baseline depth difference between seafloor survey 2003 and seafloor survey/dropper 2001.

Array	Baseline	Baseline depth difference	
		$\Delta Z_{pxp\Delta t}^{P03-D01}$ (cm)	$\Delta Z_{pxp\Delta t}^{P03-P01}$ (cm)
DEEP	D20:D13	4.8	5.9
DEEP	D13:D17	3.2	8.0
DEEP	D17:D20	-8.0	-13.9
SHAL	D18:D14	3.3	*28.9*
SHAL	D14:D16	-8.0	*-30.8*
SHAL	D16:D18	4.7	2.0
RMS		±5.3	±14.9

Closing the survey loop is a technique used to gauge repeatability whereby the first survey is repeated at the end. Investigating the loop closures (Z_{pxp}^{lc}), it is apparent that there was a systematic bias in the 2001 seafloor survey observations

at the shallow array. At the shallow array in 2001, the temperature and pressure gauges were not sufficiently equilibrated before observations began. Gauge equilibration to several kilometers depth can take upwards of 4 hours. The first survey at the shallow array was PXP D18, followed by D16, D14 and then D18 again. The depth difference at D18 was 18 cm (Table V.4). The remaining five loop closures average 3.5 cm. The shallow array seafloor surveys in 2001 should not be used as an indicator of vertical displacements since the gauges were not fully equilibrated during the surveys. Improper gauge equilibration is partially the cause of large relative depth differences at PXP D14 in Table V.3.

Table V.4: Depth measurement repeatability or loop closure, ΔZ^{lc}_{pxp}

Array	Epoch	PXP	ΔZ^{lc}_{pxp} (cm)
DEEP	2001	D18	5.6
SHAL	2001	D18	18.4
DEEP	2003	E11	1.8
DEEP	2003	E04	1.5
DEEP	2003	D17	1.7
SHAL	2003	D20	6.7
RMS			$\pm$3.5 (excl. SHAL 2001)

In 2004, the SSP pressure gauges were calibrated for systematic bias due to tilt (ν). It was found that tilting the quartz crystal resonators inside each pressure gauge with respect to the water column could offset the pressure measurement as much as $\pm$25 cm. An algorithm was created from laboratory experiments where the SSP frame was tilted in a fixed pressure environment. The pressure and temperature periods of each pressure gauge were recorded. The offset from fixed pressure was accounted for with a pressure correction coefficient. Finally, the correction for each gauge was interpolated at intermediate tilts. Table V.5 shows the average, minimum and maximum tilt at each PXP site in 2001 and 2003. Using the pressure correction for tilt, we expect to decrease the range (Θ) of three SSP depths (Z_{ssp}) at each transponder as well as PXP reduced depths (Z_{pxp}). Table V.6 shows the ranges before (ΘZ_{ssp}, ΘZ_{pxp}) and after ($\Theta Z_{ssp}{}'$, $\Theta Z_{pxp}{}'$) the

Table V.5: Average, minimum and maximum seafloor survey package tilt (°) at each epoch.

Array	PXP	2001			2003		
		ν_{avg}	ν_{min}	ν_{max}	ν_{avg}	ν_{min}	ν_{max}
DEEP	E11	-	-	-	1.8	0.6	5.3
DEEP	D17	1.4	0.6	2.5	-	-	-
DEEP	D20	2.2	0.2	4.5	1.6	0.2	4.5
DEEP	D13	1.5	0.6	2.9	2.3	0.6	3.7
SHAL	D18	1.7	0.2	4.9	2.4	0.2	4.1
SHAL	D16	1.2	0.6	1.8	2.0	0.6	4.1
SHAL	D14	4.1	0.2	7.3	4.1	1.8	9.2

pressure correction. The right two columns show the change in spread as a result of the correction. The final two rows show the RMS averages.

The pre-correction spread is greatest at sites with large slopes, particularly D14 (66.4 cm spread in 2001), D20 (21.9 cm spread in 2001) and the relocation site with D17, E11 and E04 ($\sim$10 cm spread in 2003). Post-correction, the spread in 2001 decreased by an average 1.4 cm for SSP depths and 1.7 cm for transponder depths. Significant improvements are seen at PXPs D14 and D20, where the spread decreased by 14.5 cm and 4.9 cm, respectively. Conversely, the correction did not decrease the spread of the 2003 depth data. The spread of SSP depths decreased by an average 0.1 cm and transponder depths increased by an average 0.5 cm. A possible change in gauge orientation may render the correction algorithm inappropriate for the 2003 data.

In conclusion, the most reliable depth measurements are from the dropper in 2001 and seafloor survey package in 2003. Relative transponder depths did not change more than an average $\pm$5.3 cm over the two years of data collection. These small vertical displacements demonstrate sufficient array rigidity. The pressure correction for tilt decreased the spread of depth data in 2001 though did not benefit the observations in 2003. Two possible causes for error, which must be taken into account in future surveys, is insufficient time for gauge equilibration

Table V.6: Spread (Θ) of SSP and PXP depth measurements in cm, before and after (') pressure correction for tilt followed by difference

Epoch	PXP	Pre-corr. spread		Post-corr. spread		Change	
		ΘZ_{ssp}	ΘZ_{pxp}	ΘZ_{ssp}'	ΘZ_{pxp}'	$\Delta\Theta Z_{ssp}$	$\Delta\Theta Z_{pxp}$
2001	D18	5.3	3.1	3.2	1.3	2.1	1.8
2001	D18	5.2	5.1	2.9	8.9	2.3	-3.8
2001	D16	3.4	3.9	3.0	3.8	0.4	0.1
2001	D14	66.4	17.4	52.6	2.9	13.8	14.5
2001	D20	18.0	6.4	18.9	1.5	-0.9	4.9
2001	D20	21.9	3.6	23.9	5.4	-2.0	-1.8
2001	D17	5.8	11.9	8.5	11.8	-2.7	0.1
2001	D13	12.9	10.4	15.2	12.4	-2.3	-2.0
2003	D18	1.3	2.0	2.8	3.5	1.5	1.5
2003	D18	3.3	1.9	4.6	2.7	1.3	0.8
2003	D16	2.0	2.6	3.3	3.9	1.3	1.3
2003	D14	62.8	9.6	59.4	14.2	-3.4	4.6
2003	D20	14.0	7.0	13.8	8.0	-0.2	1.0
2003	D17	9.8	5.2	9.6	5.4	-0.2	0.2
2003	D17	9.9	3.9	10.0	3.3	0.1	-0.6
2003	E11	9.8	3.1	9.6	4.7	-0.2	1.6
2003	E11	9.9	7.4	10	6.9	0.1	-0.5
2003	E04	9.8	7.5	9.6	5.7	-0.2	-1.8
2003	E04	9.9	3.6	10.0	4.2	0.1	0.6
2003	D13	9.8	0.7	10.2	0.4	0.4	-0.3
RMS 2001		17.4	7.7	16.0	6.0	-1.4	-1.7
RMS 2003		12.7	4.5	12.6	5.0	0.1	+0.5

and an unknown orientation of the survey package pressure gauges. The latter does not allow correction for tilt, which was shown to have a large impact on transponder depth measurements at sites with slopes greater than 7°.

V.3 Near-bottom Acoustic Survey

Acoustic measurements from a towed interrogator can be used to calculate the relative positions of seafloor transponders with a repeatability of ±20 mm (Sweeney et al., 2005). The near bottom survey utilizes a towed remotely operated vehicle, in this case the seafloor survey package (SSP), to interrogate the transponders from roughly 100 m above the seafloor. The interrogator records the hydrostatic pressure each second with four pressure sensors while interrogating the transponders every 20 seconds. A least-squares adjustment with a minimum of three acoustic travel times, SSP depth and a priori latitude, longitude and height of each transponder provides the relative transponder positions. The near bottom survey takes advantage of stable sound speeds at depths greater than 2 km. Section II.3 included sound speed measurements that varied ±0.1 m/s on the order of years.

Two-way, SSP-PXP travel times are shown in Figure V.5a and b. A solution for the survey tow track is shown in Figure V.5c and d. No solution was obtained at the shallow array in 2003 due to insufficient data coverage. The data at the deep array are inconclusive due to poor survey geometry resulting from time limitations for data collection. Despite the sparseness of data, valuable information was gained on using the survey package as a towed interrogator.

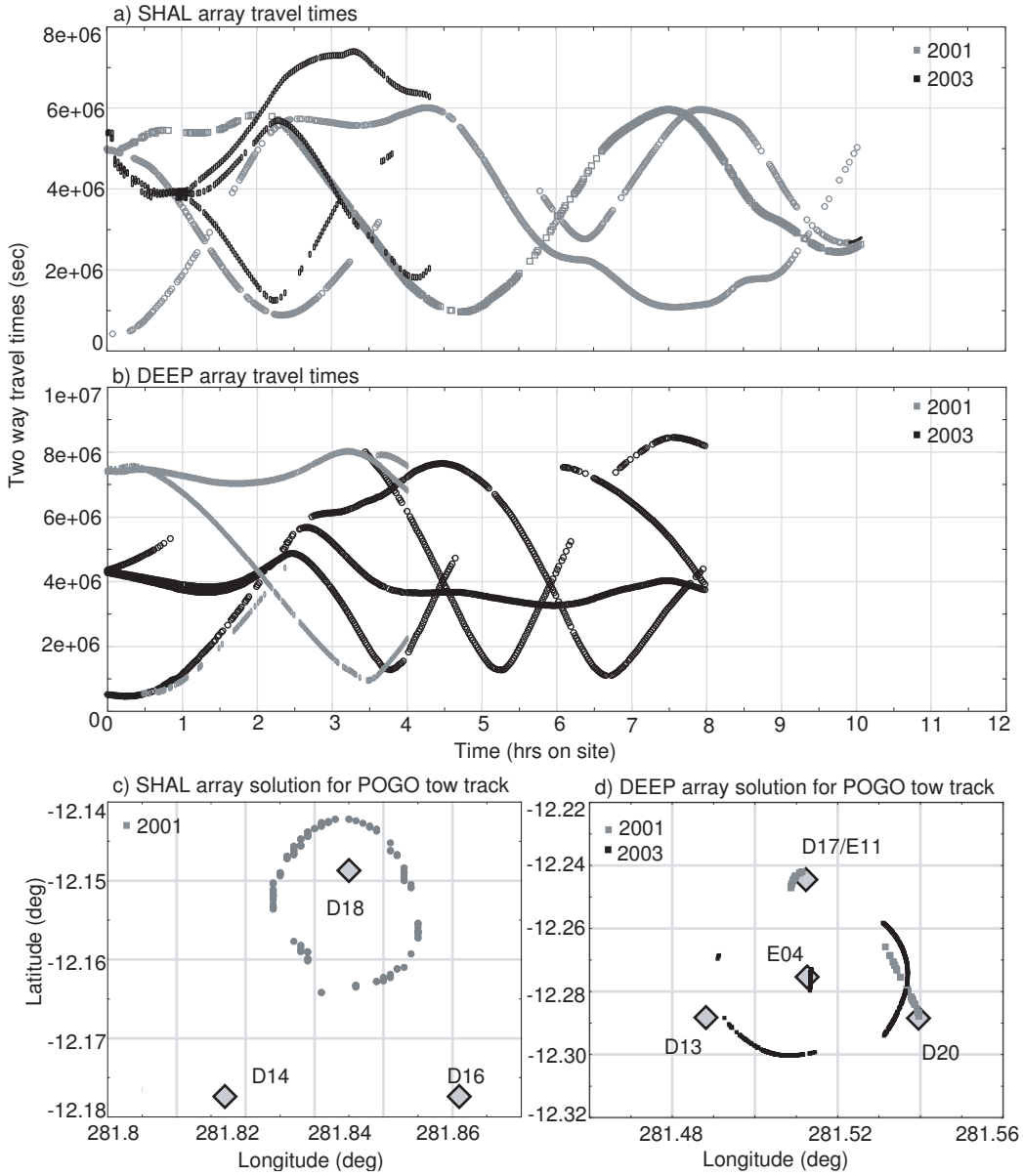

Figure V.5: a) Shallow array SSP-PXP acoustic travel times during near bottom survey in 2001 (gray) and 2003 (black). b) Deep array SSP-PXP acoustic travel times during near bottom survey in 2001 (gray) and 2003 (black). c) Survey tow track solution from least-squares adjustment at the shallow array, 2001. d) Survey tow track solution from least-squares adjustment at the deep array, 2001 and 2003.

VI

Conclusions

The GPSA technique was used to measure horizontal deformation above the thrust fault between the oceanic Nazca and continental South America plates. Three dimensional elastic half-space models showed an agreement between horizontal displacement measurements 20 and 50 km landward from the trench axis and shallow coupling between 2001 and 2003. The GPS-acoustic technique was used to provide the one of the first seafloor geodetic measurements of plate convergence. These data complete a chain of geodetic measurements across the plate boundary: from near the trench axis offshore Peru to the stable cratonic interior of South America. Several conclusions can be drawn about the development of the GPSA technique and about the geophysical significance of these observations.

VI.1 GPS-Acoustic and related techniques

This work includes a detailed analysis of the GPS-acoustic technique as it was used at the Peruvian margin to measure seafloor horizontal deformation. At the time of this work, less than five successful, indirect-path seafloor geodesy campaigns have been conducted in the world. Each development, in terms of equipment and methods of data collection and analysis, lends to the future success of this technologically challenging field. The components of the GPSA technique

were presented separately. Beginning with GPS and sea surface height, kinematic GPS residuals ranged from 1-2 mm with a 24-hour cycle in peak residuals due to the diurnal cycle of solar heating. Heading was also held with dynamic positioning such that antenna phase wrap did not introduce a bias in the kinematic GPS solution. The ability of kinematic GPS to model sea surface height as predicted by tide models averaged 0.4-1.7 cm, while the tide gauge and tide model agreed to 0.1 cm. Next, daily shipboard surveys of the GPS antenna-hydrophone baseline were shown with average residuals ±4.7 mm. The average difference between antenna baselines determined with GPS versus the shipboard survey averaged -10±40 mm. The negative average presents an unknown systematic bias in the ship survey.

Next, the acoustic travel times and sound speed calculations were presented. An average of 72 CTD casts were performed at each array, in each epoch. The stability of sound speed, temperature and salinity was demonstrated over short (∼30 minutes) and long (>2 years) timescales, with RMS values of ±4.5 m/s, ± 0.2°C and ±0.5 psu at the surface and ±0.1 m/s, ±0.01°C and ±0.01 psu > 2 km depth. The acoustic raypath was maintained at each array with dynamic positioning to within ±15 m.

Moving surveys, or 1 nm radius circle drives, were shown for each PXP, in each epoch. This survey provided the a priori position of each transponder, which was used in the final solution for array position. The surveys were also used to estimate individual transponder displacements. The average displacement of each transponder at the shallow array was comparable to the plate convergence vector. This similarity suggests that uncertainty of the moving surveys may be less than originally estimated (±200 mm), depending on the stability of the sound speed structure across the 1 nm radius circle. At the deep array, only two transponder displacements were calculated from moving surveys. Though the average transponder displacement is comparable to plate convergence, individual transponder displacements portray unexpected results. Future work should attempt to resolve the uncertainty of this technique. The successful and unexpected estimation of

plate convergence at the shallow array shows that this could be a more economical option for some locations.

In the least-squares solution for array position, acoustic range residuals vary 20 to 50 cm peak to peak as a result of sound speed fluctuations in the upper water column. Calculations of array uncertainty showed that the GPSA vector uncertainty ranged from ±5-10 mm. Performing the least-squares adjustment with increasing width of data bins (cumulative solution) demonstrated that between 76 and 110 hours were needed to decrease the repeatability to <10 mm.

Another important aspect of the GPSA technique is a method for replacing an inactive transponder. A transponder relocation occurred at the deep array in 2003. Techniques for positioning a replacement transponder included the acoustic/optical survey and a least-squares adjustment to determine the latitude, longitude and height of each survey landing and transponder. The relocation contributed ±19 mm uncertainty to the array's vector of horizontal displacement. Optimal survey network geometry was determined in a simulation of the least-squares adjustment. Future relocations could decrease the contribution to array uncertainty to ±10 mm.

The GPSA experiments offshore Peru added additional data on the uncertainty of long-baseline kinematic GPS. Station residuals for a kinematic solution at 150 km ranged between ±20-40 mm. Transponder depth was also measured with GPSA moving surveys, timed-release pressure gauges and the acoustic/optical survey. A/O survey loop closures demonstrate repeatability on short timescales (∼ hours) between 1.5 and 6.7 cm. Repeatability of transponder depth measurements over long (>2 years) timescales demonstrates the rigidity of the array. Transponder baseline depth differences ranged from 3.2-8.0 cm between 2001 and 2003. Also, an algorithm to correct for tilt of the pressure gauges at some sites decreased the spread of successive depth measurements in 2001 by ∼2 cm.

VI.2 Geodetic observations

Two seafloor geodetic sites provided displacement measurements over separate structural units, as shown in seismic refraction and reflection surveys. The deep array, 20 km from the trench axis, is located on a topographic high, above several kilometers of sediment and toe of the continental backstop. This feature is named the the outer-arc high, suggested to be the topographic signature of the updip initiation of coupling. The shallow array, 50 km from the trench axis, overlies a thin veneer of sediments and the crystalline basement between the frontal prism and the Lima Basin. Measurements of array displacement were 53 mm/yr at 78° and 55 mm/yr at 89°, at the deep and shallow arrays, respectively.

At this latitude, the thrust fault has not ruptured since an M_w 8.0 in 1974. The seafloor geodetic observations are relevant to the interseismic period of the seismic cycle. The kinematic models in this study treated the continental plate as an elastic material and the interseismic period as a time when strain was accumulating uniformly in the continental plate. Although this is a simplification of the problem, this approach is taken in the majority of kinematic and mechanical models of plate interactions. With this understanding, GPSA array displacements most likely represent shallow, elastic strain accumulation. Deformation at the deep array indicates strong coupling between the oceanic plate and trenchward limit of the backstop at 4 km depth. Deformation at the shallow array indicates coupling between the oceanic plate and the basement rock at 10 km depth.

Although GPSA observations cannot differentiate between models that initiate coupling at 0 or 2 km depth, it is likely that the upper 2 km are not coupled. Several models have shown the weak, unconsolidated sediments of the accretionary prism cannot accumulate strain until the shear stress is greater than lithostatic. In the shallow portions of the thrust fault, underplated sediments have a high porosity and low permeability. These conditions lead to high pore fluid pressure and low effective normal stress. Coupling at 2 km depth is concurrent with the initiation of coupling beneath the outer-arc high. It also agrees with temperature and pressure

related material changes and fluid pressure changes with depth, which have been used to explain the stable-unstable transition.

Seismic records, thermal conditions and topography and gravity analyses can help interpret the evolution of the margin on a longer timescale. A correlation between flat slab segments and seismic energy release could be caused by a large, cold forearc. A correlation also exists between low topography andd gravity anomalies and seismic events. The Peruvian margin, with flat slab subduction and low topography and gravity anomalies, has frequent, large magnitude coseismic events. This suggests the presence of a wide, strongly coupled seismogenic zone. Our measurements of shallow coupling fit this broader view of the dynamics of the margin.

VI.3 Future GPS-acoustic campaigns

GPSA measurements and kinematic modeling should be performed at other convergent margins. Potential sites should correspond to previous data collection campaigns and societal impact. Potential GPSA sites were chosen based on existing thermal models and geodetic coverage, records of shallow and tsunamigenic earthquakes, tectonic erosion or accretion and societal impact from tsunami hazard as well as current geophysical quandaries. Five convergence zones in particular stand out as areas in which GPSA measurements would provide invaluable evidence to help resolve current debate. Burgmann et al. (2005) proposed shallow coupling below 50 km between 51° and 57°N along the Kamchatka subduction zone. To the north, they suggest the trench experiences significant aseismic slip. If this hypothesis is correct, GPSA arrays to the south of 57°N would be displaced at the full convergence rate; arrays to the north would experience minor displacement. At the Aleutian trench, significant interseismic strain buildup has been suggested above Stevenson Basin, offshore Kodiak island with seismic surveys (von Huene et al., 1999). A discrepancy between the updip limit of teleseismic events (8-10

km depth) and the updip limit of aftershcosk from the 1964 M_w 9.4 earthquake, suggests that stress may be accumulating beneath the outer shelf and upper slope. GPSA measurements would compliment current GPS studies of interseismic strain accumulation onshore. Around Sumatra, the 2004 Indonesian tsunami has sparked several deformation studies. GPSA arrays would ideally be located south of the 2004 epicenter as this is the area expected to rupture next. The intensely tsunamigenic nature of the margin demonstratse a need for understanding shallow strain accumulation and release on thrust faults known to be strongly coupled. The oceanic plate in northern Chile descends at a steep angle ($\sim$30°) relative to flat slab suduction at the Peruvian margin at 12°S. GPSA measurements at 20°S could contrast previous kinematic models, which indicate shallow coupling at the flat slab region possibly due a large, cold forearc. Finally, full locking on the Gibraltar Arc, a shallow east dipping fault west of the Mediterranean Sea, has been proposed by Thiebot and Gutscher (2006). The fault has been tied to the 1755, M_w 8.5-9.0 Lisbon earthquake. GPSA arrays could provide evidence of interseismic strain accumulation much like at the Peruvian margin. This easily accessible area would provide ample thermal, geodetic and seismic observations though no large seismic events have been observed for several centuries, similar to Cascadia and Nankai. This region is complicated by a low convergence rate, $\sim$10 mm/yr, requiring a longer than usual campaign.

References

Altimini, Z., Sillard, P., and Boucher, C., 2002: A new release of the International Terrestrial Reference Frame for earth science applications. *Journal of Geophysical Research*, **107**(2214-2232).

Barazangi, M., and Isacks, B. L., 1976: Spatial distribution of earthquakes and subduction of the Nazca Plate beneath South America. *Geology*, **4**, 686–692.

Beck, S. L., and Ruff, L. J., 1987: Rupture process of the great 1963 Kurile Islands earthquake sequence: Asperity interaction and multiple event rupture. *J. Geophys. Res.*, **92**, 14,123–14,138.

Bevis, M., and Martel, S. J., 2001: Oblique plate convergence and interseismic strain accumulation. *Geochemistry, Geophysics, Geosystems*, **2**.

Bilek, S. L., and Lay, T., 1999: Rigidity variations with depth along interplate megathrust faults in subductioin zones. *Nature*, **400**, 443–446.

Bilek, S. L., and Ruff, L. J., 2002: Analysis of the 23 June 2001 Mw = 8.4 Peru underthrusting earthquake and its aftershocks. *Geophys. Res. Lett.*, **29**(20), 1960.

Bolt, B. A., 1993: *Earthquakes*. W. H. Freeman, New York.

Brown, K. M., Kopf, A., and Weinberger, J. L., 2003: Compositional and fluid pressure controls on the state of stress on the Nankai subduction thrust; a weak plate boundary . *Earth and Planetary Science Letters*, **214**, 589–603.

Brown, K. M., Saffer, D. M., and Bekins, B. A., 2001: Smectite diagenesis, porewater freshening, and fluid flow at the toe of the Nankai wedge. *Earth and Planetary Science Letters*, **194**, 97–109.

Burgmann, R., Kogan, M. G., Steblow, G. M., Hilley, G., Levin, V. E., and Apel, E., 2005: Interseismic coupling and asperity distribution along the Kamchatka subduction zone. *J. Geophys. Res.*, **110**.

Byrne, D. E., Davis, D. M., and Sykes, L. R., 1988: Loci and maximum size of thrust earthquakes and the mechanics of the shallow region of subduction zones. *Tectonics*, **7**, 833–857.

Byrne, D. E., Wang, W.-H., and Davis, D. M., 1993: Mechanical role of backstops in the growth of forearcs. *Tectonics*, **12**(1), 123–144.

Cahill, T., and Isacks, B. L., 1992: Seismicity and shape of the subducted Nazca plate. *Journal of Geophysical Research*, **97**, 17,503–17,529.

Caspary, W., 1988: *Concepts of network and deformation analysis*. Monograph 11. Sydney, University of New South Wales. School of Surveying.

Chadwell, C. D., 2003: Shipboard towers for Global Positioning System antennas. *Ocean Engineering*, **30**(12), 1467–1487.

Chadwell, C. D., Spiess, F. N., Hildebrand, J. A., and Dragert, H., 2002: Seafloor geodetic evidence of episodic spreading 25 km east of the Juan de Fuca Ridge. *Eos, Transactions, American Geophysical Union*, **83**, 1385.

Chen, C. T., and Millero, F. J., 1977: Speed of sound at high pressures. *J. Acoust. Soc. Am.*, **62**, 1129–1135.

Clift, P. D., Pecher, I. A., Kukowski, N., and Hampel, A., 2003: Tectonic erosion of the Peruvian forearc, Lima Basin, by subduction and Nazca Ridge collision . *Tectonics*, **22**, 16.

Currie, C. A., Hyndman, R. D., Wang, K., and Kostoglodov, V., 2002: Thermal models of the Mexico subduction zone: Implications for the megathrust seismogenic zone. *Journal of Geophysical Research B, Solid Earth and Planets*, **107**, 2370.

Dahlen, F. A., 1990: Critical taper model of fold-and-thrust belts and accretionary wedges. *Ann. Rev. Earth Planet. Sci.*, **18**, 55–99.

Davis, D. M., 1996: *Accretionary mechanics with properties that vary in space and time*, chapter Subduction Top to Bottom, 39–48. Number 96 in Geophysical Monograph Series. AGU, Wash., D. C.

Davis, D. M., Suppe, J., and Dahlen, F. A., 1983: Mechanics of fold-and-thrust belts and accretionary wedges. *J. Geophys. Res.*, **88**, 1153–1172.

Davis, E. E., Becker, K., Wang, K., Obara, K., Ito, Y., and Kinoshita, M., 2006: A discrete episode of seismic and aseismic deformation of the Nankai trough subduction zone accretionary prism and incoming Philippine Sea plate. *Earth and Planetary Science Letters*, **242**, 73–84.

Degg, M. R., and Chester, D. K., 2005: Seismic and volcanic hazards in Peru: changing attitudes to disaster mitigation. *The Geographical Journal*, **171**(2), 125–145.

DeMets, C., Gordon, R. G., Argus, F., and Stein, S., 1994: Effect of recent revisions of the geomagnetic timescale on estimates of current plate motions. *Geophys. Res. Lett.*, **21**(2191-2194).

Dragert, H., and Hyndman, R. D., 1995: Continuous GPS monitoring of elastic strain in the northern Cascadia subduction zone. *Geophysical Research Letters*, **22**(7), 755–758.

Eanes, R., and Bettadpur, S., 1995: The CSR 3.0 global ocean tide model. Technical Memorandum CSR-TM-95-06, Center for Space Research.

Egbert, G. D., Bennett, A. F., and Foreman, M. G. G., 1994: TOPEX/POSEIDON tides estimated using a global inverse model. *Journal of Geophysical Research*, **99**, 24821–24852.

Ernst, W. G., 1990: Thermobarometric and fluid explusion history of subduction zones. *Journal of Geophysical Research*, **95**, 9047–9053.

Feigl, K. L., Agnew, D. C., Bock, Y., Dong, D., Donnellan, A., Hager, G. H., Herring, T. A., Jackson, D. D., Jordan, T. H., King, R. W., Larsen, S., Larson, K. M., Murray, M. H., Shen, Z., and Webb, F. H., 1993: Space geodetic measurement of crustal deformation in central and southern California, 1984-1992. *J. Geophys. Res.*, **98**, 21677–21712.

Flueck, P., Hyndman, R. D., and Wang, K., 1997: Three-dimensional dislocation model for great earthquakes of the Cascadia subduction zone. *J. Geophys. Res.*, **102**(B9), 20,539–20,550.

Fujita, M., Ishikawa, T., Mochizuki, M., Sato, M., Toyama, S., Katayama, M., Kawai, K., Matusumoto, Y., Yabuki, T., Asada, A., and Colombo, O. L., 2006: GPS/Acoustic seafloor geodetic observations: method of data analysis and application. *Earth Planets Space*, **58**(265-275).

Fukao, Y., 1979: Tsunami earthquakes and subduction processes near deep-sea trenches. *J. Geophys. Res.*, **84**(B5), 2303–2314.

Funakoshi, M., Fujimoto, H., Sweeney, A. D., Kuwano, A., Hino, R., Miura, S., and Osada, Y., 2005: GPS/Acoustic submarine positioning using a small buoy in the subduction zone off northeastern Japan. *Abstr. Joint Meet. Earth Planet. Sci.*, **J062-001**.

Gagnon, K., and Chadwell, C. D., 2007: Relocation of a seafloor transponder: Sustaining the gps-acoustic technique. *Earth Planets Space*, **59**, 327–336.

Gagnon, K., Chadwell, C. D., and Norabuena, E., 2005: Measuring the onset of locking in the Peru-Chile Trench with GPS and acoustic measurements. *Nature*, **434**, 205–208.

Gomberg, J., and Ellis, M., 1994: Topography and tectonics of the central New Madrid seismic zone: Results of numerical experiments using a three-dimensional boundary element program. *Journal of Geophysical Research*, **99**, 20299–20310.

Grosso, V. A. D., 1974: New equations for the speed of sound in natural waters (with comparisons to other equations). *J. Acoust. Soc. Am.*, **56**(4), 1084–1091.

Gutscher, M., 2002: Andean subduction styles and their effect on thermal structure and interaply coupling. *J. S. American Earth Sciences*, **15**, 3–10.

Hampel, A., 2002: The migration history of the Nazca Ridge along the Peruvian active margin; a re-evaluation . *Earth and Planetary Science Letters*, **203**, 665–679.

Hampel, A., Kukowski, N., Bialas, J., Huebscher, C., and Heinbockel, R., 2004: Ridge subduction at an erosive margin: The collision zone of the Nazca Ridge in southern Peru. *J. Geophys. Res.*, **109**(B02101).

Hartzell, S., and Langer, C., 1993: Importance of model parametrization in finite fault inversions: Application to the 1974 Mw 8.0 Peru earthquake. *J. Geophys. Res.*, **98**(B12), 22,123–22,134.

Hildebrand, J. A., Chadwell, C. D., Wiggins, S. M., and Speiss, F. N., 2000: Offshore geodetic monitoring on the southeast flank of Kilauea Volcano . *Seismological Research Letters*, **71**, 232.

Hutton, W., DeMets, C., Sanchez, O., Suarez, G., and Stock, J., 2001: Slip kinematics and dynamics during and after the 1995 October 9 Mw = 8.0 Colima-Jalisco earthquake, Mexico, from GPS constraints. *Geophysical Journal International*, **146**, 637–658.

Hyndman, R. D., and Wang, K., 1995: The rupture zone of Cascadia great earthquakes from current deformation and the thermal regime. *Journal of Geophysical Research*, **100**(B11), 22,133–22,154.

Hyndman, R. D., Wang, K., and Yamano, M., 1995: Thermal constraints on the seismogenic portion of the southwestern Japan subduction thrust. *Journal of Geophysical Research*, **100**(B8), 15,373–15,392.

Hyndman, R. D., Yamano, M., and Oleskevich, D. A., 1997: The seismogenic zone of subduction thrust faults. *Island Arc*, **6**, 244–260.

Jr., G. H. P., Young, L. E., Speiss, F. N., Boegeman, D. E., Lawhead, R. M., Dragert, H., Schmidt, M., Jewsbury, G., Lisowski, M., and DeMets, D. C., 1993: Status of GPS/Acoustic measurements of seafloor strain accumulation across the Cascadia Subduction Zone. *EOS, Transactions, AGU*, **74**(43), 200.

Kanamori, H., 1972: Mechanism of tsunami earthquakes. *Phys. Earth Planet. Inter.*, **6**, 346–359.

Kastner, M., Elderfield, H., and Martin, J. B., 1991: Fluids in convergent margins: What do we know about their composition, origin, role in diagenesis and importance for oceanic chemical fluxes. *Philos. Trans. R. Soc. London, Ser. A*, **335**, 275–288.

Kido, M., Fujimoto, H., Miura, S., Osada, Y., Tsuka, K., and Tabei, T., 2006: Seafloor displacement at Kumano-nada caused by the 2004 off Kii Peninsula earthquakes, detected through repeated GPS/Acoustic surveys. *Earth Planets Space*, **58**, 1–5.

Krabbenhoeft, A., Bialas, J., Kopp, H., Kukowski, N., and Huebscher, C., 2004: Crustal structure of the Peruvian continental margin from wide-angle seismic studies . *Geophysical Journal International*, **159**, 749–764.

Kukowski, N., Hampel, A., Bialas, J., Huebscher, C., Barckhausen, U., and Bourgois, J., 2001: Tectonic erosion at the Peruvian margin: Evidence from swath bathymetry data and process identification from 3d sandbox analogue modeling. *Eos Trans. AGU Fall Meet. Suppl.*, **82**(47), T31A–0817.

Kukowski, N., von Huene, R., Malavieille, J., and Lallemand, S. E., 1994: Sediment accretion against a buttress beneath the Peruvian continentnal margin at 12S as simulated with sandbox modeling. *Geol. Rundsch*, **83**(822-831).

Kulm, L. D., Prince, R. A., French, W., Johnson, S., and Masias, A., 1981: Crustal structure and tectonics of the central Peru continental margin and trench. *Geol. Soc. Am. Mem.*, **154**, 445–468.

Lallemand, S. E., Schurle, P., and Lalavieille, J., 1994: Couloumb theory applied to accretionary and nonaccretionary wedges: possible causes for tectonic erosion and/or frontal accretion. *J. Geophys. Res.*, **99**(6), 12033–12055.

Larson, K. M., Freymuller, J. T., and Philipsen, S., 1997: Global plate velocities from the Global Positioning System. *Journal of Geophysical Research*, **102**, 9961–9981.

Lay, T., and Kanamori, H., 1981: *An asperity model of great earhtquake sequences*, volume 4 of *Maurice Ewing Ser.*, chapter Earthquake Prediction: An International Review, 579–592. AGU, Wash., D. C.

Lay, T., Kanamori, H., and Ruff, L. J., 1982: The asperity model and the nature of large subduction zone earthquakes. *Earthquake Pred. Res.*, **1**, 3–71.

Leffler, L., Stein, S., Mao, A., Dixon, T., Ellis, M., Ocola, L., and Sacks, I. S., 1997: Constraints on present-day shortening rate across the central eastern Andes from GPS data. *Geophysical Research Letters*, **24**, 1031–1034.

Leick, A., 2004: *GPS Satellite Surveying*. John Wiley and Sons, 3rd edition.

Marone, C., and Scholz, C. H., 1988: The depth of seismic faulting and the upper transition from stable to unstable slip regimes. *Geophysical Research Letters*, **15**(6), 621–624.

Melbourne, T., Carmichael, E., DeMets, C., Hudnut, K., Sanchez, O., Stock, J., Suarez, G., and Webb, F., 1997: The geodetic signature of the M8.0 oct. 9, 1995, Jalisco subduction earthquake. *Geophysical Research Letters*, **24**(6), 715–718.

Miura, S., Sweeney, A., Fujimoto, H., Osaki, H., Kawai, E., Ichikawa, R., Konko, T., Osada, Y., and Chadwell, C. D., 2002: Evaluations of accuracy in kinematic GPS analyses using a precision roving antenna platform. *Eos, Transactions, American Geophysical Union*, **83**(47), Fall Meet. Suppl. Abstract G52A–0959.

Moore, J. C., Lockner, D. A., Shengli, M., Summers, R., and Byerlee, J. D., 1997: Strengths of serpentinite at elevated temperatures. *J. Geophys. Res.*, **102**, 14,787–14,801.

Moore, J. C., and Saffer, D., 2001: Updip limit of the seismogenic zone beneath the accretionary prism of southwest Japan: An effect of diagenetic to low-grade metamorphic processes and increasing effective stress. *Geological Society of America*, **29**, 183–186.

Moore, J. C., and Vrolijk, P., 1992: Fluids in accretionary prisms. *Review of Geophysics*, **30**(2), 113–135.

Newman, A. V., Schwartz, S. Y., Gonzalez, V., DeShon, H. R., Protti, J. M., and Dorman, L. M., 2002: Along-strike variability in the seismogenic zone below Nicoya Peninsula, Costa Rica. *Geophysical Research Letters*, **29**, 4.

Norabuena, E., Dixon, T., Stein, S., and Harrison, C. G. A., 1999: Decelerating Naza-South America and Nazca-Pacfic plate motions. *Geophysical Research Letters*, **26**, 3405–3408.

Norabuena, E., Leffler-Griffin, L., Mao, A., Dixon, T., Stein, S., Sacks, I. S., Ocola, L., and Ellis, M., 1998: Space geodetic observations of Nazca-South America convergence across the Central Andes. *Science*, **279**, 358–362.

Obana, K., Katao, H., and Ando, M., 2000: Seafloor positioning system with GPS-acoustic link for crustal dynamics observation - a preliminary result from experiments in the sea. *Earth Planets Space*, **52**, 415–423.

Oleskevich, D. A., Hyndman, R. D., and Wang, K., 1999: The updip and downdip limits to great subduction earthquakes: Thermal and structural models of Cascadia, south Alaska, SW Japan and Chile. *Journal of Geophysical Research, B, Solid Earth and Planets*, **104**, 14,965–14,991.

Osada, Y., Fujimoto, H., Miura, S., Sweeney, A., Kanazawa, T., Nakao, S., Sakai, S., Hildebrand, J. A., and Chadwell, C. D., 2003: Estimation and correction for the effect of sound velocity variation on GPS/Acoustic seafloor positioning; an experiment off Hawaii Island . *Earth, Planets and Space*, **55**, e17–e20.

Pacheco, J. F., Sykes, L. R., and Scholz, C. H., 1993: Nature of seismic coupling along simple plate boundaries of the subduction type. *Journal of Geophysical Research*, **98**(B8), 14,133–14,159.

Pardo, M., Comte, D., and Monfret, T., 2002: Seismotectonic and stress distribution in the central Chile subduction zone. *J. S. American Earth Sciences*, **15**, 11–22.

Peacock, S. M., and Wang, K., 1999: Seismic consequences of warm versus cool subduction metamorphism: Examples from southwest and northeast Japan. *Science*, **286**, 937–939.

Phillips, K., and Chadwell, C. D., 2005: Refined deformation models of the south flank of Kilauea Volcano, Hawaii based on seafloor geodetic data from 2000 to 2004. *EOS, Transactions, American Geophysical Union*, **86**(Fall Meet. Suppl. Abstract G53B-0882).

Ponko, S. C., and Peacock, S. M., 1995: Thermal modeling of the southern Alaska subduction zone: Insight into the petrology of the subducting slab and overlying mantle wedge. *Journal of Geophysical Research*, **100**(B11), 22,117–22,128.

Provost, C. L., Genco, M. L., Lyard, F., Vincent, P., and Canceil, P., 1994: Spectroscopy of the world ocean tides froma finite element hydrodynamic model. *Journal of Geophysical Research*, **99**, 24777–24797.

Ruff, L. J., and Tichelaar, B. W., 1996: *What controls the seismogenic plate interface in subduction zones*, chapter Subduction Top to Bottom, 105–111. American Geophysical Union, Wash., D. C.

Saffer, D. M., and Marone, C., 2003: Comparison of smetitie- and illite-rich gouge frictional properties: application to the updip limit of the seismogenic zone along subduction megathrusts. *Earth and Planetary Science Letters*, **215**, 219–235.

Sallares, V., and Ranero, C. R., 2005: Structure and tectonics of the erosional convergent margin off Antofagasta, north Chile (23 30S). *Journal of Geophysical Research, B, Solid Earth and Planets*, **110**, 19.

Satake, K., and Tanioka, Y., 1999: Sources of tsunami and tsunamigenic earthqukes in subduction zones. *Pure and Applied Geophysics*, **154**.

Saunders, P. M., and Fofonoff, N. P., 1976: Conversion of pressure to depth in the ocean. *Deep-Sea Research*, **23**, 109–111.

Savage, J. C., 1983: A dislocation model of strain accumulation and release at a subduction zone. *J. Geophys. Res.*, **88**(B6), 4984–4996.

Scholz, C. H., 1998: Earthquakes and friction laws. *Nature*, **391**.

Scholz, C. H., 2003: *The Mechanics of Earthquakes and Faulting*. Cambridge Univ. Press, 2 edition.

Schweller, W. J., Kulm, L. D., and Prince, R. A., 1981: *Memoir - Geological Society of America: Tectonics, structure, and sedimentary framework of the Peru-Chile Trench*. Geological Society of America (GSA), Boulder, CO, United States (USA).

Schwiderski, E. W., 1980: Ocean tides. *Marine Geodesy*, **3**, 161–255.

Sebrier, M., and Soler, P., 1991: *Andean Magmetism and its tectonic settings*, chapter Tectonic and magmatism in the Peruvian Andes from late Oligocene time to the Present, 265. Geological Society of America (GSA).

Sella, G., Dixon, T., and Mao, A., 2002: REVEL: A model for recent plate velocities from space geodesy. *Journal of Geophysical Research*, **107**(B4), 10.

Seno, T., 2002: Tsunami earthquakes as transient phenomena. *Geophysical Research Letters*, **29**(10).

Smith, W. H. F., and Sandwell, D. T., 1997: Global seafloor topography from satellite altimetry and ship depth soundings. *Science*, **277**, 1957–1962.

Song, T. A., and Simons, M., 2003: Large trench-parallel gravity variations predict seismogenic behavior in subduction zones. *Science*, **301**, 630–633.

Spence, W., Mendoza, C., Engdahl, E. R., Choy, G. L., and Norabuena, E., 1999: Seismic subduction of the Nazca Ridge as shown by the 1996-1997 Peru earthquakes. *Pure Appl. Geophys.*, **154**, 753–776.

Spiess, F. N., Chadwell, C. D., Hildebrand, J. H., Dragert, H., Jabson, D., Sweeney, A., and Zimmerman, R., 2000: New geodetic reference stations on the Juan de Fuca Plate. *Eos, Transactions, American Geophysical Union*, **81**, 333.

Spiess, F. N., Chadwell, C. D., Hildebrand, J. H., Young, L. E., Jr., G. H. P., and Dragert, H., 1998: Precise GPS/Acoustic positioning of seafloor reference points for tectonic studies . *Physics of the Earth and Planetary Interiors*, **108**, 101–112.

Sweeney, A. D., Chadwell, C. D., hildebrand, J. A., and Speiss, F. N., 2005: Centimeter-Level positioning of seafloor acoustic transponder from a deeply-towed interrogator. *Marine Geology*, **28**, 39–70.

Swenson, J. L., and Beck, S. L., 1999: Source characteristics of the 12 November 1996 Mw 7.7 peru subduction zone earthquake. *Pure Appl. Geophys.*, **154**, 731–751.

Tabei, T., Ozawa, T., Date, Y., Hirahara, K., and Nakano, T., 1996: Crustal deformation at the Nankai subduction zone, southwest Japan, derived from GPS measurements. *Geophysical Research Letters*, **23**(21), 3059–3062.

Thiebot, E., and Gutscher, M. A., 2006: The Gibraltar Arc seismogenic zone (part 1): Constraints on a shallow east dipping fault plane source for the 1755 Lisbon earthquake provided by seismic data, gravity and thermal modeling. *Tectonophysics*, **426**, 135–152.

Tichelaar, B. W., and Ruff, L. J., 1993: Depth of seismic coupling along subduction zones . *Journal of Geophysical Research, B, Solid Earth and Planets*, **98**, 2017–2037.

Tse, S. T., and Rice, J. R., 1986: Crustal earthquake instability in relation to the depth variation of frictional slip properties. *Journal of Geophysical Research*, **91**, 9452–9472.

von Huene, R., and Lallemand, S., 1990: Tectonic erosion along the Japan and Peru convergent margins. *Geological Society of America Bulletin*, **102**, 704–720.

von Huene, R., Pecher, I. A., and Gutscher, M. A., 1996: Development of the accretionary prism along Peru and material flux after subduction of Nazca Ridge. *Tectonics*, **15**, 19–33.

von Huene, R., and Ranero, C. R., 2003: Subduction erosion and basal friction along the sediment-starved convergent margin off Antofagasta, Chile . *Journal of Geophysical Research, B, Solid Earth and Planets*, **108**, 16.

von Huene, R., and Scholl, D. W., 1991: Observations at converget margins concerning sediment subudction, subduction erosion, and the growth of continental crust. *Review of Geophysics*, **29**, 279–316.

von Huene, R., Weinrebe, W., and Heeren, F., 1999: Subduction erosion along the north Chile margin . *Journal of Geodynamics*, **27**, 345–358.

Vrolijk, R., 1990: On the mechanical role of smectite in subduction zones. *Geology*, **18**, 703–707.

Wang, C., 1980: Sediment subduction and frictional sliding in a subduction zone. *Geology*, **8**, 530–533.

Wang, K., and Hu, Y., 2006: Accretionary prisms in subduction cycles: The theory of dynamic couloumb wedge. *J. Geophys. Res.*, **111**(B06410).

Wang, W.-H., and Davis, D. M., 1996: Sandbox model simulation of forearc evolution and noncritical wedges. *J. Geophys. Res.*, **108**(B3), 11329–11339.

Warsi, W. E. K., Hilde, T. W. C., and Searle, R. C., 1983: Convergence structures of the Peru Trench between 10 degrees S and 14 degrees S . *Tectonophysics*, **99**, 313–329.

Watts, I., 2000: Sea-bird electronics. 19.2, Sea-Bird Electronics, Bellevue, WA.

Wdowinski, S., and Bock, Y., 1994: The evolution of deformation and topography of high elevated plateaus; Application to the Central Andes. *J. Geophys. Res.*, **99**(B4), 7121–7130.

Webb, F. H., and Zumberge, J. F., 1997: An introduction to GIPSY/OASIS-II. Technical Report D-11088, Jet Propulsion Lab.

Wells, R. E., Blakely, R. J., Sugiyama, Y., Scholl, D. W., and Dinterman, P. A., 2003: Basin-centered asperities in great subduction zone earthquakes: A link between slip, subsidence, and subduction erosion? *J. Geophys. Res.*, **108**(B10), 2507.

Wilson, W. D., 1960: Equation for speed of sound in seawater. *J. Acoust. Soc. Am.*, **32**(10), 1357.

Wortel, M. J. R., and Cloetingh, S. A. P. L., 1985: Accretion and lateral variations in tectonic structure along the Peru-Chile trench. *Tectonophysics*, **112**, 443–462.

Yamada, T., Ando, M., Tadokoro, K., Sato, K., Okuda, T., and Oike, K., 2002: Error evaluation in acoustic positioning of a single transponder for seafloor curstal deformatin measurements. *Earth Planets Space*, **54**, 871–881.